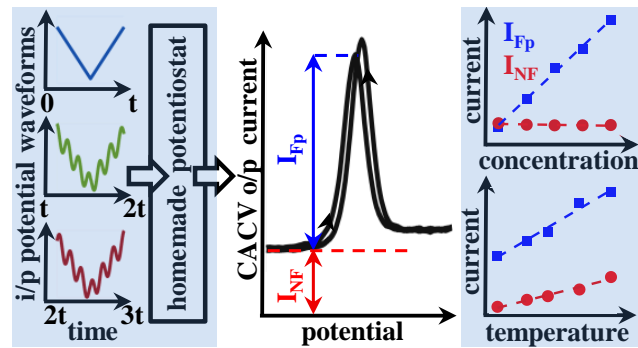


# Complementary AC Voltammetry - A method for simultaneous measurement of faradaic and nonfaradaic currents in an electrochemically reversible system

N. Kumar, A. Arora, and A. Krishnan\*

**Abstract**— We report a technique named complementary alternating current voltammetry (CACV) to simultaneously measure faradaic and nonfaradaic currents in an electrochemical sensing apparatus using three sequential input potential waveforms: i) a triangular waveform as used in cyclic voltammetry (CV); ii) small signal sine modulated triangular waveform; and iii) small signal cosine modulated triangular waveform. The three output currents were post-processed to obtain the peak faradaic current ' $I_{FP}$ ' (sensitive to the concentration of the analyte) and nonfaradaic current ' $I_{NF}$ ' (sensitive to the equivalent circuit parameters of the electrochemical cell). The proposed method has the advantage of producing a straight baseline  $I_{NF}$  which is not easily possible in CV and measure  $I_{FP}$  without using a phase lock-in amplifier (commonly used in AC voltammetry). The proposed method was computationally investigated using finite difference time domain method and experimentally validated for a standard redox reaction of potassium ferricyanide using a homemade digital potentiostat. CACV showed the successful recovery of faradaic and nonfaradaic currents, even for the cases where CV analysis was not possible due to the low faradaic-to-nonfaradaic current ratio. Finally, we observed that there was change in the peak current with a change in concentration as well as temperature, whereas change in the baseline was only due to the change in temperature. We believe that this can be used for calibration of an electrochemical cell to sense analytes or to compensate for any change in currents in a fixed analyte concentration due to extraneous parameter changes.

**Index Terms**— AC voltammetry, cyclic voltammetry, electrochemical sensor, faradaic current, FDTD simulation, nonfaradaic current, sensor calibration



## I. INTRODUCTION

Over decades, electrochemical methods have shown potential for chemical analysis and sensing applications, wherein the output is measured either as a reaction current or a potential difference [1]–[7]. However in any practical electrochemical system, the measured quantities consist of different inseparable interfering components. The output current consists of two components i) the reaction current called the faradaic current; and ii) the double layer (DL) charging current called the nonfaradaic current, while the potential is the sum of the reaction potential and the resistive drop [8]. In most of the cases, the nonfaradaic current and the resistive drop are considered as undesired components and hence need to be suppressed [9], [10]. This is one of the major challenges

in the design and development of a sensitive and reliable electrochemical sensor, especially for an affordable, point-of-care biosensors due to two reasons. First, the faradaic current reduces linearly with the reduction in analyte concentration, whereas the nonfaradaic current remains almost constant [11], [12]. At low analyte concentrations, the output current is mostly nonfaradaic, making it difficult to recover the small faradaic component [13]. Second, these sensors have to work outside the controlled lab environment, using a hand-held potentiostat and on-chip miniaturized electrodes. This makes them prone to error due to factors like environmental changes, chip-to-chip variation and cycle-to-cycle electrode degradation [14].

In practice, the resistive drop can be minimized using standard methods such as usage of micro-electrodes, supporting electrolyte, Luggin probe and negative resistance [15], [16]. The faradaic current recovery is relatively tedious and critical for analysis, measurement of which involves existing standard methods such as background current subtraction [17], various pulse voltammetry and AC voltammetry [18]. However

Manuscript received June 20, 2020. (\*Corresponding author: A. Krishnan.)

The authors are with the Department of Electrical Engineering, Indian Institute of Technology Madras, Chennai 600036, India (e-mail: ee15s076@ee.iitm.ac.in; ee16d025@ee.iitm.ac.in; ananthk@ee.iitm.ac.in)

these methods still suffer some drawbacks such as fluctuation in background current [19], limited temporal resolution and phase measurement errors [18]. Various signal post-processing methods for faradaic current recovery such as chemometric analysis [11], convolution-based analysis [19], independent component analysis [20], iterative target transformation factor analysis [21] and different Fourier domain analysis [22]–[24] have been proposed earlier. Many recent reports propose new voltammetry methods to solve specific problems such as reduction of inter-species interference [25], sensitive determination of electrochemical transfer coefficient, reaction rate constant [26] and reduction of electrode fouling during multi-cycle electrochemical analysis [27]. However, many of these methods neglect the nonfaradaic current, which could potentially provide information about any undesired change in the system parameters. Therefore, simultaneous recovery of faradaic and nonfaradaic current is critical for reliable sensing [28].

In this work, a voltammetry method namely ‘complementary ac voltammetry’ (CACV) is proposed to simultaneously retrieve faradaic and nonfaradaic currents using three input potential waveforms in sequence: i) a triangular waveform as used in cyclic voltammetry (CV); ii) small signal sine modulated triangular waveform; and iii) small signal cosine modulated triangular waveform. We describe this new method in detail with the help of theory, numerical simulation and demonstrate its experimental validation. We have also compared this method with CV and demonstrate the recovery of faradaic and nonfaradaic currents under different conditions. The baseline determination is critical for the quantification of the peak current in conventional CV, which in the proposed method is direct and straightforward, thus resulting in lower detection limit. In case of electrode fouling, the CACV method showed superior performance compared to CV. Through systematic experiments, we showed that the CACV peak current has linear dependence on the analyte concentration. Finally, CACV was used to identify the effect of temperature variation on the estimation of analyte concentration.

## II. MATERIAL AND METHODS

### A. Apparatus

All experiments were performed using polypropylene tubes as an electrochemical cell. 70 mm long bare HB pencil leads with 0.5 mm dia (with measured end to end resistance  $5.3 \pm 0.3\Omega$ ) as pencil graphite electrodes (PGE) for working and counter electrodes, as shown in Fig. 1(a). For reference electrode, either PGE or Ag/AgCl electrode was used as indicated in different experiments. All the measurements were performed using a homemade potentiostat (circuit schematic shown in the Fig. 1(b)) designed using off-the-self components on a general purpose printed circuit board along the lines of low cost potentiostat [29], [30]. Tektronix AFG1022 function generator was used to generate the required potential waveforms **E** and NI USB 6008 OEM data acquisition (DAQ) board was used to acquire the corresponding output current waveforms **I**. For all the measurements, the geometrical area of PGE for all three electrodes was maintained constant. Before

the experiments, the PGEs were tested for their electrochemical stability using cyclic voltammetry and chronoamperometry measurements. The PGEs electrode potential and RC decay rate for several measurement cycles were found to be stable in our experiments. Matlab was used for processing and plotting the acquired data and also for the finite difference time domain (FDTD) simulations.

### B. Reagents and Solution

Potassium chloride (KCl) and potassium ferricyanide ( $K_3Fe(CN)_6$ ) procured from Sigma-Aldrich were used as received. Supporting electrolyte solution of 0.1 M KCl was prepared in 18 MΩ/cm de-ionised water. A 64 mM stock solution of  $K_3Fe(CN)_6$  in 0.1 M KCl was used to prepare different lower concentrations up to 0.125 mM of  $K_3Fe(CN)_6$  by successive dilution. The choice of  $K_3Fe(CN)_6$  over other electron transfer species such as ferrocenemethanol or ruthenium hexamine chloride, was due to two factors. First,  $K_3Fe(CN)_6$  is a commonly used electron transfer mediator in evaluating an electrochemical system. Second, it exhibits adsorption effects on PGEs, which can be used to test the performance of the proposed method under such conditions. In this work, we show that our proposed method can respond to changes in resistance and capacitance of the PGEs due to adsorption effects.

## III. THEORY

### A. Theoretical model

Fig. 1(c) shows the schematic of one dimensional, 3-electrode electrochemical cell with its Randles equivalent circuit used for theoretical and computational analysis. For simplicity, a diffusion limited, one electron reversible electrochemical reaction (1e-RER),  $A + e^{-1} \rightleftharpoons B$ , has been considered. The initial concentration of A has been assumed to be  $c_A^*$ , while that of species B to be  $c_B^* = 0$ . The drift transport of both the species has been assumed to be negligible and the time scale ( $t_{max}$ ) of the experiment has been assumed to be small enough to neglect any transport due to convection. Therefore, diffusion is the only mode of transport of the species in the cell. The diffusion coefficients for both the species have been assumed to be equal, and represented as ‘D’. Therefore, the concentration of A and B at any position ‘x’ from the working electrode and at any time instant ‘t’ follows the equivalence relation given by (1).

$$\begin{aligned} c_A(x, t) + c_B(x, t) &= c_A^* + c_B^* \\ &= c_A^* \\ \Rightarrow c_B(x, t) &= c_A^* - c_A(x, t) \end{aligned} \quad (1)$$

For diffusion dominated transport of any species ‘j’, the concentration  $c_j$  in one dimension ‘x’ follows Fick’s second law:

$$\frac{\partial c_j}{\partial t} = D \left( \frac{\partial^2 c_j}{\partial x^2} \right) \quad (2)$$

The reaction kinetics has been assumed to be much faster than the diffusion rate, such that the reaction is limited by diffusion of species rather than the reaction kinetics and hence

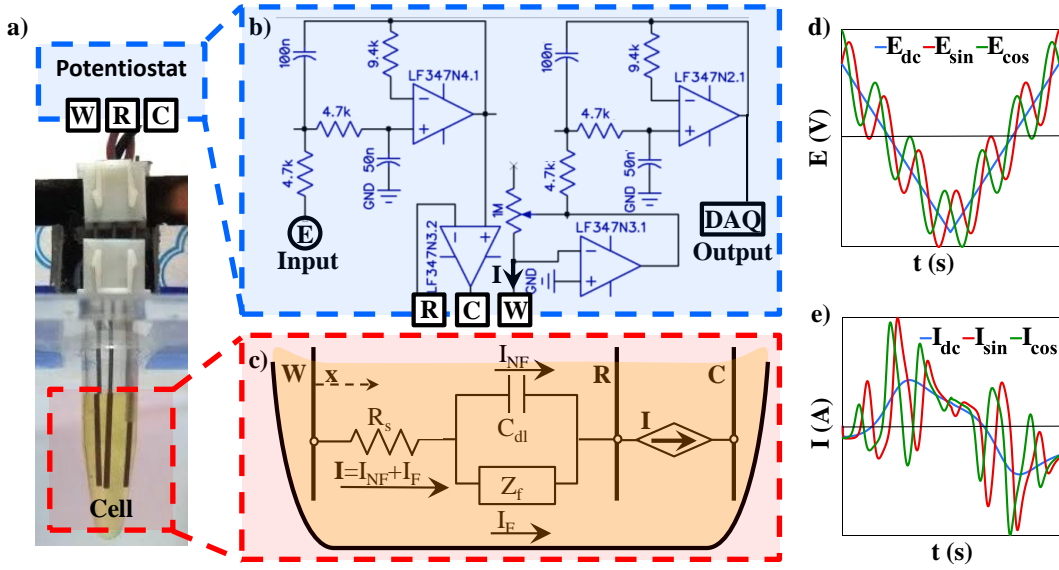


**Fig. 1. Experimental setup:** a) 3-electrode electrochemical cell with W, R and C as the connection ports of the potentiostat for respectively the working, reference and the counter electrodes; b) Potentiostat circuit schematic where  $E$  is the input potential applied using a function generator and  $I$  is the output current recorded using DAQ; c) One dimensional model of the electrochemical cell with Randles equivalent circuit showing series resistance  $R_s$ , DL capacitance  $C_{dl}$  and faradaic impedance  $Z_f$  between W and R. The output current  $I$  is the sum of nonfaradaic  $I_{NF}$  and faradaic  $I_F$  currents flowing between W and C with zero current in R indicated by a dependent current source  $I$ .  $x$  is the distance from the working electrode used in the simulations; d) Input potential waveforms used in CACV; and e) The corresponding output current waveforms. In both d) and e), frequency and amplitude of modulation have been exaggerated for the sake of clarity.

the system is in Nernst equilibrium. The concentration of the species at the surface of working electrode for applied potential  $E$  follows the Nernst equation given as (3), where  $E_f^0$  is the formal reduction potential,  $R$  is the gas constant,  $T$  is the ambient temperature and  $F$  is the Faraday constant.

$$E = E_f^0 + \frac{RT}{F} \ln \left( \frac{c_A(x=0,t)}{c_B(x=0,t)} \right) \quad (3)$$

Substituting  $c_B(x,t)$  from (1) in (3),  $c_A(x,t)$  at the surface of working electrode can be calculated as:

$$c_A(x=0,t > 0) = \frac{c_A^*}{1 + \exp \left( -\frac{E - E_f^0}{RT/F} \right)} \quad (4)$$

Finally the faradaic current  $I_F$  for the working electrode of surface area ‘S’ can be calculated using Fick’s first law:

$$I_F = -D \frac{\partial c_A}{\partial x} \Big|_{x=0} \times S \quad (5)$$

### B. Proposed method - CACV to measure faradaic and nonfaradaic currents

In the proposed CACV method, three different potential waveforms, viz.,  $E_{dc}$ ,  $E_{sin}$  and  $E_{cos}$ , as shown in Fig. 1 (d), are to be applied sequentially at the working electrode. The resulting current waveforms viz.,  $I_{dc}$ ,  $I_{sin}$  and  $I_{cos}$  corresponding to the respective applied input potentials are shown in Fig. 1 (e). It can be seen that,  $E_{dc}$  is a typical triangular CV input waveform while  $E_{sin}$  and  $E_{cos}$  are the small signal modulated triangular waveforms, typically used in ac voltammetry, with the modulation  $\Delta E \sin(2\pi ft + \theta)$ , where  $\theta = 0$  or  $\theta = \pi/2$  corresponding to sine or cosine waveform

respectively. For  $\theta = 0$ , the modulation  $e_{sin} = \Delta E \sin(2\pi ft)$  results in the ac output current  $i_{sin}$  which is the sum of faradaic and nonfaradaic currents expressed as:

$$i_{sin} = \underbrace{\frac{\Delta E}{Z_f} \sin(2\pi ft + \phi_f)}_{\text{faradaic}} + \underbrace{\frac{\Delta E}{Z_{nf}} \sin(2\pi ft + \phi_{nf})}_{\text{nonfaradaic}} \quad (6)$$

where,  $\phi_f = \pi/4$  for an ideal 1e-RER and  $0 < \phi_f < \pi/4$  for a quasireversible system [31] and the magnitude of equivalent faradaic admittance ( $1/Z_f$ ) being a function of the applied potential  $E_{dc}$ . The nonfaradaic current can be calculated from the Randles equivalent circuit shown in Fig. 1(c).  $1/Z_{nf}$  and  $\phi_{nf}$  are the magnitude and phase of the nonfaradaic admittance respectively, both of which are functions of  $R_s$  and  $C_{dl}$ . Similarly, for  $\theta = \pi/2$ , the modulation  $e_{cos} = \Delta E \cos(2\pi ft)$  results in ac output current  $i_{cos}$  given as:

$$i_{cos} = \frac{\Delta E}{Z_f} \cos(2\pi ft + \phi_f) + \frac{\Delta E}{Z_{nf}} \cos(2\pi ft + \phi_{nf}) \quad (7)$$

The phasor sum of these two ac output currents will be :

$$\begin{aligned} i_{ac} &= \sqrt{i_{sin}^2 + i_{cos}^2} \\ &= \Delta E \sqrt{\frac{1}{Z_f^2} + \frac{1}{Z_{nf}^2} + \frac{2\cos(\phi_f - \phi_{nf})}{Z_f Z_{nf}}} \\ &= \underbrace{\left( \frac{\Delta E}{Z_f} \angle \phi \right)}_{i_f} + \underbrace{\left( \frac{\Delta E}{Z_{nf}} \angle 0 \right)}_{i_{nf}} \end{aligned} \quad (8)$$

where,  $\phi = \phi_f - \phi_{nf}$

In equation (9), the faradaic current  $i_f$  depends on  $Z_f$  and hence is a function of  $E_{dc}$ , while the nonfaradaic current  $i_{nf}$  depends on  $Z_{nf}$  and hence is a function of  $R_s$  and  $C_{dl}$  only. Thus, over the complete potential scan range of  $E_{dc}$ , the current  $i_{nf}$  remains constant resulting in a flat baseline, with the variation in  $i_f$  added to it. Therefore the proposed method, contrary to ac voltammetry, can be used to estimate both the current components  $i_f$  and  $i_{nf}$ , without any assumption on the value of phase  $\phi$ .

In CACV experiments,  $i_{sin}$  is the difference between  $I_{sin}$  and  $I_{dc}$ , while  $i_{cos}$  is the difference between  $I_{cos}$  and  $I_{dc}$ . Following (8), the final CACV output current can be calculated as:

$$I_{CACV} = \sqrt{(I_{sin} - I_{dc})^2 + (I_{cos} - I_{dc})^2} \quad (10)$$

$I_{CACV}$  was digitally filtered and plotted against  $E_{dc}$  to obtain the CACV voltammogram.

### C. Simulation setup for a 1D electrochemical cell - Effect of series resistance and DL capacitance

FDTD was used to simulate 1e-RER for one dimensional electrochemical cell [32]. For the CACV input potential waveforms  $E$ ,  $I_F$  and  $I_{NF}$  were calculated iteratively at every time instant from  $t = 0$  to  $t = t_{max}$ . In the first iteration, the charge  $Q_c$  on  $C_{dl}$  was assumed to be zero, thus the potential  $E_c$  across it was  $Q_c/C_{dl} = 0$ , resulting in total electrochemical current  $I = (E - E_c)/R_s = E/R_s$ . Next,  $c_A(x, t)$  was calculated by solving (2) as:

$$\begin{aligned} \frac{c(x, t) - c(x, t - \Delta t)}{\Delta t} &= \\ \frac{c(x - \Delta x, t) - 2c(x, t) + c(x + \Delta x, t)}{(\Delta x)^2}, \end{aligned} \quad (11)$$

under the boundary conditions at  $x = 0$  given by (4) for  $E = E_c = 0$  and at  $x_{max} = 6\sqrt{Dt_{max}}$  [33] given as  $c^*_A$ . For working electrode of a given surface area ‘S’,  $I_F$  was calculated using (5) as:

$$I_F = -D \left( \frac{-c(2\Delta x, t) + 4c(\Delta x, t) - 3c(0, t)}{2\Delta x} \right) \times S. \quad (12)$$

$I_{NF}$  was calculated as  $I - I_F$ , which flows through  $C_{dl}$  thus charging it to  $Q_c + I_{NF} \times \Delta t$ , updating  $Q_c$  for the next iteration. The computed current  $I$  for different input potentials  $E$  were used to calculate  $I_{CACV}$  using the relation given by (10). The  $I_{CACV}$  obtained was filtered using an ideal low-pass filter and plotted against  $E_{dc}$  to obtain the CACV voltammogram.

## IV. RESULTS AND DISCUSSION

### A. Proposed CACV method vs standard CV method

TABLE I  
SIMULATION PARAMETERS

Parameters	Symbol	Magnitude		Unit
		ideal	non-ideal	
Temperature	T	298	298	K
Electrode Area	S	0.09	0.09	cm <sup>2</sup>
Concentration	$c_A^*$	10	10	mM
Diffusion coefficient	D	6.5	6.5	10 <sup>-6</sup> cm <sup>2</sup> /s
Scan rate	$\nu$	200	200	mV/s
Modulation amplitude	$\Delta E$	10	10	mV
Modulation frequency	f	10	10	Hz
DL Capacitance	$C_{dl}$	0	1	$\mu$ F/cm <sup>2</sup>
Series resistance	$R_s$	0	25	M $\Omega$
Parallel DL resistance	$R_p$	$\infty$	3	M $\Omega$

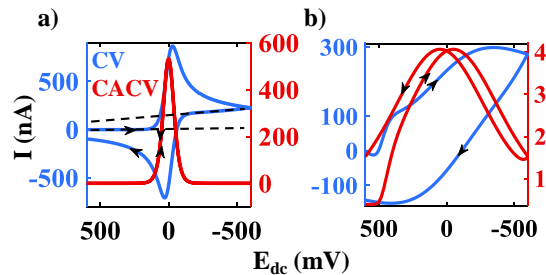


Fig. 2. Simulated CV shown in blue and CACV voltammograms shown in red for a single-electron reversible electrochemical reaction for a) an ideal electrochemical system; and b) a non-ideal electrochemical system (simulation parameters in Table I). Black arrows show the voltage scan direction and the dashed lines in a) show the baselines for the peak current estimation in the case of CV.

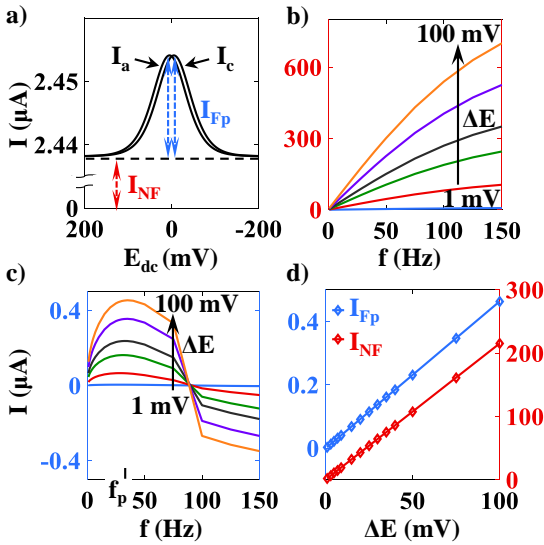
Table I shows the parameters used for simulating the ideal and non-ideal cases for both the CV and CACV, using FDTD. Fig.2 shows the simulated CV and CACV voltammograms for 1e-RER for two different systems. Fig.2(a) shows the result for an ideal electrochemical system, the output current being purely faradaic. The value of reduction potential was set to 0 V. Therefore, in the case of CV, the peak current in the forward and reversed sweeps were symmetrically positioned on either side of the 0 V with a separation of  $\approx 59$  mV, as expected [34]. In order to estimate the faradaic peak current, baseline current must be subtracted from the peak current. In this case, as the nonfaradaic current was zero, the baseline had only a residual current component. As expected, the ratio of the two peak currents after the baseline correction was found to be unity. However, in the case of CACV, the forward and reversed sweeps were overlapping with the peaks at 0 V. Therefore, the CACV peak potentials represent the reduction potential of the reaction. The ratio of the peak currents was unity, which is also a feature in CV for a typical 1e-RER. This is also evident from the full width at half maximum (FWHM) of the CACV voltammogram, which was calculated to be  $\approx 92.0$  mV, close to the expected value of 90.4 mV for 1e-RER [18].

Fig.2(b) shows the CV and CACV voltammograms for a non-ideal electrochemical system with the non-idealities introduced as a double-layer capacitance  $C_{dl}$ , uncompensated

resistance  $R_s$  as shown in Fig.1(c) and an additional DL resistance  $R_p$  in parallel to  $C_{dl}$ , with the values as given in Table I. This resulted in the output current consisting of faradaic along with a large nonfaradaic current component. In the case of CV, this resulted in increased separation between forward and reversed peak potentials [34]. Due to large nonfaradaic current, there was no clear baseline making the faradaic peak current determination difficult. On contrary, the CACV voltammogram showed lesser separation between the forward and reversed peak potentials. CACV voltammogram also shows an increase in FWHM compared to that in the ideal case. The value of both the peak currents were equal indicating that the reaction was electrochemically reversible, an information which could not be retrieved from the CV voltammogram. It is important to note that, in this case the CACV baseline is at finite current value, which was at 0 A in Fig.2(a), indicating that the baseline position corresponds to the magnitude of nonfaradaic current. This gives an added advantage to CACV over CV and has been discussed in the following sections.

### B. CACV parameters - On the choice of frequency and amplitude of modulation

The CACV performance depends on the input waveform and the system parameters. Fig.3 shows the effect of waveform parameters, *viz.*, modulating sinusoidal frequency 'f' and amplitude  $\Delta E$  on the magnitude of  $I_{Fp}$  and  $I_{NF}$  for system parameters  $R_s$  and  $C_{dl}$  given as  $100 \Omega$  and  $10 \mu\text{F}$ , respectively.



**Fig. 3. Effect of waveform parameters:** a) A typical CACV voltammogram of a reversible electrochemical reaction where  $I_{NF}$  and  $I_{Fp}$  are respectively the nonfaradaic current and faradaic peak current, estimated from the baseline marked by black dashed line; b) the effect of modulating sinusoidal frequency 'f' on  $I_{NF}$  for different sinusoidal amplitude  $\Delta E$ ; c) the effect of 'f' on  $I_{Fp}$  for different  $\Delta E$ ; and d) variation of  $I_{Fp}$  and  $I_{NF}$  with respect to  $\Delta E$  at the frequency of maximum peak current  $f_p$ .

Fig.3(a) shows a typical CACV voltammogram with different current components marked on it. Here, the forward and reversed sweep currents are respectively the cathodic ( $I_c$ ) and anodic ( $I_a$ ) currents with equal peak magnitudes,

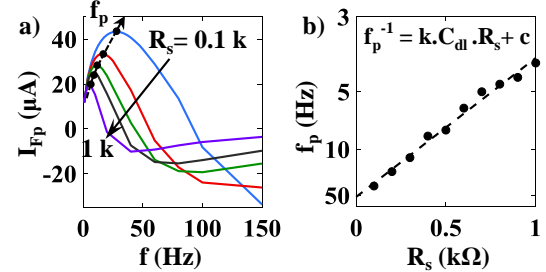
marked as peak faradaic current ( $I_{Fp}$ ). The baseline current is proportional to the nonfaradaic current and has been labelled as  $I_{NF}$ . Fig.3(b) shows the effect of 'f' on  $I_{NF}$  for different  $\Delta E$  where it was observed that  $I_{NF}$  increased monotonically with both 'f' and  $\Delta E$ . This can be explained from the Randles equivalent circuit model as shown in Fig.1(c). If we neglect the faradaic impedance, the circuit reduced to a simple series combination of  $R_s$  and  $C_{dl}$  with the impedance given by

$$Z_{nf} = R_s + \frac{1}{j2\pi f C_{dl}} \quad (13)$$

and thus the magnitude of  $I_{NF}$  can be given by

$$I_{NF} = \Delta E \times \left( R_s^2 + \frac{1}{(2\pi f C_{dl})^2} \right)^{-1/2} \quad (14)$$

Equation 14 clearly explains the trend of  $I_{NF}$  for different 'f' and  $\Delta E$  as shown in Fig.3(b). Fig.3(c) shows the effect of 'f' on  $I_{Fp}$  for different  $\Delta E$ . With increasing 'f',  $I_{Fp}$  initially increased sub-linearly till a particular frequency marked as  $f_p$  and decreased thereafter. However,  $I_{Fp}$ , similar to  $I_{NF}$ , increased monotonically with increasing  $\Delta E$ . Also, at the frequency  $f_p$ , both  $I_{Fp}$  and  $I_{NF}$  showed linear increase with increasing  $\Delta E$ , as shown in Fig.3(d) with slopes equal to the magnitude of their respective impedances. The observed nonlinear behaviour of  $I_{Fp}$  with respect to 'f' shown in Fig.3(c) can be explained from the equivalent circuit model as shown in Fig.1(c). The  $R_s$  and  $C_{dl}$  act as a RC low-pass filter across the faradaic element  $Z_f$ . Thus the effective  $\Delta E$  across  $Z_f$  decreases above the RC cutoff frequency, decreasing the  $I_{Fp}$  above the frequency  $f_p$ . Further increasing the frequency resulted in zero and then negative  $I_{Fp}$ . This was due to the fact that around the reduction potential, the nonfaradaic current  $I_{NF}$  experiences a dip due to decrease in effective  $C_{dl}$  [35], [36]. Hence, the estimated  $I_{Fp}$  is the difference of actual faradaic current and the magnitude of the dip in  $I_{NF}$ , which depending on frequency may be zero or negative. At very high frequency,  $I_{Fp}$  asymptotically converges to zero due to zero effective ac potential across  $Z_f$ .



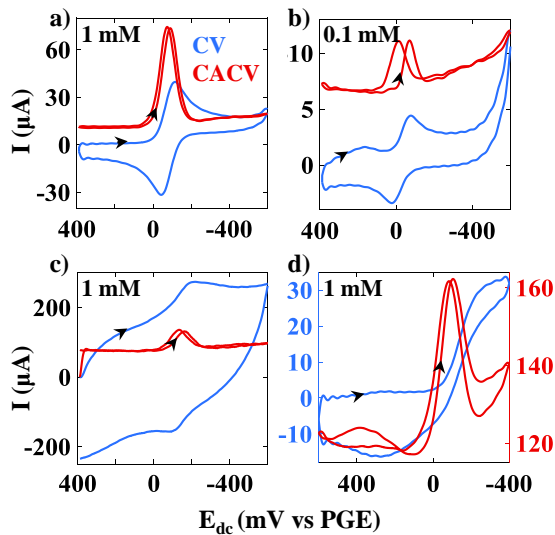
**Fig. 4. Effect of system parameters:** a) variation of peak faradaic current  $I_{Fp}$  with respect to modulating sinusoidal frequency 'f' for different series resistance  $R_s$ ; and b) variation of frequency of maximum peak current  $f_p$  with respect to  $R_s$ . The indicated expression was used for the linear fit, shown by black dashed line, to the simulated data points.

Fig.4(a) shows the effect of system parameter  $R_s$  on the frequency dependence of  $I_{Fp}$ , keeping all other simulation parameters unchanged. For a given value of  $R_s$ , the  $I_{Fp}$  initially increased with the increase in frequency up to  $f_p$  and decreased thereafter, a behaviour discussed above and shown

in Fig.3(c). With the increase in  $R_s$ , there was a decrease in the peak current and frequency  $f_p$ . Similar behaviour of  $I_{Fp}$  was observed for increasing  $C_{dl}$  (not shown here). Further, it was observed that  $f_p$  was not a function of any other parameters like analyte concentration, scan rate and diffusion coefficient. This affirms that  $f_p$  is closely related to the cutoff frequency of the RC low-pass filter in the Randles equivalent circuit. Fig.4(b) shows the dependence of  $f_p$  on  $R_s$  for  $C_{dl} = 10 \mu\text{F}$ , where  $f_p$  is plotted on inverse y-axis. The black dashed line shows the straight line fit to the relation indicated in the figure, which is similar to the RC low-pass filter behaviour. Therefore, in order to maximize the faradaic current, the modulation frequency should be within a range around  $f_p$ . In an ideal case,  $\Delta E$  should be as large as possible, limited by potential window of electrodes and reaction potential of the other species present in the system. However in practical cases, system currents do not follow linear relationship with  $\Delta E$  and in order to approximate this to a linear behaviour,  $\Delta E$  should be small, usually below 10 mV in experiments [37].

### C. Experimental demonstration of CACV - separation of faradaic & nonfaradaic currents at different temperatures

Fig.5 shows the experimental CV and CACV voltammograms of  $\text{K}_3\text{Fe}(\text{CN})_6$  in 0.1 M KCl as supporting electrolyte using PGE for all the three electrodes. Scan rate of 100 mV/s, modulating sinusoidal frequency  $f = 10 \text{ Hz}$  and sinusoidal amplitude  $\Delta E = 20 \text{ mV}$  were used for all the measurements.



**Fig. 5.** Experimental CV shown in blue and CACV voltammograms shown in red for a) 1 mM and b) 0.1 mM  $\text{K}_3\text{Fe}(\text{CN})_6$ ; c) 1 mM  $\text{K}_3\text{Fe}(\text{CN})_6$  with large nonfaradaic current due to high capacitance working electrode; and d) the system same as in (a) left undisturbed for 24 hours at ambient conditions. 0.5 mm pencil leads were used as pencil graphite electrodes (PGE) for all the three electrodes and 0.1 M KCl was used as supporting electrolyte. All the measurements were done at a scan rate of 100 mV/s. Modulating sinusoidal waveform of amplitude  $\Delta E = 20 \text{ mV}$  and frequency  $f = 10 \text{ Hz}$  were used for CACV measurements.

Fig.5(a) and (b) show the CV and CACV voltammograms for 1 mM and 0.1 mM concentration of  $\text{K}_3\text{Fe}(\text{CN})_6$  respectively. The CV voltammogram for 1 mM  $\text{K}_3\text{Fe}(\text{CN})_6$ , shown

in the Fig.5(a), showed the peak current of  $\approx 38.6 \mu\text{A}$ , with peaks symmetrically placed around -80 mV and ratio of  $\approx 1.04$  after baseline correction, confirming that the reaction is reversible. Due to the finite series resistance  $R_s$ , the separation between the peaks was  $\approx 71 \text{ mV}$ , slightly more than the case of ideal 1e-RER. The CACV voltammogram for this case showed peak current of  $\approx 62.7 \mu\text{A}$  at about -82 mV with ratio  $\approx 1.04$  and FWHM of  $\approx 93 \text{ mV}$  which was comparable to the simulation results. The baseline current was  $\approx 11 \mu\text{A}$ , giving the nonfaradaic current component. The CV voltammogram for 0.1 mM  $\text{K}_3\text{Fe}(\text{CN})_6$  shown in Fig.5(b), showed the current peaks symmetrically placed around -28 mV with separation  $\approx 91 \text{ mV}$ . In this case, though both the peaks were observed, the estimation of  $I_{Fp}$  was difficult due to distorted baseline. However, in the case of CACV, along with distinct current peaks, a clear baseline at  $\approx 6.7 \mu\text{A}$  was obtained. This facilitated the estimation of both the  $I_{Fp}$  and  $I_{NF}$  current components. Contrary to simulation, the baseline and hence  $I_{NF}$  in CACV showed a dependence on sweep voltage  $E_{dc}$ , which may be due to the variation in  $C_{dl}$  with  $E_{dc}$  [38]. At this concentration, a broad peak in CV voltammogram was observed at approximately 165 mV only in the forward sweep as shown in Fig.5(b), while this was absent or suppressed in the case of CACV. This peak of irreversible nature could possibly be due to processes like interference from the trace amount of impurities/contaminants in the electrode surface [39] or dissolved oxygen reduction reaction [40]. Fig.5(c) shows the CV and CACV voltammograms for 1 mM  $\text{K}_3\text{Fe}(\text{CN})_6$  using electrically annealed working electrode. In the case of CACV, it was observed that  $I_{Fp}$  was  $\approx 58.7 \mu\text{A}$  at around -148 mV with a dc shift in the CACV baseline indicating an increase in  $I_{NF}$  from  $\approx 11 \mu\text{A}$  in the case of unannealed electrode (shown in Fig.5(a)) to  $\approx 76 \mu\text{A}$ . Since, decrease in the PGE resistance was negligible, we attribute this increase in  $I_{NF}$  to increase in effective capacitance of the working electrode. The increase in  $I_{NF}$  for the case of CV resulted in baseline distortion, inhibiting the estimation of  $I_{Fp}$ . Similar effects were observed for increased resistance due to either increased working electrode resistance (added externally in series) or increased solution resistance (reduced supporting electrolyte concentration). In both these cases, an increase in  $I_{NF}$  and a decrease in  $I_{Fp}$  were observed due to the increased uncompensated resistance (figure not shown here for brevity). Fig.5(d) shows the CV and CACV voltammograms of the same system in Fig.5(a), left undisturbed for 24 hours at ambient conditions. In CV voltammogram, no current peak was observed. This may be due to the physical adsorption of  $\text{K}_3\text{Fe}(\text{CN})_6$  on electrodes, which prevented system to operate in diffusion limited region. The CACV voltammogram of this system showed both the forward and reversed peaks at around -92 mV with  $I_{Fp} \approx 40 \mu\text{A}$  and  $I_{NF} \approx 120 \mu\text{A}$ , compared to  $60 \mu\text{A}$  and  $11 \mu\text{A}$  respectively in Fig.5(a). The large increase in  $I_{NF}$  may be due to the increased DL capacitance of the working electrode. Therefore, CACV proves to be a potential method for the cases like continuous monitoring where adsorption on electrode surface is a common problem [41], [42].

Fig.6(a) shows the CACV voltammograms for different

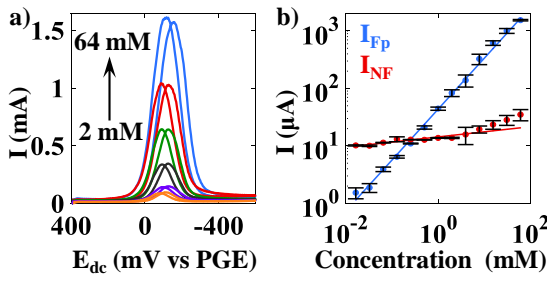


**Fig. 6.** a) Experimental CACV voltammograms for different concentrations of  $\text{K}_3\text{Fe}(\text{CN})_6$ ; and b) the extracted peak faradaic  $I_{Fp}$  and nonfaradaic  $I_{NF}$  currents for different concentrations. All the measurements were done using pencil graphite electrodes (PGE) at the scan rate of 100 mV/s, modulating sinusoidal frequency  $f = 10$  Hz and sinusoidal amplitude  $\Delta E = 20$  mV. Error bar in b) represents the 95% confidence interval based on one sample t-test ( $n=5$ ).

concentrations of  $\text{K}_3\text{Fe}(\text{CN})_6$  and Fig.6(b) shows the extracted current components  $I_{Fp}$  &  $I_{NF}$  for concentrations from 64 mM to 0.125 mM. The experimental results show linear increase in  $I_{Fp}$  with the increase in analyte concentration which is in good agreement with the simulation results.  $I_{NF}$  as expected was found to be almost insensitive to concentration with a slight increase due to change in  $C_{dl}$ . Five sets of experiments, with 10 cycles in each set were performed for 1 mM  $\text{K}_3\text{Fe}(\text{CN})_6$  / 0.1 M KCl to obtain peak faradaic  $I_{Fp}$  and nonfaradaic  $I_{NF}$  currents. From these experiments, it was observed that the coefficient of variation of the faradaic current in all sets of experiments was  $\leq 0.75\%$ . Thus, it can be concluded that while  $I_{NF}$  depends only on system parameters,  $I_{Fp}$  is sensitive to analyte concentration as well as system parameters. Therefore for a given system, it becomes difficult to uniquely attribute the change in  $I_{Fp}$  to either the change in analyte concentration or change in system parameter or both. At this point, estimation of  $I_{NF}$  can help to identify any change in system parameters, thereby resolving the ambiguity in origin of change in  $I_{Fp}$ .

The system parameters, specially for an on-site electrochemical sensor can change due to multiple unknown factors like, humidity, temperature and electrode fouling which can lead to error in the analyte analysis [17], [42], [43]. Fig.7 shows the effect of analyte concentration and temperature variation on CV and CACV measurements. For clarity, only forward sweep has been shown. In order to avoid any instability in the reference potential, standard Ag/AgCl in 3.5 M KCl was used as reference electrode. Fig.7(a) and (b) show the CV voltammograms respectively for varying concentration and temperature.  $I_{Fp}$  was observed to change whereas  $I_{NF}$  was almost constant in both the cases. This limits CV to differentiate between the two origins of change in  $I_{Fp}$ . Fig.7(c) and (d) show the CACV voltammograms for varying concentration and temperature respectively.  $I_{Fp}$  was observed to change in both the cases, whereas  $I_{NF}$  showed variation only in the case of temperature variation. Therefore change in  $I_{NF}$  can be used as an error indicator or as a secondary validation/correction factor in electrochemical sensors.

## V. CONCLUSIONS

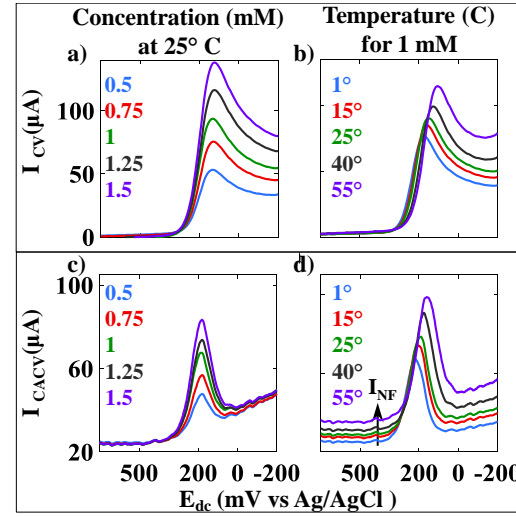


**Fig. 7.** CV voltammograms for a) five different concentrations of  $\text{K}_3\text{Fe}(\text{CN})_6$  at  $25^\circ\text{C}$  and b) at five different temperatures for 1 mM  $\text{K}_3\text{Fe}(\text{CN})_6$ . CACV voltammograms for c) five different concentrations of  $\text{K}_3\text{Fe}(\text{CN})_6$  at  $25^\circ\text{C}$  and d) at five different temperatures for 1 mM  $\text{K}_3\text{Fe}(\text{CN})_6$ .  $I_{NF}$  in d) shows the nonfaradaic current marked with black arrows.  $I_{NF}$  remained unchanged in CV whereas increased in the case of CACV with the increase in temperature. The electrochemical cell consisted of Ag/AgCl in 3.5 M KCl as the reference electrode and 0.5 mm pencil leads as working and counter electrodes. 0.1 M KCl was used as the supporting electrolyte. All the measurements were done at a scan rate of 100 mV/s. Modulating sinusoidal waveform of amplitude  $\Delta E = 20$  mV and frequency  $f = 10$  Hz were used for CACV measurements.

A new voltammetric method CACV was demonstrated which showed three-fold improvement over CV: i) showed 5 times better detection limit compared to that of CV due to a clear baseline; ii) CACV could isolate the effects of system parameter change on the sensor's reading due to simultaneous faradaic and nonfaradaic current estimation, making it a suitable choice for reliable on-field sensing prone to environmental changes; and iii) CACV was observed to be applicable even in the case of electrode fouling and thus has potential for continuous monitoring systems.

## ACKNOWLEDGMENT

The authors acknowledge the financial support from the Science and Engineering Research Board (SERB) and the Department of Science and Technology (DST) India, under the grant number EMR/2016/003506.

## REFERENCES

- [1] M. Labib, E. H. Sargent, and S. O. Kelley, "Electrochemical methods for the analysis of clinically relevant biomolecules," *Chemical reviews*, vol. 116, no. 16, pp. 9001–9090, Jul. 2016.
- [2] Y. Wang, H. Xu, J. Zhang, and G. Li, "Electrochemical sensors for clinic analysis," *Sensors*, vol. 8, no. 4, pp. 2043–2081, 2008.
- [3] A. Kumar, H. Kim, and G. P. Hancke, "Environmental monitoring systems: A review," *IEEE Sensors Journal*, vol. 13, no. 4, pp. 1329–1339, 2012.
- [4] G. Hanrahan, D. G. Patil, and J. Wang, "Electrochemical sensors for environmental monitoring: design, development and applications," *Journal of Environmental Monitoring*, vol. 6, no. 8, pp. 657–664, 2004.
- [5] Y. Cui, "Electronic Materials, Devices, and Signals in Electrochemical Sensors," *IEEE Transactions on Electron Devices*, vol. 64, no. 6, pp. 2467–2477, 2017.

- [6] N. Alizadeh, H. Jamalabadi, and F. Tavoli, "Breath acetone sensors as non-invasive health monitoring systems: A review," *IEEE Sensors Journal*, vol. 20, no. 1, pp. 5–31, 2019.
- [7] A. Nag, S. C. Mukhopadhyay, and J. Kosei, "Wearable flexible sensors: A review," *IEEE Sensors Journal*, vol. 17, no. 13, pp. 3949–3960, 2017.
- [8] A. J. Bard, L. R. Faulkner, J. Leddy, and C. G. Zoski, *Electrochemical methods: fundamentals and applications*, 2nd ed. New York, USA: Wiley New York, 1980, ch. 1, pp. 9–28.
- [9] J. A. Johnson, N. T. Rodeberg, and R. M. Wightman, "Measurement of basal neurotransmitter levels using convolution-based nonfaradaic current removal," *Analytical chemistry*, vol. 90, no. 12, pp. 7181–7189, 2018.
- [10] E. Grygolowicz-Pawlak and E. Bakker, "Background current elimination in thin layer ion-selective membrane coulometry," *Electrochemistry communications*, vol. 12, no. 9, pp. 1195–1198, 2010.
- [11] J. Tu, W. Cai, and X. Shao, "Enhancing the sensitivity of potential step voltammetry using chemometric resolution," *Analyst*, vol. 139, no. 5, pp. 1016–1022, 2014.
- [12] F. Scholz, "Voltammetric techniques of analysis: the essentials," *ChemTexts*, vol. 1, no. 4, p. 17, 2015.
- [13] W. Smirnov, N. Yang, R. Hoffmann, J. Hees, H. Obloh, W. Muller-Sebert, and C. E. Nebel, "Integrated all-diamond ultramicroelectrode arrays: optimization of faradaic and capacitive currents," *Analytical chemistry*, vol. 83, no. 19, pp. 7438–7443, 2011.
- [14] C. Zuliani and D. Diamond, "Opportunities and challenges of using ion-selective electrodes in environmental monitoring and wearable sensors," *Electrochimica Acta*, vol. 84, pp. 29–34, 2012.
- [15] S. Hwang, C. N. LaFratta, V. Agarwal, X. Yu, D. R. Walt, and S. Sonkusale, "Cmos microelectrode array for electrochemical lab-on-a-chip applications," *IEEE Sensors Journal*, vol. 9, no. 6, pp. 609–615, 2009.
- [16] C. Amatore, E. Maisonneau, and G. Simonneau, "Ultrafast cyclic voltammetry: performing in the few megavolts per second range without ohmic drop," *Electrochemistry communications*, vol. 2, no. 2, pp. 81–84, 2000.
- [17] G. Zhao and G. Liu, "A portable electrochemical system for the on-site detection of heavy metals in farmland soil based on electrochemical sensors," *IEEE Sensors Journal*, vol. 18, no. 14, pp. 5645–5655, 2018.
- [18] A. J. Bard, L. R. Faulkner, J. Leddy, and C. G. Zoski, *Electrochemical methods: fundamentals and applications*, 2nd ed. New York, USA: Wiley New York, 1980, ch. 7,10, pp. 275–301,388–406.
- [19] J. A. Johnson, C. N. Hobbs, and R. M. Wightman, "Removal of differential capacitive interferences in fast-scan cyclic voltammetry," *Analytical chemistry*, vol. 89, no. 11, pp. 6166–6174, 2017.
- [20] F. Ciepiela and M. Jakubowska, "Faradaic and capacitive current estimation by means of independent components analysis and 1 khz sampling," *Talanta*, vol. 170, pp. 158–164, 2017.
- [21] J. Tu, W. Cai, and X. Shao, "Direct separation of faradaic and double layer charging current in potential step voltammetry," *Talanta*, vol. 116, pp. 575–580, 2013.
- [22] J. Zhang, S.-X. Guo, A. M. Bond, and F. Marken, "Large-amplitude fourier transformed high-harmonic alternating current cyclic voltammetry: kinetic discrimination of interfering faradaic processes at glassy carbon and at boron-doped diamond electrodes," *Analytical chemistry*, vol. 76, no. 13, pp. 3619–3629, 2004.
- [23] A. P. O'Mullane, J. Zhang, A. Brajter-Toth, and A. M. Bond, "Higher harmonic large-amplitude fourier transformed alternating current voltammetry: analytical attributes derived from studies of the oxidation of ferrocenemethanol and uric acid at a glassy carbon electrode," *Analytical chemistry*, vol. 80, no. 12, pp. 4614–4626, 2008.
- [24] A. A. Sher, A. M. Bond, D. J. Gavaghan, K. Gillow, N. W. Duffy, S.-X. Guo, and J. Zhang, "Fourier transformed large amplitude square-wave voltammetry as an alternative to impedance spectroscopy: Evaluation of resistance, capacitance and electrode kinetic effects via an heuristic approach," *Electroanalysis*, vol. 17, no. 15-16, pp. 1450–1462, 2005.
- [25] Y. Uchida, E. Kätelhön, and R. G. Compton, "Linear sweep voltammetry with non-triangular waveforms: New opportunities in electroanalysis," *Journal of Electroanalytical Chemistry*, vol. 818, pp. 140–148, 2018.
- [26] ——, "Cyclic voltammetry with non-triangular waveforms: Electrochemically irreversible and quasi-reversible systems," *Journal of Electroanalytical Chemistry*, vol. 810, pp. 135–144, 2018.
- [27] D. Nardiello, C. Palermo, A. Natale, M. Quinto, and D. Centonze, "Pulsed amperometric detection at glassy carbon electrodes: A new waveform for sensitive and reproducible determination of electroactive compounds," *Analytica chimica acta*, vol. 894, pp. 1–6, 2015.
- [28] S.-M. Park and J.-S. Yoo, "Electrochemical impedance spectroscopy for better electrochemical measurements," *Analytical Chemistry*, vol. 75, no. 21, pp. 455 A – 461 A, 2003.
- [29] A. A. Rowe, A. J. Bonham, R. J. White, M. P. Zimmer, R. J. Yadgar, T. M. Hobza, J. W. Honea, I. Ben-Yaacov, and K. W. Plaxco, "Cheapstat: an open-source, "do-it-yourself" potentiostat for analytical and educational applications," *PloS one*, vol. 6, no. 9, 2011.
- [30] S. D. Adams, E. H. Doeven, K. Quayle, and A. Z. Kouzani, "Ministat: Development and evaluation of a mini-potentiostat for electrochemical measurements," *IEEE Access*, vol. 7, pp. 31903–31912, 2019.
- [31] A. J. Bard, L. R. Faulkner, J. Leddy, and C. G. Zoski, *Electrochemical methods: fundamentals and applications*, 2nd ed. New York, USA: Wiley New York, 1980, ch. 10, p. 383.
- [32] R. G. Compton, E. Laborda, and K. R. Ward, *Understanding voltammetry: simulation of electrode processes*. Imperial College Press, 2014.
- [33] ——, *Understanding voltammetry: simulation of electrode processes*. Imperial College Press, 2014.
- [34] N. Elgrishi, K. J. Rountree, B. D. McCarthy, E. S. Rountree, T. T. Eisenhart, and J. L. Dempsey, "A practical beginner's guide to cyclic voltammetry," *Journal of Chemical Education*, vol. 95, no. 2, pp. 197–206, 2018.
- [35] A. J. Bard, L. R. Faulkner, J. Leddy, and C. G. Zoski, *Electrochemical methods: fundamentals and applications*, 2nd ed. New York, USA: Wiley New York, 1980, ch. 10, p. 553.
- [36] K. J. Aoki, J. Chen, X. Zeng, and Z. Wang, "Decrease in the double layer capacitance by faradaic current," *RSC advances*, vol. 7, no. 36, pp. 22501–22509, 2017.
- [37] S. O. Engblom, J. C. Myland, and K. B. Oldham, "Must ac voltammetry employ small signals?" *Journal of Electroanalytical Chemistry*, vol. 480, no. 1-2, pp. 120–132, 2000.
- [38] J. Vatamanu, L. Cao, O. Borodin, D. Bedrov, and G. D. Smith, "On the influence of surface topography on the electric double layer structure and differential capacitance of graphite/ionic liquid interfaces," *Journal of Physical Chemistry Letters*, vol. 2, no. 17, pp. 2267–2272, 2011.
- [39] R. Navratil, A. Kotzianova, V. Halouzka, T. Opletal, I. Triskova, L. Trnkova, and J. Hrbac, "Polymer lead pencil graphite as electrode material: Voltammetric, xps and raman study," *Journal of Electroanalytical Chemistry*, vol. 783, pp. 152–160, 2016.
- [40] A. J. Bard, L. R. Faulkner, J. Leddy, and C. G. Zoski, *Electrochemical methods: fundamentals and applications*, 2nd ed. New York, USA: Wiley New York, 1980, ch. 10, p. 406.
- [41] B. L. Hanssen, S. Siraj, and D. K. Wong, "Recent strategies to minimise fouling in electrochemical detection systems," *Reviews in Analytical Chemistry*, vol. 35, no. 1, pp. 1–28, 2016.
- [42] P.-H. Lin and B.-R. Li, "Antifouling strategies in advanced electrochemical sensors and biosensors," *The Analyst*, 2020.
- [43] F. Usman, J. O. Dennis, A. Y. Ahmed, F. Meriaudeau, O. B. Ayodele, and A. A. Rabih, "A Review of Biosensors for Non-Invasive Diabetes Monitoring and Screening in Human Exhaled Breath," *IEEE Access*, vol. 7, pp. 5963–5974, 2019.

**Nirjhar Kumar** is a graduate student pursuing his M.S. and Ph.D. dual degree from Indian Institute of Technology Madras, Chennai, India. His present research interests include design and modelling electrochemical system, electrochemical-plasmonic imaging and biosensors.

**Ankit Arora** is a graduate student pursuing his PhD in electrical engineering at the Indian Institute of Technology, Madras (IIT-M). He obtained his MS degree in electrical engineering from IIT-M.

**Ananth Krishnan** is a faculty member at the Department of Electrical Engineering in the Indian Institute of Technology, Madras. He specializes in the design, fabrication, and characterization of plasmonic devices and applications.



## Research article

Ankit Arora, Pramoda K. Nayak, Tejendra Dixit, Kolla Lakshmi Ganapathi, Ananth Krishnan and Mamidanna Sri Ramachandra Rao\*

# Stacking angle dependent multiple excitonic resonances in bilayer tungsten diselenide

<https://doi.org/10.1515/nanoph-2020-0034>

Received January 15, 2020; accepted May 3, 2020; published online June 18, 2020

**Abstract:** We report on multiple excitonic resonances in bilayer tungsten diselenide ( $\text{BL-WSe}_2$ ) stacked at different angles and demonstrate the use of the stacking angle to control the occurrence of these excitations.  $\text{BL-WSe}_2$  with different stacking angles were fabricated by stacking chemical vapour deposited monolayers and analysed using photoluminescence measurements in the temperature range 300–100 K. At reduced temperatures, several excitonic features were observed and the occurrences of these excitonic resonances were found to be stacking angle dependent. Our results indicate that by controlling the stacking angle, it is possible to excite or quench higher order excitations to tune the excitonic flux in optoelectronic devices. We attribute the presence/absence of

multiple higher order excitons to the strength of interlayer coupling and doping effect from  $\text{SiO}_2/\text{Si}$  substrate. Understanding interlayer excitations will help in engineering excitonic devices and give an insight into the physics of many-body dynamics.

**Keywords:** 2D transition metal dichalcogenides; bilayer  $\text{WSe}_2$ ; excitonic device; many-body dynamics; multiple excitonic resonances; stacking angle.

**PACS:** 78.67.-n; 71.35.-y.

## 1 Introduction

Transition metal dichalcogenides (TMDs) with the chemical formula  $\text{MX}_2$  ( $\text{M}$  = transition metal and  $\text{X}$  = chalcogen) are a class of two-dimensional (2D) materials beyond graphene, which have attracted much attention recently because of their interesting optical properties [1, 2]. Monolayer (1L) TMDs are direct bandgap semiconductors with excellent quantum confinement, broken inversion symmetry and reduced dielectric screening resulting in the formation of strong coulomb bound electron-hole pair, called excitons [3, 4]. Hence, light-matter interactions in these systems are primarily governed by the excitonic effects, which have been exploited to develop exciton-based devices [5–9]. Apart from this two body complex, 1L-TMDs also exhibit higher-order excitations namely, three body complex called charged exciton or trion [10], four body complex called biexciton [11], and so on [12, 13]. These higher order excitations show distinct excitation power dependence [14–16], lifetime [11], spatial distribution [17, 18], and have specific spin-valley configurations [19–21] which make them useful for novel quantum optoelectronic applications. However, external control of these excitations in 1L-TMDs have remained a major challenge and restricted their practical applicabilities.

Bilayer (BL) systems comprising of two monolayers of same or different TMDs have drawn lots of interest towards designing novel quantum materials due to fascinating emergent properties [22–27]. The key control knob

\*Corresponding author: Mamidanna Sri Ramachandra Rao,  
Department of Physics and Materials Science Research Centre, Indian Institute of Technology Madras, Chennai, 600036, India, and Nano Functional Materials Technology Centre, Indian Institute of Technology Madras, Chennai, 600036, India,  
E-mail: msrrao@iitm.ac.in. <https://orcid.org/0000-0002-7806-2151>

**Ankit Arora:** Centre for NEMS and Nano Photonics, Department of Electrical Engineering, Indian Institute of Technology Madras, Chennai, 600036, India; Department of Physics and Materials Science Research Centre, Indian Institute of Technology Madras, Chennai, 600036, India; and Nano Functional Materials Technology Centre, Indian Institute of Technology Madras, Chennai, 600036, India.  
<https://orcid.org/0000-0003-4899-1336>

**Pramoda K. Nayak and Kolla Lakshmi Ganapathi:** Department of Physics and Materials Science Research Centre, Indian Institute of Technology Madras, Chennai, 600036, India,  
E-mail: pnayak@iitm.ac.in (P.K. Nayak)

**Tejendra Dixit:** Department of Physics and Materials Science Research Centre, Indian Institute of Technology Madras, Chennai, 600036, India; Department of Electronics and Communication Engineering, Indian Institute of Information Technology D&M, Kancheepuram, Chennai, 600127, India

**Ananth Krishnan:** Centre for NEMS and Nano Photonics, Department of Electrical Engineering, Indian Institute of Technology Madras, Chennai, 600036, India, E-mail: ananthk@iitm.ac.in

for designing these materials is the stacking angle dependent interlayer coupling which can be used as an external degree of freedom to tune their optical and electronic properties [28–31]. Recently, electrically controlled excitonic switching has been demonstrated in BL-TMDs due to the formation of interlayer excitonic species [32–34]. Although some initial work has been done to explore many body effects in BL-TMDs [28, 35, 36], most of these demonstrations are limited only to neutral excitons. However, for better flux control and efficient device applications, it is important to understand all the higher order excitations and their stacking angle dependence in BL-TMD systems.

In the present work, we report on multiple excitonic resonances in BL-WSe<sub>2</sub> on SiO<sub>2</sub>/Si substrate stacked at different angles, using temperature dependent photoluminescence (PL) measurements. At temperature ~100 K, the presence or absence of these resonances showed strong stacking angle dependence. Excitation power dependent PL measurements confirmed the nature of these resonances as higher order excitations, such as trions and biexcitons, along with neutral excitons. The emission intensities and the peak positions of these higher order excitations, relative to that of the neutral exciton, showed a systematic stacking angle dependence. These observations demonstrated the interlayer nature of these excitations and were attributed to stacking angle dependent interlayer distance and doping efficiency from SiO<sub>2</sub>/Si substrate. This study provides an ideal platform for understanding interlayer excitations in BL-TMD systems for engineering excitonic devices and gives an insight into the physics of the many-body dynamics.

## 2 Materials and methods

Monolayer (1L) WSe<sub>2</sub> flakes were grown on sapphire (001) substrate using low pressure chemical vapour deposition (LPCVD) as reported earlier [37]. The as grown 1L-WSe<sub>2</sub> flakes on sapphire substrate were transferred onto SiO<sub>2</sub>/Si substrate with 300 nm oxide thickness using polymethyl methacrylate (PMMA) based transfer process [37]. For the second layer transfer, 1L-WSe<sub>2</sub>/SiO<sub>2</sub>/Si was used as the substrate in place of SiO<sub>2</sub>/Si. In order to reduce any inhomogeneity in the overlapping region caused due to the transfer process, samples were annealed at ~600 K for 1 h in Argon atmosphere [37]. As the transfer process was random, bilayer (BL) systems with several stacking angles were obtained and are shown in Fig.S1 of the supplementary information. Stacking angle was measured as clockwise orientation of the top layer with respect to bottom layer with an accuracy of ~2°. Due to three-fold symmetry of WSe<sub>2</sub> flakes, BL-WSe<sub>2</sub> stacked at angles 0° and 60° have minimum steric hindrance and hence maximum interlayer interaction, while those stacked at angles around 30° have maximum steric hindrance and hence minimum interlayer interaction [28, 29]. Therefore, from several fabricated BL systems, one with asymmetrically stacked at angle 36° and two with symmetrically stacked at angles 0° and 60° were selected for further studies, their corresponding scanning electron microscopy (SEM) images and schematics are shown in Figure 1. The atomic force microscopy measurements using Park Systems NX10 were carried out to determine the thickness of WSe<sub>2</sub> flakes as shown in Fig. S2. An edge step height ~0.9 nm at the substrate-bottom layer interface and ~0.7 nm at the bottom layer-top layer interface corresponds to thickness of the two constituent 1L-WSe<sub>2</sub>. These BL-WSe<sub>2</sub> systems were characterized using room temperature (RT) Raman and temperature dependent PL using a HORIBA LabRAM confocal micro-PL system in back scattering geometry. A laser of wavelength 488 nm, spot size ~1 μm and tunable optical power from ~0.3 to 300 μW was used as the excitation source. For RT measurements, 100× objectives were used while for low temperature measurements, long working distance 50× objectives were used. All the PL and Raman spectroscopy measurements of BL-WSe<sub>2</sub> samples were carried out at three different locations in the overlap region.

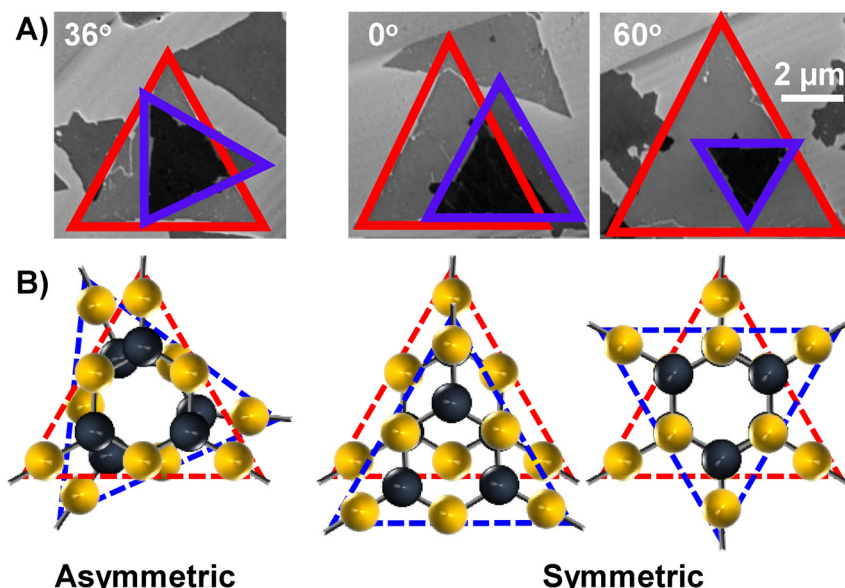


**Figure 1:** (A) SEM images and (B) Schematic of BL-WSe<sub>2</sub> with asymmetric (36°) and symmetric (0° and 60°) stacking angles. Monolayers marked in red and blue triangles are the bottom and the top layers respectively. Black spheres represent W atoms and yellow spheres represent Se atoms. The schematics have been drawn considering the two centrosymmetric triangles.

### 3 Results and discussion

As grown 1L-WSe<sub>2</sub> flakes on sapphire and post-transfer on SiO<sub>2</sub>/Si were characterized for their optical properties using PL measurements. The RT PL peak of as grown pristine 1L-WSe<sub>2</sub> on sapphire was observed at ~1.59 eV which shifted to ~1.66 eV after transfer to SiO<sub>2</sub>/Si substrate due to the stress release and bandgap renormalization after the transfer [38]. Figure 2A shows the RT PL spectra of 1L and the three BL-WSe<sub>2</sub> on SiO<sub>2</sub>/Si. The peak PL intensity for all the BL systems was approximately half the intensity of 1L-WSe<sub>2</sub> with negligible change in the peak position. This reduction in the PL intensity was due to the transition from direct bandgap in monolayer to partial indirect bandgap nature in BL systems [28, 39]. Interestingly, these spectra did not show any significant stacking angle dependence. Figure 2B shows the low frequency RT Raman spectra of BL-WSe<sub>2</sub> for different stacking angles. The red curve corresponding to the 60° stacking, shows two modes at ~17.3 and ~29.5 cm<sup>-1</sup> which can be attributed respectively to the in-plane shear mode (SM) and out-of-plane layer breathing mode (LBM) [40, 41]. However, in the case of 0° stacking, shown in blue, SM was absent and only LBM was observed, with a slight red shift and peak broadening. The absence of SM was due to its high sensitivity to the atomic alignment and the red shift in LBM was due to reduced restoring force between the layers [41–43]. In the case of 36° stacking, both these modes were quenched due to the lack of strong interlayer interaction. The low frequency Raman spectrum of 1L-WSe<sub>2</sub>, shown in black, showed a peak close to 20 cm<sup>-1</sup>, whose origin is not yet clear and can be attributed to resonant effect arising due to 488 nm excitation wavelength [37]. A similar peak has earlier been reported in MoS<sub>2</sub> at 38 cm<sup>-1</sup> for 632 nm excitation [44]. Figure 2C shows the RT Raman spectra of BL-WSe<sub>2</sub> for different stacking angles at higher frequencies. The peak at ~250 cm<sup>-1</sup> can be attributed to E<sub>2g</sub> modes and at ~260 cm<sup>-1</sup> to the second order 2LA(M) mode [45]. These modes were found to be relatively

insensitive to the stacking angle. A weak peak at ~308 cm<sup>-1</sup> was observed in all the bilayer systems which corresponds to the out-of-plane interlayer coupling mode A''<sub>2</sub> and hence was absent in 1L-WSe<sub>2</sub> [45].

Since RT PL spectra were found to be insensitive to stacking angle, temperature dependent PL measurements down to 100 K, were carried out on these BL systems and the corresponding spectra are shown in Fig.S3. It was observed that, with the reduction in temperature, there was a blue shift and a gradual reduction in the PL intensity of 1L as well as all the BL-WSe<sub>2</sub> systems, which can be attributed to the presence of optically dark exciton in WSe<sub>2</sub> [46, 47]. Further, at temperatures below 150 K, the PL line shape of asymmetrically and symmetrically stacked BL-WSe<sub>2</sub> systems were different. Figure 3A shows the PL spectrum of asymmetrically stacked BL-WSe<sub>2</sub> at 100 K obtained using 66 μW excitation power. The PL spectrum clearly showed the emergence of distinct emission features which indicated the presence of multiple excitonic states. Deconvolution of the PL spectrum into the constituent Gaussian curves showed three dominant peaks marked as X<sub>0</sub> (red), X<sub>1</sub> (green), and X<sub>2</sub> (blue). Similar excitonic features were observed in the case of 1L-WSe<sub>2</sub> on SiO<sub>2</sub>/Si but were absent in the case of 1L-WSe<sub>2</sub> on sapphire substrate as shown in the inset of Figure 3A. Therefore, it can be inferred that the emergence of these distinct emission features was a substrate dependent effect, in this case, due to the excess carriers from SiO<sub>2</sub>/Si substrate coming from the interface impurities or dangling bonds resulting in the doping of WSe<sub>2</sub> flakes [28, 38, 48].

In order to understand the nature of these excitonic states, power dependent PL measurements were performed with the excitation power (P<sub>Ex</sub>) varying from 0.03 to 240 μW. A broad low energy emission for P<sub>Ex</sub> ~0.03 μW was observed as shown in Fig. S4, which was negligible for higher P<sub>Ex</sub> and can be attributed to localized excitons [15]. Figure 3B shows the logarithmic plot of the PL intensities (I)

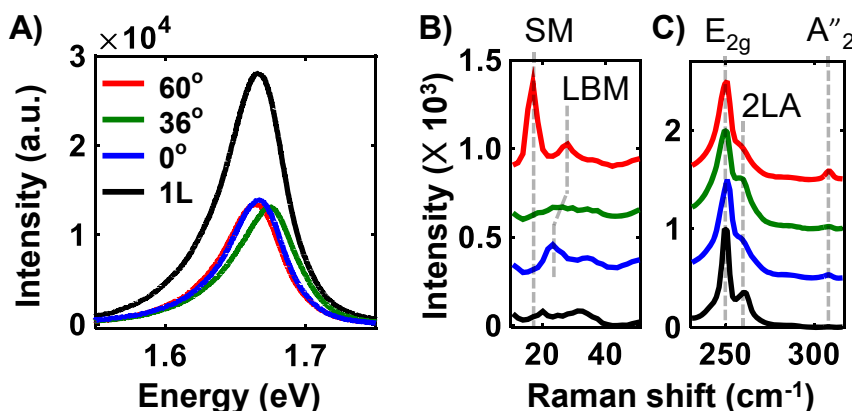


**Figure 2:** (A) Room temperature PL spectra; (B) Low frequency Raman spectra and (C) High frequency Raman spectra of 1L and BL-WSe<sub>2</sub> for different stacking angles. The characteristic low frequency shear mode (SM) and layer breathing mode (LBM) and higher frequency E<sub>2g</sub>, 2LA, and A''<sub>2</sub> modes are marked with vertical dashed lines.

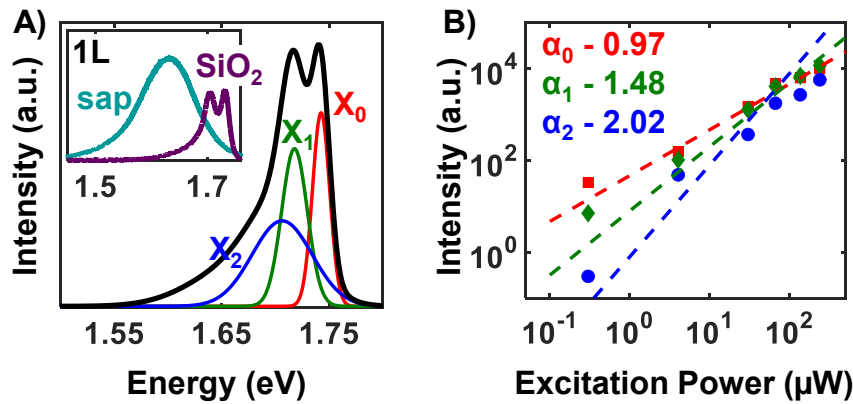


**Figure 3:** Asymmetrically stacked BL-WSe<sub>2</sub> (36°): (A) PL spectrum (black) at 100 K, obtained using 66 μW 488 nm excitation. The constituent deconvolved peaks are marked as X<sub>0</sub> (red) at ~1.74 eV, X<sub>1</sub> (green) at ~1.72 eV, and X<sub>2</sub> (blue) at ~1.70 eV. The inset shows the PL spectra of 1L-WSe<sub>2</sub> on sapphire (sap) and post-transfer on SiO<sub>2</sub>/Si substrate at 100 K; and (B) Excitation power dependence of X<sub>0</sub>, X<sub>1</sub>, and X<sub>2</sub> and their fit to the power law  $I \propto P_{Ex}^a$ .

for different excitation power ( $P_{Ex}$ ) of the peaks marked in Figure 3A and their fit to the power law  $I \propto P_{Ex}^a$ . The slope of the power law fit corresponds to  $\alpha$  and has been indicated in the figure. The peak marked as X<sub>0</sub> at ~1.74 eV showed almost linear dependence on  $P_{Ex}$  with  $\alpha \sim 0.97$  and hence can be attributed to neutral exciton [14]. The PL intensities of the other two peaks were observed to increase more steeply with  $P_{Ex}$ , thereby indicating their origin to be higher order excitons. The peak marked as X<sub>1</sub> at ~1.72 eV showed super-linear behaviour with  $\alpha \sim 1.48$  which is a characteristic of the three body complex called trion, consisting of a hole and two electrons [15, 38]. Excess carries from SiO<sub>2</sub>/Si resulted in higher electron density in BL-WSe<sub>2</sub> thereby increasing the probability of a neutral exciton to interact with an electron resulting in a negative trion with binding energy ~20 meV. The peak at ~1.70 eV marked as X<sub>2</sub> showed quadratic behaviour with  $\alpha \sim 2.02$  for  $P_{Ex} < 100 \mu\text{W}$ , however became almost linear for higher  $P_{Ex}$ . Based on its quadratic dependence on the excitation power and its position ~40 meV below the neutral exciton, the peak X<sub>2</sub> can be attributed to the four body complex called biexciton [36]. The emission intensity saturation at higher  $P_{Ex}$  was due to non-radiative decay channel, such as exciton-exciton annihilation at high exciton density [49]. These emission properties of the asymmetrically stacked BL-WSe<sub>2</sub>, that is, the peak positions, binding energies, and the power dependence of the neutral exciton, negative trion, and biexciton are similar to that of the 1L-WSe<sub>2</sub>. This indicates that, though there is some interlayer interaction between the constituent layers, the asymmetrically stacked BL system is equivalent to two 1L systems. However, the case of symmetrically stacked BL systems were strikingly different from their constituent monolayers and also from that of asymmetrically stacked one.

Figure 4A,C show the PL spectra of the two symmetrically stacked BL-WSe<sub>2</sub>, stacked at 0° and 60° at 100 K,

obtained using 66 μW excitation power. These PL spectra showed the emergence of several distinct emission features and a red shift of ~10 meV with respect to the asymmetrically stacked system. The three peaks labelled as X<sub>0</sub> (red), X<sub>1</sub> (green), and X<sub>2</sub> (blue) correspond to the ones observed in the case of asymmetric stacking, namely, the neutral exciton, negative trion and the biexciton. However, from I versus  $P_{Ex}$  plots shown in Figure 4B,D, it was observed that the  $P_{Ex}$  dependence of the neutral exciton was reduced to sub-linear from linear and that of the biexciton reduced to 1.28 (1.06) for 60° (0°) from quadratic in the asymmetric case. Moreover, the peaks X<sub>3</sub> to X<sub>5</sub> labelled in Figure 4A,C were not observed in the asymmetrically stacked BL system. The peak marked as X<sub>3</sub>, based on its position at 1.65 eV and its super-linear  $P_{Ex}$  dependence of ~1.24 (1.13) for 0° (60°) as shown in Fig. S5, may be assigned to the exciton-trion complex also known as charged biexciton [12, 13]. This negatively charged five body complex consists of two holes and three electrons with specific spin-valley configuration. Since, the two valence-band holes residing in the same valley is energetically unfavourable, the only possible configuration would consist of a negative-trion bound to an exciton residing in different valleys [13]. Emission peaks at 1.60 eV and below in both the symmetrically stacked systems may be attributed to indirect and localized excitons [39, 15]. Another feeble peak between X<sub>2</sub> and X<sub>3</sub> in the case of 60° was observed, its exact origin is still under investigation. It should be pointed here that the possibility of the formation of moiré superlattice due to the angle measurement tolerance of ~2° can be ignored as this effect for TMDs are known to be pronounced for angles  $\geq 3.1^\circ$  [50, 51]. Also, the PL measurements at three different locations on the overlapping region were observed to be consistent with an intensity variation within the experimental limits, indicating absence of regions of different stacking created due to moiré superlattice [42]. However, no atomic resolution images were obtained and no local

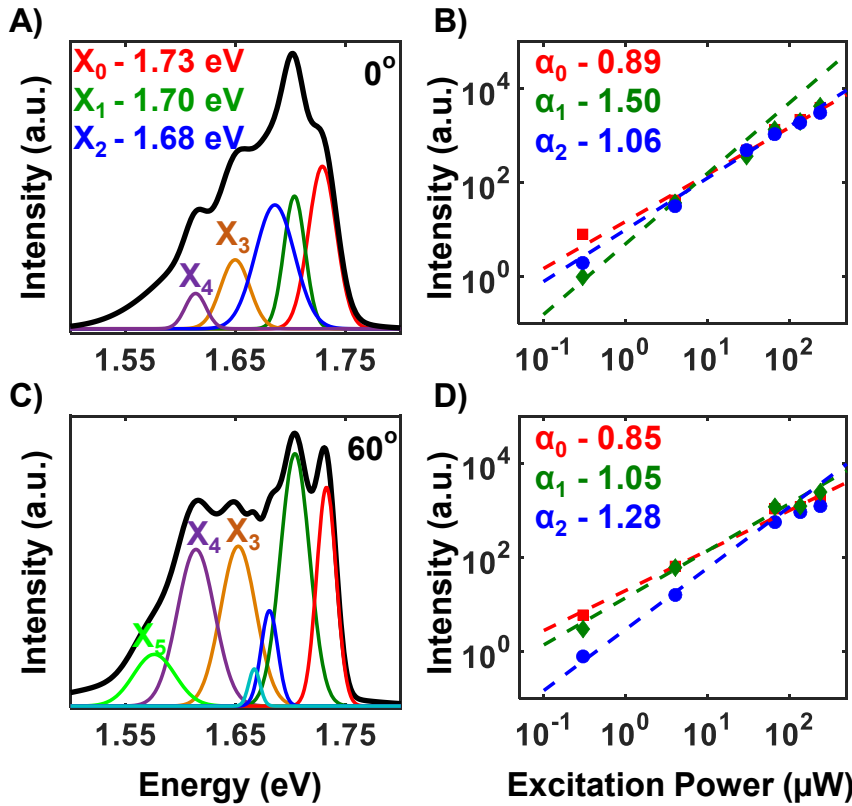


**Figure 4:** Symmetrically stacked BL-WSe<sub>2</sub>: (A & C) PL spectrum (black) at 100 K obtained using 488 nm, 66  $\mu$ W excitation for 0° and 60° respectively. The constituent deconvolved peaks are marked from X<sub>0</sub> to X<sub>5</sub>; and (B & D) Excitation power dependence of peaks marked as X<sub>0</sub>, X<sub>1</sub>, and X<sub>2</sub> for 0° and 60° respectively, and their fit to the power law  $I \propto P_{Ex}^{\alpha}$ .

probe measurements were done on the fabricated bilayer samples as this was beyond the scope of this work.

Therefore, from these observations it evident that the emission properties and presence/absence of different excitonic states in BL-WSe<sub>2</sub> system is highly sensitive to the stacking angle. Figure 5A shows the intensity ratios and the binding energies of X<sub>1</sub> and X<sub>2</sub> of the three BL systems. The intensity ration was calculated as the peak emission intensity normalized with their respective neutral exciton intensity. The contribution of both the higher order excitons is more in the case of symmetrically stacked system when

compared to the asymmetrically stacked one. Also, it can be noted that for symmetrically stacked systems, the binding energies of X<sub>1</sub> and X<sub>2</sub> were 30 and 50 meV respectively, which were reduced to 20 and 40 meV in the case of asymmetric stacking. These observed differences may be attributed mainly to two effects: (i) the interlayer coupling and (ii) doping from the substrate. Firstly, due to steric hindrance in the case of asymmetrically stacked BL-WSe<sub>2</sub>, the interlayer distance is ~0.72 nm, as calculated theoretically in earlier reported work, which reduces to ~0.65 nm for symmetrically stacked one [52]. This reduction in interlayer

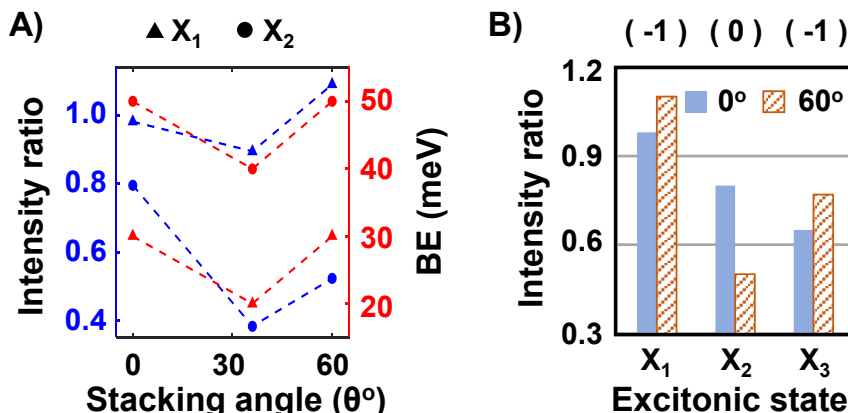


**Figure 5:** (A) Intensity ratio (the peak emission intensity normalized with respect to the intensity of neutral exciton) and the binding energies (BE) in meV of trion (X<sub>1</sub>) marked as ▲ and biexciton (X<sub>2</sub>) marked as ● of BL-WSe<sub>2</sub> with different stacking angles at 100 K; and (B) Intensity ratio of trion (X<sub>1</sub>), biexciton (X<sub>2</sub>), and charged-biexciton (X<sub>3</sub>) of BL-WSe<sub>2</sub> stacked at 0° and 60° at 100 K. Top axis shows the charge of the species X<sub>1</sub>, X<sub>2</sub>, and X<sub>3</sub> as -1, 0, or neutral and -1 respectively.

distance would result in larger van der Walls force, stronger interlayer coupling and higher exciton density. Secondly, the doping effect from the SiO<sub>2</sub>/Si substrate has earlier been shown to depend on the stacking angle [28]. The excess electron transfer from SiO<sub>2</sub>/Si is more efficient for stronger interlayer coupling and therefore is maximum in the case of symmetric stacking compared to that in the asymmetric case. These two effects together would give rise to increased carrier density and hence multiple higher order excitonic states in the symmetrically stacked BL systems and quench them in the asymmetrically stacked ones. Further, from a closer analysis of the two symmetrically stacked cases, it can be inferred that the difference in the PL spectrum is mainly due to the difference in relative contributions from the different excitonic states. It was observed that the relative contribution of the charged species, viz., trion and charged biexciton was more in 60° stacking while the neutral biexciton was more in 0° stacking, as shown in Figure 5B. This indicates that the doping effect is more in the case of the 60° compared to that in 0° stacking.

## 4 Conclusions

In conclusion, multiple excitonic resonances were observed in BL-WSe<sub>2</sub> from temperature dependent PL measurements down to 100 K. The evolution of these excitonic resonances was found to be sensitive to the stacking angle i. e. appear in case of high symmetric stacking, 0° and 60° and disappear in the case of asymmetric stacking, here 36°, an intermediate angle. Excitation power dependent PL measurements at 100 K confirmed the nature of these resonances as higher order excitations such as trions and biexcitons, along with neutral excitons. These higher order excitations showed interlayer nature and their occurrence were attributed to stacking angle dependent interlayer coupling and doping efficiency from SiO<sub>2</sub>/Si substrate. This work provides an ideal platform for understanding interlayer excitations in BL-TMD systems for engineering excitonic devices and give an insight into the physics of the many-body dynamics.

**Acknowledgment:** This work was partially supported by the Department of Science and Technology, Government of India (DST-GoI) that led to the establishment of Nano Functional Materials Technology Centre (NFMTC) (SR/NM/NAT/02-2005 and DST/NM/JIIT-01/2016(C)). P.K.N. acknowledge the financial support from DST-GoI, with sanction order no. SB/S2/RJN-043/2017 under Ramanujan Fellowship. K.L.G. acknowledge the financial support from DST-GoI, with sanction order no. DST/

INSPIRE/04/2016/001865 under DST INSPIRE Faculty program.

**Author contribution:** All the authors have accepted responsibility for the entire content of this submitted manuscript and approved submission.

**Research funding:** This research was funded by the Department of Science and Technology, Government of India (DST-GoI) that led to the establishment of Nano Functional Materials Technology Centre (NFMTC) (SR/NM/NAT/02-2005 and DST/NM/JIIT-01/2016(C)).

**Employment or leadership:** None declared.

**Honorarium:** None declared.

**Conflict of interest statement:** The authors declare no conflicts of interest regarding this article.

## References

- [1] K. F. Mak, and J. Shan, *Nat. Photon.*, vol. 10, pp. 216, 2016.
- [2] S. Manzeli, D. Ovchinnikov, D. Pasquier, O. V. Yazyev, and A. Kis, *Nat. Rev. Mater.*, vol. 2, pp. 17033, 2017.
- [3] J. Xiao, M. Zhao, Y. Wang, and X. Zhang, *Nanophotonics*, vol. 6, pp. 1309, 2017.
- [4] G. Wang, A. Chernikov, M. M. Glazov, et al., *Rev. Modern Phys.*, vol. 90, 2018, 021001.
- [5] T. Mueller, and E. Malic, *npj 2D Mater. Applic.*, vol. 2, pp. 1, 2018.
- [6] D. Jariwala, V. K. Sangwan, L. J. Lauhon, T. J. Marks, and M. C. Hersam, *ACS Nano*, vol. 8, pp. 1102, 2014.
- [7] J. Pu, and T. Takenobu, *Adv. Mater.*, vol. 30, pp. 1707627, 2018.
- [8] C. Chakraborty, L. Kinnischtke, K. M. Goodfellow, R. Beams, and A. N. Vamivakas, *Nat. Nanotechnol.*, vol. 10, pp. 507, 2015.
- [9] C. Palacios-Berraquero, M. Barbone, D. M. Kara, et al., *Nat. Commun.*, vol. 7, pp. 12978, 2016.
- [10] K. F. Mak, K. He, C. Lee, et al., *Nat. Mater.*, vol. 12, pp. 207, 2013.
- [11] Y. You, X. X. Zhang, T. C. Berkelbach, M. S. Hybertsen, D. R. Reichman, and T. F. Heinz, *Nat. Phys.*, vol. 11, pp. 477, 2015.
- [12] S. Y. Chen, T. Goldstein, T. Taniguchi, K. Watanabe, and J. Yan, *Nat. Commun.*, vol. 9, pp. 3717, 2018.
- [13] Z. Li, T. Wang, Z. Lu, et al., *Nat. Commun.*, vol. 9, 2018, <https://doi.org/10.1038/s41467-018-05863-5>.
- [14] D. Kaplan, Y. Gong, K. Mills, et al., *2D Mater.*, vol. 3, 2016, Art no. 015005, <https://doi.org/10.1088/2053-1583/3/1/015005>.
- [15] J. Huang, T. B. Hoang, and M. H. Mikkelsen, *Sci. Rep.*, vol. 6, pp. 22414, 2016.
- [16] M. Barbone, A. R.P. Montblanch, D. M. Kara, et al., *Nat. Commun.*, vol. 9, pp. 3721, 2018.
- [17] T. Kato, and T. Kaneko, *ACS Nano*, vol. 10, pp. 9687, 2016.
- [18] Y. Lee, S. J. Yun, Y. Kim, et al., *Nanoscale*, vol. 9, pp. 2272, 2017.
- [19] E. J. Sie, A. J. Frenzel, Y.H. Lee, J. Kong, and N. Gedik, *Phys. Rev. B* vol. 92, pp. 125417, 2015.
- [20] G. Plechinger, P. Nagler, A. Arora, et al., *Nat. Commun.*, vol. 7, pp. 12715, 2016.
- [21] K. Hao, J. F. Specht, P. Nagler, et al., *Nat. Commun.*, vol. 8, pp. 15552, 2017.
- [22] Y. Wang, C. Cong, J. Shang, et al., *Nanoscale Horizons*, vol. 4, pp. 396, 2019.
- [23] S. Das, G. Gupta, and K. Majumdar, *Phys. Rev. B*, vol. 99, pp. 165411, 2019.

- [24] I. C. Gerber, E. Courtade, S. Shree, et al., *Phys. Rev. B*, vol. 99, 2019, Art no. 035443, <https://doi.org/10.1103/PhysRevB.99.035443>.
- [25] C. Jin, E. Y. Ma, O. Karni, E. C. Regan, F. Wang, and T. F. Heinz, *Nat. Nanotechnol.*, vol. 13, pp. 994, 2018.
- [26] Z. Wang, Y. H. Chiu, K. Honz, K. F. Mak, and J. Shan, *Nano Lett.*, vol. 18, pp. 137, 2017.
- [27] A. M. Jones, H. Yu, J. S. Ross, et al., *Nat. Phys.*, vol. 10, pp. 130, 2014.
- [28] S. Huang, X. Ling, L. Liang, et al., *Nano Lett.*, 14, pp. 5500, 2014.
- [29] A. M. van Der Zande, J. Kunstmamn, A. Chernikov, et al., *Nano Lett.*, vol. 14, pp. 3869, 2014.
- [30] S. Zheng, L. Sun, X. Zhou, et al., *Adv. Opt. Mater.*, vol. 3, pp. 1600, 2015.
- [31] W. T. Hsu, B. H. Lin, L. S. Lu, et al., *Sci. Adv.*, vol. 5, 2019, <https://doi.org/10.1126/sciadv.aax7407>.
- [32] D. Unuchek, A. Ciarrocchi, A. Avsar, K. Watanabe, T. Taniguchi, and A. Kis, *Nature*, vol. 560, pp. 340, 2018.
- [33] A. Ciarrocchi, D. Unuchek, A. Avsar, K. Watanabe, T. Taniguchi, and A. Kis, *Nat. Photonics*, vol. 13, pp. 131, 2019.
- [34] M. Tahir, P. Krstajić, and P. Vasilopoulos, *Phys. Rev. B*, vol. 98, 2018, Art no. 075429, <https://doi.org/10.1103/PhysRevB.98.075429>.
- [35] T. Deilmann, and K. S. Thygesen, *Nano Lett.*, vol. 18, pp. 1460, 2018.
- [36] Z. He, W. Xu, Y. Zhou, et al., *ACS Nano*, vol. 10, pp. 2176, 2016.
- [37] P. K. Nayak, Y. Horbatenko, S. Ahn, et al., *Acs Nano*, vol. 11, pp. 4041, 2017.
- [38] S. Lippert, L. M. Schneider, D. Renaud, et al., *2D Mater.*, vol. 4, 2017, Art no. 025045, <https://doi.org/10.1088/2053-1583/aa5b21>.
- [39] W. Zhao, R. M. Ribeiro, M. Toh, et al., *Nano Lett.*, vol. 13, pp. 5627, 2013.
- [40] A. A. Puretzky, L. Liang, X. Li, et al., *ACS Nano*, vol. 9, pp. 6333, 2015.
- [41] C. H. Lui, Z. Ye, C. Ji, et al., *Phys. Rev. B*, vol. 91, pp. 165403, 2015.
- [42] S. Huang, L. Liang, X. Ling, et al., *Nano Lett.*, vol. 16, pp. 1435, 2016.
- [43] A. A. Puretzky, L. Liang, X. Li, et al., *ACS Nano*, vol. 10, pp. 2736, 2016.
- [44] J. U. Lee, J. Park, Y. W. Son, and H. Cheong, *Nanoscale*, vol. 7, pp. 3229, 2015.
- [45] W. Zhao, Z. Ghorannevis, K. K. Amara, et al., *Nanoscale*, vol. 5, pp. 9677, 2013.
- [46] X.-X. Zhang, Y. You, S. Y. F. Zhao, and T. F. Heinz, *Phys. Rev. Lett.*, 115, pp. 257403, 2015.
- [47] A. Arora, T. Dixit, K. Anil Kumar, et al., *Appl. Phys. Lett.*, vol. 114, pp. 201101, 2019.
- [48] M. Drüppel, T. Deilmann, P. Krüger, and M. Rohlfing, *Nat. Commun.*, vol. 8, pp. 2117, 2017.
- [49] D. Sun, Y. Rao, G. A. Reider, et al., *Nano Lett.*, vol. 14, pp. 5625, 2014.
- [50] M. H. Naik, and M. Jain, *Phys. Rev. Lett.*, vol. 121, pp. 266401, 2018.
- [51] L. Wang, E. M. Shih, A. Ghiotto, et al., *arXiv preprint arXiv: 1910.12147*, 2019.
- [52] J. He, K. Hummer, and C. Franchini, *Phys. Rev. B*, vol. 89, 2014, Art no. 075409, <https://doi.org/10.1103/PhysRevB.89.075409>.

---

**Supplementary material:** The online version of this article offers supplementary material <https://doi.org/10.1515/nanoph-2020-0034>.

# Plasmon induced brightening of dark exciton in monolayer WSe<sub>2</sub> for quantum optoelectronics

Cite as: Appl. Phys. Lett. 114, 201101 (2019); <https://doi.org/10.1063/1.5093664>

Submitted: 23 February 2019 . Accepted: 28 April 2019 . Published Online: 21 May 2019

Ankit Arora , Tejendra Dixit, K. V. Anil Kumar, Sivarama Krishnan, K. Lakshmi Ganapathi, Ananth Krishnan , Pramoda K. Nayak , and M. S. Ramachandra Rao



View Online



Export Citation



CrossMark

## ARTICLES YOU MAY BE INTERESTED IN

[Investigation of the band alignment at MoS<sub>2</sub>/PtSe<sub>2</sub> heterojunctions](#)

Applied Physics Letters 114, 201601 (2019); <https://doi.org/10.1063/1.5097248>

[Negative refraction inspired polariton lens in van der Waals lateral heterojunctions](#)

Applied Physics Letters 114, 221101 (2019); <https://doi.org/10.1063/1.5098346>

[Observation of Kerr nonlinearity and Kerr-like nonlinearity induced by terahertz generation in LiNbO<sub>3</sub>](#)

Applied Physics Letters 114, 201102 (2019); <https://doi.org/10.1063/1.5096557>



[WWW.MMR-TECH.COM](http://WWW.MMR-TECH.COM)

THE WORLD'S RESOURCE FOR  
VARIABLE TEMPERATURE  
SOLID STATE CHARACTERIZATION



OPTICAL STUDIES SYSTEMS



SEEBECK STUDIES SYSTEMS



MICROPROBE STATIONS



HALL EFFECT STUDY SYSTEMS AND MAGNETS

# Plasmon induced brightening of dark exciton in monolayer WSe<sub>2</sub> for quantum optoelectronics

Cite as: Appl. Phys. Lett. 114, 201101 (2019); doi: 10.1063/1.5093664

Submitted: 23 February 2019 · Accepted: 28 April 2019 ·

Published Online: 21 May 2019



View Online



Export Citation



CrossMark

Ankit Arora,<sup>1,2,3</sup> Tejendra Dixit,<sup>1,3</sup> K. V. Anil Kumar,<sup>1</sup> Sivarama Krishnan,<sup>1</sup> K. Lakshmi Ganapathi,<sup>1</sup> Ananth Krishnan,<sup>2,a)</sup> Pramoda K. Nayak,<sup>1,b)</sup> and M. S. Ramachandra Rao<sup>1,3,c)</sup>

## AFFILIATIONS

<sup>1</sup>Department of Physics and Materials Science Research Centre, Indian Institute of Technology Madras, Chennai 600036, India

<sup>2</sup>Centre for NEMS and Nano Photonics (CNNP), Department of Electrical Engineering, Indian Institute of Technology Madras, Chennai 600036, India

<sup>3</sup>Nano Functional Materials Technology Centre, Indian Institute of Technology Madras, Chennai 600036, India

a) Electronic mail: [ananthk@iitm.ac.in](mailto:ananthk@iitm.ac.in)

b) Electronic mail: [pnayak@iitm.ac.in](mailto:pnayak@iitm.ac.in)

c) Electronic mail: [msrro@iitm.ac.in](mailto:msrro@iitm.ac.in)

## ABSTRACT

In the present work, we report plasmon induced brightening of dark excitons ( $X_D$ ) in Au nanoparticle (Au-NP) coated monolayer (1L) WSe<sub>2</sub>. We observed one order enhancement in photoluminescence (PL) intensity and surface enhanced Raman scattering in Au-NP/1L-WSe<sub>2</sub> at room temperature (RT). Temperature dependent PL measurements showed enhanced PL emission from RT down to 100 K in contrast to reduced PL emission which is generally observed for pristine 1L-WSe<sub>2</sub>. We attribute this effect to the out-of-plane electric field induced by the scattering from Au-NPs, which results in the out-of-plane dipole moment and spin-flip of conduction band electrons in Au-NP/1L-WSe<sub>2</sub>, making  $X_D$  bright. Our approach provides a facile way to harness excitonic properties in low-dimensional semiconductors, offering simple strategies for quantum optoelectronics.

Published under license by AIP Publishing. <https://doi.org/10.1063/1.5093664>

Monolayer transition metal dichalcogenides (1L-TMDs), with chemical formula MX<sub>2</sub> (M = Mo, W, and so on; X = S, Se, or Te) are semiconductors with a direct bandgap situated at the K-point of the Brillouin zone.<sup>1,2</sup> These two-dimensional (2D) systems exhibit tightly bound electron-hole pairs called excitons even at room temperature (RT) and therefore have great potential for several photonic applications.<sup>3–5</sup> However, their low quantum efficiency, weak optical absorption, and low photoluminescence (PL) hinder their practical utilization. In the recent past, several methods have been demonstrated to enhance the PL significantly by integrating plasmonic nanostructures with 1L-TMDs.<sup>6–14</sup> The exciton-plasmon interaction in such structures has been discussed in terms of strong near-field enhancement, resonance overlap, and/or charge transfer between plasmonic nanostructures and 1L-TMDs. Surprisingly, the PL enhancement is not unanimous as there are studies reporting both PL enhancement<sup>6,8</sup> and PL quenching<sup>15</sup> in similar systems. The consequence of this process is still under debate and probably needs more comprehensive study of metal/1L-TMD hybrid structures considering other intriguing properties of TMDs.

Due to the absence of inversion symmetry and the presence of strong spin-orbit interaction (SOI), 1L-TMDs show energy bands that exhibit spin splitting with opposite signs in the two valleys<sup>16</sup> as shown in Fig. 1. The magnitude of valence band splitting ( $\Delta_{VB}$ ) is in the range of few hundred millielectron volts, giving rise to two excitonic energy levels labeled as A and B. The conduction band splitting ( $\Delta_{CB}$ ) is in the range of tens of meV, and the spin orientation at the two levels is material dependent.<sup>17–19</sup> Depending on the spin configuration of the electron-hole pair, excitons in 1L-TMD can be either optically bright or dark.<sup>20–22</sup> An exciton is optically bright when it consists of an electron and a hole with opposite spins that exist in the same valley and optically dark otherwise. In the case of 1L-WX<sub>2</sub>, the upper valence band and the lowest conduction band have the same spin in a valley, hence making the lowest intravalley transition optically dark. For MoX<sub>2</sub>, the splitting is opposite to that of WX<sub>2</sub>, i.e., the lowest intravalley transition is optically bright. Dark excitons ( $X_D$ ) exhibit a much longer radiative lifetime compared to bright excitons ( $X_O$ ), which makes them attractive for optically controlled information processing.<sup>23–25</sup> However, optical excitation, detection, and control of  $X_D$

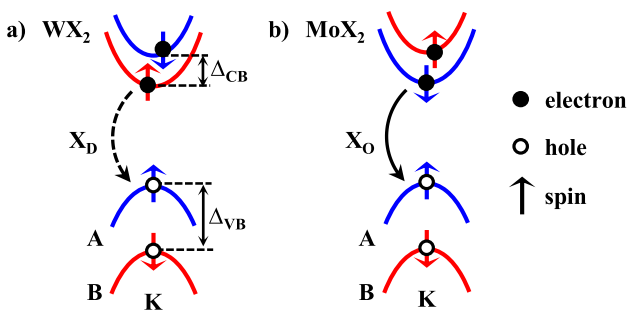


**FIG. 1.** E-k diagram of (a)  $\text{WX}_2$  and (b)  $\text{MoX}_2$  at the K valley, showing valence band splitting ( $\Delta_{VB}$ ) and conduction band splitting ( $\Delta_{CB}$ ) with the spin orientation.  $X_D$  and  $X_O$  correspond to the optically dark and bright transitions, respectively.

have remained challenging due to their decoupled nature from light.<sup>22,24</sup> Recently, several approaches to couple  $X_D$  with light have been demonstrated by applying either high in-plane magnetic fields<sup>25</sup> or out-of-plane electric fields via near-field coupling to surface plasmon polaritons.<sup>24</sup> In addition to this, Park *et al.* have proposed another method using tip enhanced PL spectroscopy, where a metal nanotip couples to the out-of-plane dipole moment of  $X_D$ , making it bright.<sup>26</sup> These methods are, however, restricted due to the need for cryogenic temperature ( $\sim 4\text{ K}$ ), exceptionally high magnetic field ( $\sim 30\text{ T}$ ), and/or system complexity.

In the present work, we study the exciton-plasmon interaction experimentally by drop-casting Au nanoparticles (Au-NPs) on chemical vapor deposition (CVD) grown 1L-WSe<sub>2</sub>. Temperature dependent PL measurements of these structures showed a gradual increase in PL intensity at reduced temperatures, in contrast to the reduced PL emission observed for pristine 1L-WSe<sub>2</sub>.<sup>27</sup> We attribute this reversed temperature trend of PL intensity in Au-NP/1L-WSe<sub>2</sub> to the brightening of dark excitons. Furthermore, electromagnetic simulations of Au-NP/1L-WSe<sub>2</sub> were carried out to understand this effect. It was observed that some of the scattered components of incident light can give rise to the out-of-plane electric field, which, on the surface of a material with strong SOI, can couple to  $X_D$ , thereby making them bright. This method provides a facile way to optically probe  $X_D$  and manipulate excitonic properties of atomically thin materials, thus opening up new avenues for realizing active metasurfaces and robust quantum optoelectronic systems.

The 1L-WSe<sub>2</sub> flakes were grown on the sapphire substrate using low pressure CVD as mentioned in our earlier report.<sup>28</sup> Colloidal solution of Au-NPs with a mean diameter of  $\sim 45\text{ nm}$  and the extinction peak at  $\sim 2.3\text{ eV}$  was prepared using the standard citrate reduction method<sup>29</sup> (shown in Fig. S1, *supplementary material*). Spherical Au-NPs of this size ( $\sim 50\text{ nm}$ ) were selected in order to have a polarization independent response and a sufficiently high extinction cross-section with a narrow resonance spectrum away from 1L-WSe<sub>2</sub> transition. The synthesized Au-NP solution was drop-cast on as-grown 1L-WSe<sub>2</sub> and dried at 330 K on a hot plate. The atomic force microscopy measurements using a Park Systems NX10 were carried out to determine the flake thickness and Au-NP distribution on 1L-WSe<sub>2</sub> as shown in Fig. S2. PL and the Raman spectroscopy measurements were performed using a HORIBA LabRAM in a confocal microscopy backscattering geometry. Continuous wave (CW) lasers of

energies 1.96 eV and 2.54 eV and optical power  $\sim 700\text{ }\mu\text{W}$  were used as excitation sources. The spot size of these laser beams was  $\sim 1\text{ }\mu\text{m}$ . For RT measurements, a  $100\times$  objective was used, whereas a  $50\times$  long working distance objective was used for low temperature measurements down to 100 K.

Figure 2(a) shows the RT-PL spectra of 1L-WSe<sub>2</sub> without and with Au-NPs recorded using an excitation energy of 1.96 eV ( $E_{ex}$ ), which is much below the localized surface plasmon resonance (LSPR) energy of Au-NPs (2.3 eV). This  $E_{ex}$  was selected to avoid any hot-carrier effect or charge transfer between WSe<sub>2</sub> and Au-NPs and to ensure only the near-field enhancement. The PL peak for pristine 1L-WSe<sub>2</sub>/sapphire was observed at  $\sim 1.6\text{ eV}$ , which is slightly less than that of 1L-WSe<sub>2</sub>/SiO<sub>2</sub>.<sup>30</sup> The PL intensity of Au-NP/1L-WSe<sub>2</sub> was enhanced by an order of magnitude and was blue shifted by  $\sim 20\text{ meV}$  as compared to pristine 1L-WSe<sub>2</sub>. Since both the excitation and emission energies are far from LSPR, both are expected to be enhanced equally, resulting in overall PL intensity enhancement. The slight blue shift in the peak may be attributed to the change in dipole coupling strength in the vicinity of the enhanced electric field. Figure 2(b) shows the RT Raman spectra of 1L-WSe<sub>2</sub> without and with Au-NPs using  $E_{ex} = 1.96\text{ eV}$ . Because of the quasi-resonant condition, modes other than the dominant ones were also observed. The Raman spectrum of Au-NP/1L-WSe<sub>2</sub> showed surface enhanced Raman scattering (SERS) due to the near field enhancement. Since there is no alteration in the dominant modes of 1L-WSe<sub>2</sub> [shown in Fig. 2(b)], Au-NPs are expected to be adsorbed physically, indicating no bond formation between 1L-WSe<sub>2</sub> and Au-NPs. The peak at  $\sim 250\text{ cm}^{-1}$  can be attributed to degenerate  $E'$  and  $A'_1$  modes and at  $\sim 260\text{ cm}^{-1}$  to the second

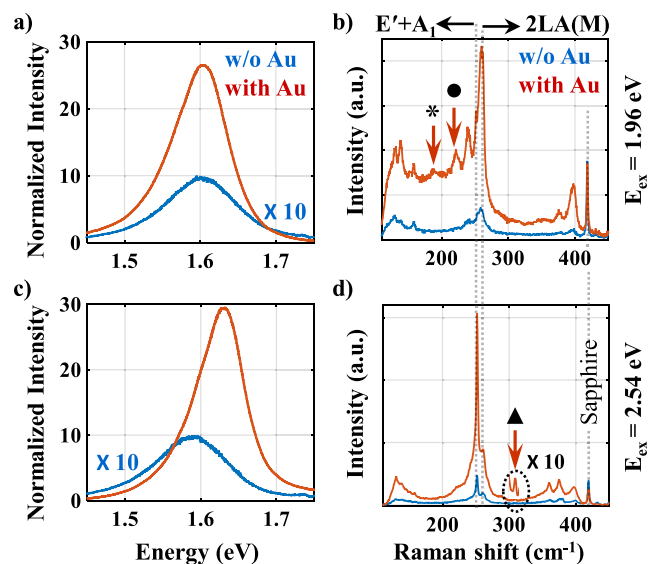


**FIG. 2.** Room temperature (a) and (c) PL and (b) and (d) Raman spectra of 1L-WSe<sub>2</sub> without (blue) and with (red) Au-NPs using 1.96 eV (a) and (b) and 2.54 eV (c) and (d) excitation. For clarity, PL spectra of WSe<sub>2</sub> without Au-NPs are multiplied by a factor of 10. The dominant characteristic Raman modes of 1L-WSe<sub>2</sub> [ $E' + A'_1$  and  $2\text{LA(M)}$ ] and the Raman mode of Sapphire are marked with vertical dashed lines. The new emergent peaks are indicated by arrows and marked as \* at  $\sim 180\text{ cm}^{-1}$  and ● at  $\sim 221\text{ cm}^{-1}$  in (b) and ▲ at  $\sim 308\text{ cm}^{-1}$  magnified by a factor of 10 in (d).

order 2LA(M) mode. Other peaks present at  $\sim 131\text{ cm}^{-1}$ ,  $139\text{ cm}^{-1}$ ,  $157\text{ cm}^{-1}$ ,  $239\text{ cm}^{-1}$ ,  $375\text{ cm}^{-1}$ , and  $397\text{ cm}^{-1}$  correspond to the higher order and combination modes.<sup>31,32</sup> It can be observed that the intensity of the sapphire peak at  $\sim 418\text{ cm}^{-1}$  remained unaltered as the maximum field enhancement is on the surface of 1L-WSe<sub>2</sub>. In the Raman spectrum of Au-NP/1L-WSe<sub>2</sub>, two new peaks marked as \* at  $\sim 180\text{ cm}^{-1}$  and • at  $\sim 221\text{ cm}^{-1}$  in Fig. 2(b) were observed, which were inactive in pristine 1L-WSe<sub>2</sub>. The peak at  $\sim 221\text{ cm}^{-1}$  corresponds to the combination of LA(M), TA(M), and ZA(M) modes, while the peak at  $\sim 180\text{ cm}^{-1}$  can be attributed to the E'' mode, which is expected at  $\sim 170\text{ cm}^{-1}$  theoretically.<sup>33,34</sup> Interestingly, the E'' mode is forbidden in backscattering experimental geometry,<sup>33</sup> where the light propagation direction is along the c-axis of 1L-WSe<sub>2</sub>. It can be expected that due to the enhanced photon scattering by Au-NPs, the E'' mode became active.

The RT PL and Raman spectra of 1L-WSe<sub>2</sub> without and with Au-NPs were also recorded using  $E_{ex} = 2.54\text{ eV}$  as shown in Figs. 2(c) and 2(d). Since  $E_{ex}$  is higher than LSPR of Au-NPs, it can facilitate charge transfer between WSe<sub>2</sub> and Au-NPs. Also, due to the large overlap between  $E_{ex}$  and LSPR, it is expected that the field enhancement of excitation intensity should be more than the emission intensity. However, it was observed that the enhancement in the PL intensity was nearly the same as that with  $E_{ex} = 1.96\text{ eV}$  with a small blue shift ( $\sim 30\text{ meV}$ ). This blue shift may be due to the charge transfer from Au-NPs to 1L-WSe<sub>2</sub>, as WSe<sub>2</sub> is intrinsically p-type in nature.<sup>35,36</sup> The Raman spectrum of Au-NP/1L-WSe<sub>2</sub> showed the emergence of a weak peak at  $\sim 308\text{ cm}^{-1}$  marked as ▲, which may be due to the strong phononic coupling between Au-NPs and 1L-WSe<sub>2</sub>.<sup>37</sup> For comparison, similar studies were carried out on CVD grown 1L-MoS<sub>2</sub>/SiO<sub>2</sub> as shown in Fig. S3. The RT-PL intensity was found to be almost double as compared to pristine MoS<sub>2</sub> for both  $1.96\text{ eV}$  and  $2.54\text{ eV}$  excitation.

In order to further explore the effect of Au-NPs on the excitonic properties of 1L-WSe<sub>2</sub>, temperature dependent PL measurements were carried out. Figure 3(a) shows the temperature dependent PL spectra of as-grown pristine 1L-WSe<sub>2</sub> in the range of RT to 100 K using  $E_{ex} = 1.96\text{ eV}$ . It was observed that there is a gradual reduction in the PL intensity with the reduction in temperature. This decrease in the PL intensity was due to the fact that the lowest transition in 1L-WSe<sub>2</sub> is optically dark.<sup>27</sup> As discussed above, the lowest energy A exciton in the case of 1L-WSe<sub>2</sub> can be either a spin-forbidden intervalley exciton or a momentum-forbidden intervalley exciton. At RT, due to sufficient thermal energy, there exists some population in the upper

conduction band of 1L-WSe<sub>2</sub>, resulting in an optically bright A exciton which dominates the RT PL. As the temperature decreases, the exciton population at the upper conduction band decreases and the lowest state increases, resulting in PL quenching. The blue shift in the PL with the reduction in temperature was also observed, which can be attributed to the reduction in the phonon scattering. For comparison, temperature dependent PL was also carried out for CVD grown 1L-MoS<sub>2</sub>, where PL intensity was observed to increase with the reduction in temperature because the lowest state is optically bright.<sup>1,20</sup> Therefore, the temperature dependences of the PL intensity of 1L-WSe<sub>2</sub> and 1L-MoS<sub>2</sub> are in clear contrast to each other, demonstrating the existence of the dark exciton in the former, while the bright exciton in the latter (the PL trend shown later in Fig. 4).

Figure 3(b) shows the temperature dependent PL spectra of Au-NP/1L-WSe<sub>2</sub>, and it was observed that there is an increase in the PL intensity with the reduction in temperature, which was opposite to the temperature dependence of pristine 1L-WSe<sub>2</sub>. The blue shift with the reduction in temperature was the same as that of pristine 1L-WSe<sub>2</sub> (Fig. S4). These measurements were repeated several times for different flakes and were found to exhibit the same trend. Some asymmetry in the PL line shape was observed for low temperatures similar to that reported by Yan *et al.*<sup>38</sup>

Figure 4(a) shows the temperature vs PL intensity of 1L-WSe<sub>2</sub> without and with Au-NPs. The PL intensity at different temperatures has been normalized with respect to that of RT. The horizontal dashed line corresponds to the PL intensity at RT. It is clearly evident that the PL intensity for pristine 1L-WSe<sub>2</sub> lies below the dashed line for all temperatures, while that of the Au-NP/1L-WSe<sub>2</sub> lies above it. The PL intensity of Au-NP/1L-WSe<sub>2</sub> at 100 K was observed to be  $\sim 3$  times more than that at RT. Figure 4(b) shows the temperature vs PL intensity of MoS<sub>2</sub> without and with Au-NPs, where the temperature dependence of intensity remained unaltered, indicating the diversified effect of Au-NP interaction with WSe<sub>2</sub> and MoS<sub>2</sub>.

The effect of Au-NPs, plasmon-exciton interaction, and the field experienced by the exciton is known to remain almost constant over the investigated temperature range.<sup>39</sup> The possible reasons for the reversed trend of the PL intensity vs temperature for Au-NP/1L-WSe<sub>2</sub> include: (i) luminescence from localized/defect states; (ii) emission from intervalley indirect transition; and (iii) perturbation in lowest dark state transition. Localized states originate due to the disorder or defect in the material because of impurity, stress, and/or substrate

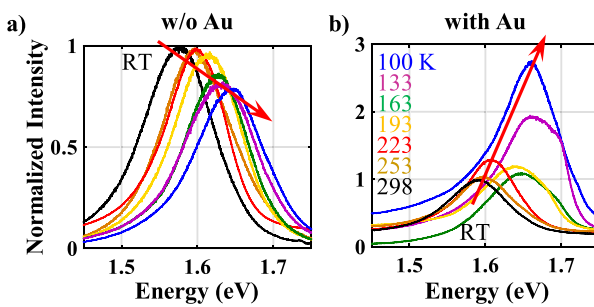


FIG. 3. Temperature dependent PL spectra of 1L-WSe<sub>2</sub> (a) without and (b) with Au-NPs using  $1.96\text{ eV}$  excitation. The direction of the red arrow indicates the reduction in temperature from RT to 100 K. In both the cases, the intensity was normalized with respect to the RT intensity.

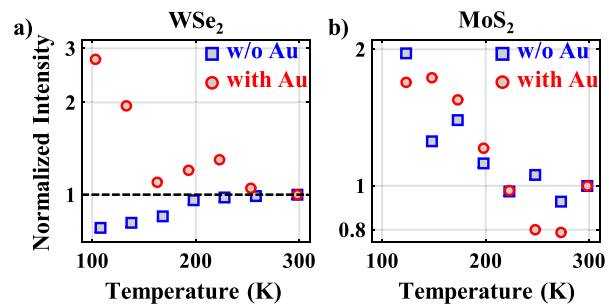
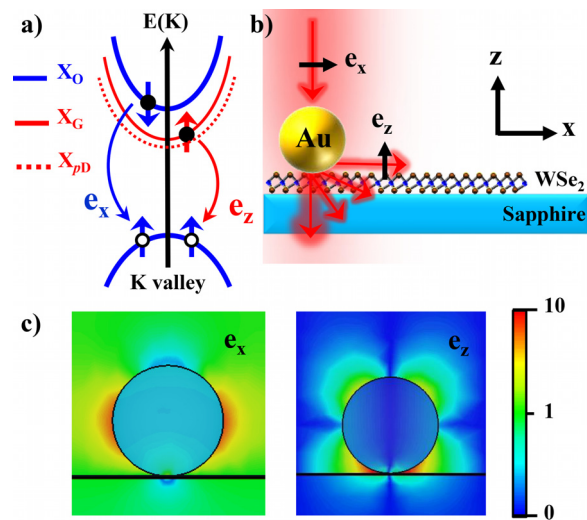


FIG. 4. (a) Temperature vs PL intensity of 1L-WSe<sub>2</sub> without (blue square) and with (red circle) Au-NPs using  $1.96\text{ eV}$  excitation; (b) temperature vs PL intensity of MoS<sub>2</sub> without (blue square) and with (red circle) Au-NPs using  $2.54\text{ eV}$  excitation. In both the cases, the intensity was normalized with respect to the RT intensity.

roughness.<sup>40</sup> Emission from these states may also be significantly affected by Au-NPs coated on the flakes.<sup>11</sup> Emission from these states increases with the decrease in temperature and occurs at much lower energy than that of the free exciton. However, localized state emissions are observed at temperatures as low as few tens of Kelvins and become insignificant above 100 K.<sup>11,38,40</sup> In the present experiments, an increase in the intensity was observed for all the temperatures below RT with a consistent blue shift and no emergence of new low energy peaks. Therefore, the contribution from localized states to the reversed temperature trend can be ruled out. Second, the intervalley excitons are momentum-forbidden and need phonon interaction to become optically active. Since the phonon population decreases with the decrease in temperature, the possibility of intervalley excitons can also be eliminated.

Therefore, the only possible reason for this reversed trend can be due to the perturbation in the lowest optically dark-state transition. As discussed previously, there exists conduction band spin splitting in 1L-WSe<sub>2</sub>, which gives rise to the intravalley optically dark state which has recently been shown to consist of two distinct states.<sup>41</sup> Because of the short range electron-hole exchange interaction, the degeneracy of this dark state is lifted. The lower state is spin-forbidden and electric dipole forbidden, known as the perfectly Dark exciton ( $X_{pD}$ ), and the upper state is spin-forbidden but electric-dipole allowed (out-of-plane of the 1L), known as the Gray exciton ( $X_G$ ). These dark states can be made optically bright with the use of the in-plane magnetic field, out-of-plane electric field, and/or reflection symmetry breaking.<sup>42</sup>

In the present work, all the PL measurements were carried out in backscattering geometry, where neither the external in-plane magnetic field nor the out-of-plane electric field was used. However, the Au-NPs have a large scattering cross-section<sup>43,44</sup> and can scatter the incident light to a wide range of angles, some of which would be along the plane of 1L-WSe<sub>2</sub> with an out-of-plane electric field component [schematic shown in Fig. 5(a)]. To verify this, single nanoparticle electromagnetic simulation was carried out using CST-Microwave Studio, a commercial electromagnetic solver<sup>45</sup> (the details are given in Sec. S5). Figure 5(c) shows the simulated time averaged  $e_x$  and  $e_z$  components of the electric field at 1.96 eV. It was observed that, for the x-polarized excitation, the scattered electric field has both the x and z components. In fact, the  $e_z$  component was well confined between the Au-NP and 1L-WSe<sub>2</sub> with strength more than that of  $e_x$  in the vicinity of Au-NP. This out-of-plane  $e_z$  component can be responsible for the brightening of both the components ( $X_G$ ,  $X_{pD}$ ) of dark excitons. The  $X_G$  exciton interacts with  $e_z$  via the out-of-plane electric dipole moment and becomes optically bright. Recently, it has been experimentally demonstrated that  $X_G$  can be excited/detected optically using either in-plane illumination or a high numerical aperture objective lens.<sup>46</sup> Moreover, the  $e_z$  component breaks the reflection symmetry of 1L-WSe<sub>2</sub>. This reflection symmetry breaking along with the strong spin-orbit interaction in 1L-WSe<sub>2</sub> can lead to the spin flip and hence make  $X_{pD}$  bright.<sup>42,47,48</sup> Therefore, Au-NPs in the vicinity of 1L-WSe<sub>2</sub> give rise to the out-of-plane electric field due to the wide angle scattering of the incident light, which was also evident from the emergence of new peaks in the Raman Spectrum of Au-NP/1L-WSe<sub>2</sub>, shown in Fig. 2(b). The PL spectrum of Au-NP/1L-WSe<sub>2</sub> at 100 K was further analyzed by deconvolving into the constituent Gaussian peaks (shown in Fig. S5). The two curves with peaks at 1.71 eV and 1.66 eV can be attributed to  $X_O$  and  $X_D$  respectively, with the peak separation of ~45 meV.<sup>17–19</sup>



**FIG. 5.** Brightening of the Dark exciton: (a) E-k diagram of 1L-WSe<sub>2</sub> at the K valley, showing conduction band splitting into bright (blue) and dark (red) exciton levels. Furthermore, the fine structure splitting of the dark exciton into lower spin-flip allowed ( $X_{pD}$ ) and upper z-dipolar allowed ( $X_G$ ) is also shown. For clarity, electrons and holes are shown off the central axis and only the A-exciton level is shown in the valence band. (b) Schematic of Au-NP/1L-WSe<sub>2</sub> on Sapphire, showing the wide angle scattering of the x-polarized incident light ( $e_x$ ), resulting in light along the plane of 1L-WSe<sub>2</sub> with the  $e_z$  component. (c) Simulated electric field plot showing the  $e_x$  and  $e_z$  component of electric field distribution on the x-z cross section. The color represents the normalized electric field intensity  $|e/e_0|$  on the log scale.

In conclusion, a reversed temperature trend of PL intensity was observed in Au-NP/1L-WSe<sub>2</sub> structures, which could be assigned to the brightening of  $X_D$ . Scattering from Au-NPs resulted in an out-of-plane electric field, which was supported by single NP electromagnetic simulation. The combined effect of this out-of-plane electric field and strong SOI in 1L-WSe<sub>2</sub> resulted in brightening of  $X_D$ . This work provides a simple approach for tuning excitonic properties of atomically thin materials, offering simple strategies for quantum optoelectronics. This work also indicates that the effect of plasmon-exciton interaction can have far-reaching consequences due to intriguing properties of materials and not just a result of field enhancement and charge transfer.

See the [supplementary material](#) for Au-NP characterization; AFM images of 1L-WSe<sub>2</sub>; PL spectra of MoS<sub>2</sub>; and deconvolved PL spectra of Au-NP/1L-WSe<sub>2</sub> showing  $X_D$ .

This work was partially supported by the Department of Science and Technology India (DST) that led to the establishment of the Nano Functional Materials Technology Centre (Grant No. SR/325 NM/NAT/02-2005). P.K.N. acknowledges the financial support from DST (Grant No. SERB/F/5379/2017-2018, Ramanujan Fellowship). K.L.G. acknowledges the financial support from DST (Grant No. DST/INSPIRE/04/2016/001865, INSPIRE Faculty program).

## REFERENCES

- K. F. Mak, C. Lee, J. Hone, J. Shan, and T. F. Heinz, *Phys. Rev. Lett.* **105**, 136805 (2010).

- <sup>2</sup>A. Splendiani, L. Sun, Y. Zhang, T. Li, J. Kim, C.-Y. Chim, G. Galli, and F. Wang, *Nano Lett.* **10**, 1271 (2010).
- <sup>3</sup>K. He, N. Kumar, L. Zhao, Z. Wang, K. F. Mak, H. Zhao, and J. Shan, *Phys. Rev. Lett.* **113**, 026803 (2014).
- <sup>4</sup>T. Mueller and E. Malic, *npj 2D Mater. Appl.* **2**, 29 (2018).
- <sup>5</sup>S. Z. Butler, S. M. Hollen, L. Cao, Y. Cui, J. A. Gupta, H. R. Gutierrez, T. F. Heinz, S. S. Hong, J. Huang, A. F. Ismach *et al.*, *ACS Nano* **7**, 2898 (2013).
- <sup>6</sup>Z. Wang, Z. Dong, Y. Gu, Y.-H. Chang, L. Zhang, L.-J. Li, W. Zhao, G. Eda, W. Zhang, G. Grinblat *et al.*, *Nat. Commun.* **7**, 11283 (2016).
- <sup>7</sup>F. Cheng, A. D. Johnson, Y. Tsai, P.-H. Su, S. Hu, J. G. Ekerdt, and C.-K. Shih, *ACS Photonics* **4**, 1421 (2017).
- <sup>8</sup>K. C. Lee, Y.-H. Chen, H.-Y. Lin, C.-C. Cheng, P.-Y. Chen, T.-Y. Wu, M.-H. Shih, K.-H. Wei, L.-J. Li, and C.-W. Chang, *Sci. Rep.* **5**, 16374 (2015).
- <sup>9</sup>S. Najmaei, A. Mlayah, A. Arbouet, C. Girard, J. Léotin, and J. Lou, *ACS Nano* **8**, 12682 (2014).
- <sup>10</sup>J. Kern, A. Trügler, I. Niehues, J. Ewering, R. Schmidt, R. Schneider, S. Najmaei, A. George, J. Zhang, J. Lou, U. Hohenester, S. M. de Vasconcellos, and R. Bratschitsch, *ACS Photonics* **2**(9), 1260–1265 (2015).
- <sup>11</sup>A. D. Johnson, F. Cheng, Y. Tsai, and C.-K. Shih, *Nano Lett.* **17**, 4317 (2017).
- <sup>12</sup>B. Mukherjee, N. Kaushik, R. P. Tripathi, A. Joseph, P. Mohapatra, S. Dhar, B. Singh, G. P. Kumar, E. Simsek, and S. Lodha, *Sci. Rep.* **7**, 41175 (2017).
- <sup>13</sup>J. Yan, C. Ma, P. Liu, and G. Yang, *ACS Photonics* **4**, 1092 (2017).
- <sup>14</sup>J. Sun, H. Hu, D. Zheng, D. Zhang, Q. Deng, S. Zhang, and H. Xu, *ACS Nano* **12**, 10393 (2018).
- <sup>15</sup>U. Bhanu, M. R. Islam, L. Tetard, and S. I. Khondaker, *Sci. Rep.* **4**, 5575 (2014).
- <sup>16</sup>Z. Zhu, Y. Cheng, and U. Schwingenschlögl, *Phys. Rev. B* **84**, 153402 (2011).
- <sup>17</sup>Z. Ye, T. Cao, K. O'brien, H. Zhu, X. Yin, Y. Wang, S. G. Louie, and X. Zhang, *Nature* **513**, 214 (2014).
- <sup>18</sup>A. Chernikov, T. C. Berkelbach, H. M. Hill, A. Rigosi, Y. Li, O. B. Aslan, D. R. Reichman, M. S. Hybertsen, and T. F. Heinz, *Phys. Rev. Lett.* **113**, 076802 (2014).
- <sup>19</sup>K. Kosmider, J. W. González, and J. Fernández-Rossier, *Phys. Rev. B* **88**, 245436 (2013).
- <sup>20</sup>D. Y. Qiu, H. Felipe, and S. G. Louie, *Phys. Rev. Lett.* **111**, 216805 (2013).
- <sup>21</sup>X. Xu, W. Yao, D. Xiao, and T. F. Heinz, *Nat. Phys.* **10**, 343 (2014).
- <sup>22</sup>J. Echeverry, B. Urbaszek, T. Amand, X. Marie, and I. Gerber, *Phys. Rev. B* **93**, 121107 (2016).
- <sup>23</sup>K. P. Loh, *Nat. Nanotechnol.* **12**, 837 (2017).
- <sup>24</sup>Y. Zhou, G. Scuri, D. S. Wild, A. A. High, A. Dibos, L. A. Jauregui, C. Shu, K. De Greve, K. Pistunova, A. Y. Joe *et al.*, *Nat. Nanotechnol.* **12**, 856 (2017).
- <sup>25</sup>X.-X. Zhang, T. Cao, Z. Lu, Y.-C. Lin, F. Zhang, Y. Wang, Z. Li, J. C. Hone, J. A. Robinson, D. Smirnov *et al.*, *Nat. Nanotechnol.* **12**, 883 (2017).
- <sup>26</sup>K.-D. Park, T. Jiang, G. Clark, X. Xu, and M. B. Raschke, *Nat. Nanotechnol.* **13**, 59 (2018).
- <sup>27</sup>X.-X. Zhang, Y. You, S. Y. F. Zhao, and T. F. Heinz, *Phys. Rev. Lett.* **115**, 257403 (2015).
- <sup>28</sup>P. K. Nayak, Y. Horbatenko, S. Ahn, G. Kim, J.-U. Lee, K. Y. Ma, A.-R. Jang, H. Lim, D. Kim, S. Ryu *et al.*, *ACS Nano* **11**, 4041 (2017).
- <sup>29</sup>J. Turkevich, P. C. Stevenson, and J. Hillier, *Discuss. Faraday Soc.* **11**, 55 (1951).
- <sup>30</sup>M. Dau, C. Vergnaud, A. Marty, F. Rortais, C. Beigné, H. Boukari, E. Bellet-Amalric, V. Guigoz, O. Renault, C. Alvarez *et al.*, *Appl. Phys. Lett.* **110**, 011909 (2017).
- <sup>31</sup>W. Zhao, Z. Ghorannevis, K. K. Amara, J. R. Pang, M. Toh, X. Zhang, C. Kloc, P. H. Tan, and G. Eda, *Nanoscale* **5**, 9677 (2013).
- <sup>32</sup>X. Zhang, X.-F. Qiao, W. Shi, J.-B. Wu, D.-S. Jiang, and P.-H. Tan, *Chem. Soc. Rev.* **44**, 2757 (2015).
- <sup>33</sup>H. Sahin, S. Tongay, S. Horzum, W. Fan, J. Zhou, J. Li, J. Wu, and F. Peeters, *Phys. Rev. B* **87**, 165409 (2013).
- <sup>34</sup>E. del Corro, A. Botello-Méndez, Y. Gillet, A. L. Elias, H. Terrones, S. Feng, C. Fantini, D. Rhodes, N. Pradhan, L. Balicas *et al.*, *Nano Lett.* **16**, 2363 (2016).
- <sup>35</sup>J. Kang, S. Tongay, J. Zhou, J. Li, and J. Wu, *Appl. Phys. Lett.* **102**, 012111 (2013).
- <sup>36</sup>H. Fang, S. Chuang, T. C. Chang, K. Takei, T. Takahashi, and A. Javey, *Nano Lett.* **12**, 3788 (2012).
- <sup>37</sup>M.-H. Chiu, M.-Y. Li, W. Zhang, W.-T. Hsu, W.-H. Chang, M. Terrones, H. Terrones, and L.-J. Li, *ACS Nano* **8**, 9649 (2014).
- <sup>38</sup>T. Yan, X. Qiao, X. Liu, P. Tan, and X. Zhang, *Appl. Phys. Lett.* **105**, 101901 (2014).
- <sup>39</sup>I. Abid, W. Chen, J. Yuan, A. Bohloul, S. Najmaei, C. Avendano, R. Pe?chou, A. Mlayah, and J. Lou, *ACS Photonics* **4**, 1653 (2017).
- <sup>40</sup>S. Zhang, C.-G. Wang, M.-Y. Li, D. Huang, L.-J. Li, W. Ji, and S. Wu, *Phys. Rev. Lett.* **119**, 046101 (2017).
- <sup>41</sup>C. Robert, T. Amand, F. Cadiz, D. Lagarde, E. Courtade, M. Manca, T. Taniguchi, K. Watanabe, B. Urbaszek, and X. Marie, *Phys. Rev. B* **96**, 155423 (2017).
- <sup>42</sup>A. Slobodeniuk and D. Basko, *2D Mater.* **3**, 035009 (2016).
- <sup>43</sup>C. F. Bohren and D. R. Huffman, *Absorption and Scattering of Light by Small Particles* (John Wiley & Sons, 2008).
- <sup>44</sup>U. Kreibig and M. Vollmer, *Optical Properties of Metal Clusters* (Springer Science & Business Media, 2013), Vol. 25.
- <sup>45</sup>M. Studio, <http://www.cst.com/products/cstmws> for Cst-computer simulation technology (2016).
- <sup>46</sup>G. Wang, C. Robert, M. Glazov, F. Cadiz, E. Courtade, T. Amand, D. Lagarde, T. Taniguchi, K. Watanabe, B. Urbaszek *et al.*, *Phys. Rev. Lett.* **119**, 047401 (2017).
- <sup>47</sup>E. I. Rashba, *Physica E* **20**, 189 (2004).
- <sup>48</sup>J. Ibañez-Azpíroz, A. Eiguren, E. Y. Sherman, and A. Bergara, *Phys. Rev. Lett.* **109**, 156401 (2012).

# Journal of Physics Communications



OPEN ACCESS

**PAPER**

## On-chip label-free plasmonic based imaging microscopy for microfluidics

RECEIVED  
24 May 2018REVISED  
18 July 2018ACCEPTED FOR PUBLICATION  
1 August 2018PUBLISHED  
13 August 2018P Arora<sup>1,2</sup> and A Krishnan<sup>1,2</sup><sup>1</sup> Centre for NEMS and Nanophotonics (CNNP), Department of Electrical Engineering, Indian Institute of Technology Madras, Chennai—600036, India<sup>2</sup> Experimental Optics Laboratory (Expo), Department of Electrical Engineering, Indian Institute of Technology Madras, Chennai—600036, IndiaE-mail: [ee11d036@ee.iitm.ac.in](mailto:ee11d036@ee.iitm.ac.in)**Keywords:** plasmonic microscopy, surface plasmon, microfluidic

Original content from this work may be used under the terms of the Creative Commons Attribution 3.0 licence.

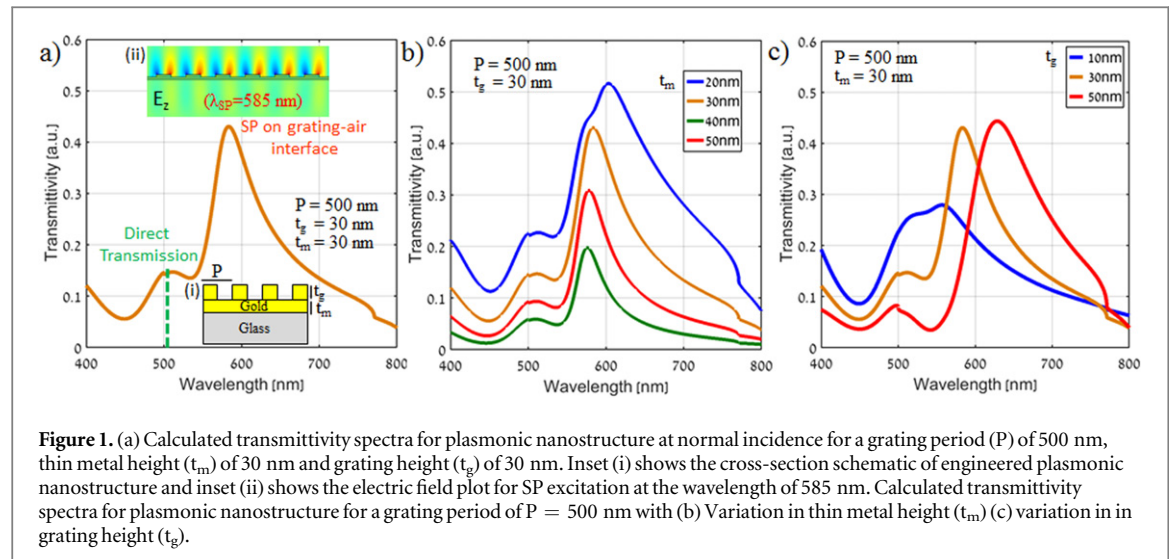
Any further distribution of this work must maintain attribution to the author(s) and the title of the work, journal citation and DOI.

**Abstract**

In this work, we demonstrated an on-chip label-free imaging microscopy using real and Fourier Plane (FP) dark field images of surface plasmons, by integrating engineered plasmonic substrates with different shapes of microfluidic channels. After successful integration of fabricated plasmonic nanostructures with SU-8 based microfluidic channels, on-chip label-free index monitoring of analytes with different refractive indices was demonstrated and an index resolution of  $1.63 \times 10^{-4}$  RIU was achieved by quantifying CMYK components of captured images. Label-free imaging for interface of colorless miscible and immiscible analytes flowing on plasmonic nanostructures in the microfluidic channels was performed using color-selective filtering nature of plasmonic nanostructures. Hydrodynamic focusing where the width of the focused stream of one liquid was controlled by the relative flow rates of the three liquids was demonstrated and utilized to capture the flow of air bubbles on plasmonic nanostructures with real and FP images. Since, the imaging is realized on a chip and does not need any complicated and bulky arrangement, it will benefit the development of flat optical components for sensing applications and will be well suited for on-chip point of care diagnostics.

**Introduction**

Traditional labels such as fluorophores or chromophores are widely used in microfluidic applications to visualize flow or detect the presence or concentration of relevant species [1–5]. However, each of these labels has shortcomings including bleaching of fluorophores and non-specificity of chromophores etc [6, 7]. In particular in microfluidics, labeling with multiple dyes may suffer from the low Reynolds number laminar flow and when introduced at high concentration, may alter the physical properties of the flow solution [8, 9]. To avoid this, label-free on-chip sensing has gained huge attention because of low sample consumption, avoiding time consuming labeling process and the efficient delivery of target analytes to sensing sites [10–14]. In particular, Surface Plasmon Resonance (SPR) based label-free optical technique has been integrated with microfluidics to measure the changes in the refractive index near the surface of the sensor with the advantage of simple collinear broadband illumination and portable spectrophotometer [15–20]. Moreover, periodic nanostructure coupled SPRs have been proven to be a promising tool in label free imaging due to the color-selective filtering nature and the possibility of coupling to Surface Plasmons (SP) modes at normal incidences [21–26]. In this work, we demonstrate an on-chip label free plasmonic based imaging microscopy for microfluidics on engineered periodic nanostructures operating in collinear transmission mode. The engineered fabricated 1D and 2D nanostructures after successful integration of SU-8 based microfluidic channels were placed in between two crossed polarizers ( $\theta_P = 45^\circ$  and  $\theta_A = 135^\circ$ ) to diminish direct 0th order transmission [27] and capture bright SPs emission against a dark background in real and Fourier Plane (FP) images. The analytes of interest with different refractive indices were introduced and the change in the color corresponding to SP excitation



wavelengths was captured in real and FP images and quantified with Cyan, Magenta, Yellow, and Black (CMYK) components of images extracted using image processing [28]. The interaction of two colorless miscible and immiscible liquid analytes were captured by real and FP images without using any stain (label) in SU-8 based microfluidic channels using color-selective filtering nature of plasmonic nanostructures. Hydrodynamic focusing which allows users of flow cytometry to gauge the size of particles in a flow channel [5] by controlling the width of the focused stream of one liquid by relative flow rates of other liquids, was utilized to capture the flow of air bubbles using real and FP images. The most common configuration for hydrodynamic focusing is a 3-inlets-1-outlet device which was fabricated and tested that allowed to capture the flow of air bubbles on plasmonic nanostructures through hydrodynamic focusing. Since the imaging is realized on a chip and does not need any complicated and bulky arrangement, it will be well suited for on-chip point of care diagnostics. Several of these proposed structures can be integrated on the same chip with plasmonic nanostructures of different sizes and shapes to realize multiplex, multianalyte sensing for several different target analytes.

### Design and fabrication of plasmonic on-chip device

The cross-section schematic of designed periodic plasmonic nanostructure with period  $\approx$  wavelength is shown in inset (i) of figure 1(a). Broadband simulations were performed for normal incidence from the top of the structures using Rigorous coupled wave analysis to exhibit transmission resonances as transmission peaks instead of dips in visible spectrum [29]. The choice of these geometrical parameters for low aspect ratio nanostructure structure was made from a number of simulations carried out with systematic variation of the geometrical parameters to achieve narrower Full Width at Half maximum (FWHM) and maximum transmittivity which corresponds to maximum excitation efficiency of SPs. The calculated transmission characteristics of the structure for a grating height ( $t_g$ ) of 30 nm, period ( $P$ ) of 500 nm with 50% duty cycle and for a homogeneous thin metal layer thickness  $t_m$  of 30 nm, are shown in figure 1(a). Two transmission peaks at wavelengths of 520 nm and 585 nm were observed in the spectra as shown in figure 1(a). The transmission peak at wavelength 520 nm was due to direct transmission through thin gold film since near this wavelength, refractive index of gold  $\approx 1$  because of strong inter-band transition in the near UV-vis region [27]. The field distribution for peak at 585 nm is shown in the inset of figure 1(a). From the field plot, it is clear that the peak at 585 nm was attributed to a SP mode at metal grating-air interface. Due to the presence of a homogeneous metal layer, under most conditions, almost all of the incident light was reflected back to the top. When the SPs were excited on the metal grating-air interface, due to very small thickness of the homogeneous metal layer ( $t_m = 30$  nm), a radiative decay of SPs occurred through the substrate (glass) and the light leaked through the substrate at specific angles depending on the refractive indices of substrate and air.

To get the optimized geometry for proposed plasmonic nanograting structure, the geometrical parameters namely the thin metal height ( $t_m$ ) and grating height ( $t_g$ ) were changed systematically as shown in figures 1(b) and (c) respectively. Figure 1(b) shows the transmittivity spectra for  $t_g$  of 30 nm,  $P$  of 500 nm and with different thickness of metal height ( $t_m$ ). As  $t_m$  was increased to 50 nm, the transmittivity reduced to 0.2 (green color) resulting in low signal contrast but with narrowest FWHM. When  $t_m$  was lower than 30 nm (blue color), the transmittivity value was found to be the highest but with higher FWHM. Hence, a careful choice of the thickness of the thin metal ( $t_m$ ) of 30 nm (brown color), resulted in a decent value of signal contrast and FWHM. Figure 1(c) shows the transmittivity spectra for  $t_m$  of 30 nm,  $P$  of 500 nm and with different thickness of metal

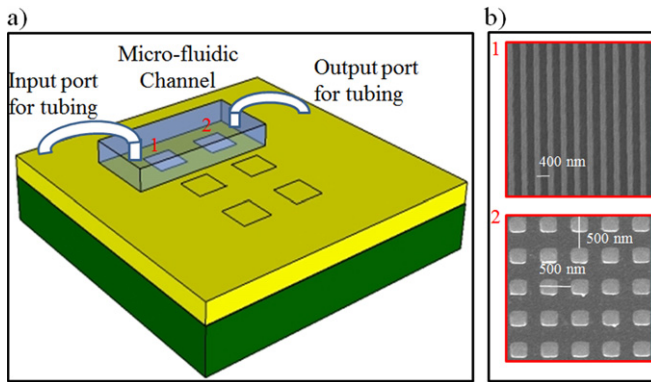


**Figure 2.** (a) The schematic for on-chip plasmonic device integrated with microfluidic channel (b) SEM micrograph for fabricated periodic plasmonic 1D and 2D nanostructure.

grating height ( $t_g$ ). It was noticed that the metal grating height ( $t_g$ ) of 30 nm (brown color) resulted in high transmittivity and low FWHM. The more information about the proposed designed structure can be found in [27, 29].

The engineered nanostructures were fabricated on glass substrate coated with a thin gold film of thickness 30 nm, using e-beam lithography, gold evaporation of thickness 30 nm and lift-off process [21, 27]. Inclusion of a homogeneous 30 nm metal layer below the periodic structures resulted in mitigating the charging effects during electron beam lithography. Finally, on-chip plasmonic device was fabricated by integrating the fabricated plasmonic substrates with microfluidic channels. Figure 2(a) shows the schematic of the on-chip device integrated with plasmonic substrate and figure 2(b) shows the SEM micrograph for fabricated 1D and 2D plasmonic nanostructures.

After fabricating the plasmonic substrates, SU-8 (10) resist from Microchem was spin coated on the surface of plasmonic substrates at the speed of 5000 rpm for 30 s to a thickness of 10  $\mu\text{m}$ . It was then soft baked at 80 °C for 20 min. The required channel mask designed in Clewin software and printed on transparency sheet, was used to expose the SU-8 layer using UV- photolithography. The alignment between fabricated plasmonic nanostructures and microfluidic channels was carried out using mask aligning process. The substrates were prebaked at 80 °C for 15 min and then patterns were developed in SU-8 developer for 1 min, followed by rinsing with DI water. Again the baking step was done by keeping the samples in oven at 80 °C temperature for 30 min. Now, the next step was to cap and seal the fabricated SU-8 microfluidic channels. A PDMS cap was used with holes for inlets and outlets corresponding to fabricated channels and aligned with SU-8 reservoirs. The property of epoxy group of SU-8 to form covalent bond with amine group was used to seal PDMS with SU-8 channels. The surface of PDMS was first functionalized with (–OH) groups through oxygen plasma for 30 s exposure and then was immersed in a solution of (3-AminoPropyl) Tri Ethoxy Silane (APTES) for 2 h and as a result of which, the amine groups were formed on the surface of PDMS by silanization [30]. Then the PDMS was capped and brought into contact with SU-8 channels and by applying the pressure gently and keeping the integrated device for 2 h in oven at temperature of 80 °C, the bonding was carried out. Figures 3(a)–(d) shows the complete procedure for fabricating SU-8 based microfluidic channels and sealing these channels with PDMS. Figure 3(e) shows the image of on-chip device with one inlet and one outlet and figure 3(f) shows the fabricated SU-8 channel. The idea of fabricating SU-8 based microfluidic channel and capping with PDMS, instead of fabricating conventional PDMS based microfluidic channel was to get rid of the precise alignment of the PDMS based microfluidic channels and the plasmonic nanostructures which is a very big challenge. Moreover, the bonding between plasma treated PDMS and gold surface was found to be very weak which results in leakage from the channels.

To test the bonding quality of these SU-8 based microfluidic channels, DI water was pumped through these channels at different flow rates (from 0.5  $\mu\text{l min}^{-1}$  to 30  $\mu\text{l min}^{-1}$ ) using a syringe pump and captured microscope images confirmed the flow of water without any leakage through the channel.

### Characterization setup

Figure 4 shows the characterization setup used for real-time monitoring of refractive index induced surface modifications for different analytes. A pair of cross polarizer-analyzer ( $\theta_P = 45^\circ$  and  $\theta_A = 135^\circ$ ) in an inverted broadband leakage radiation bright microscope is used to diminish direct 0th order transmission and capture bright SPs emission (due to  $\pm 1$  diffraction order) against a dark background. A polarization rotation of 90° in fabricated nanostructures mediated by SP excitation was used to develop a dark field plasmon polarization

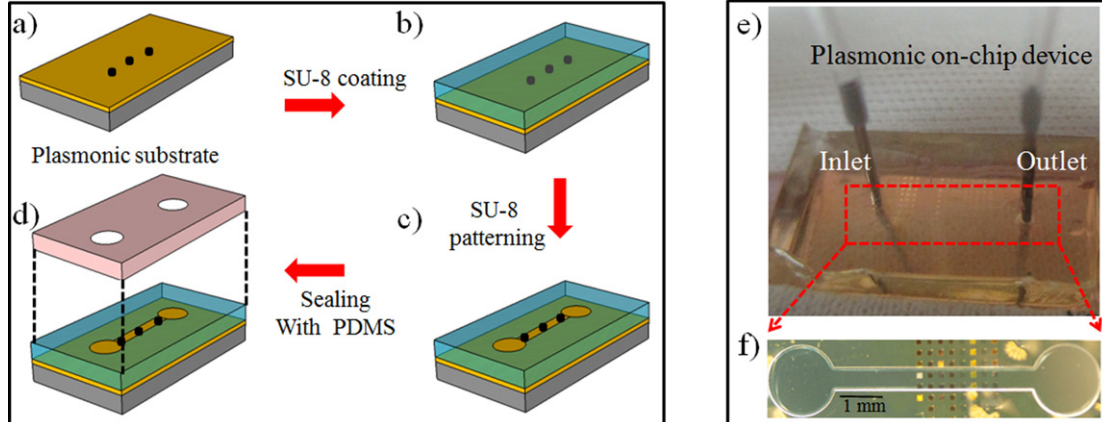


**Figure 3.** (a)–(d) The process flow for fabrication of SU-8 based microfluidic channel (e) On-chip device with one inlet and one outlet (f) Microscopic image of fabricated SU-8 channel.

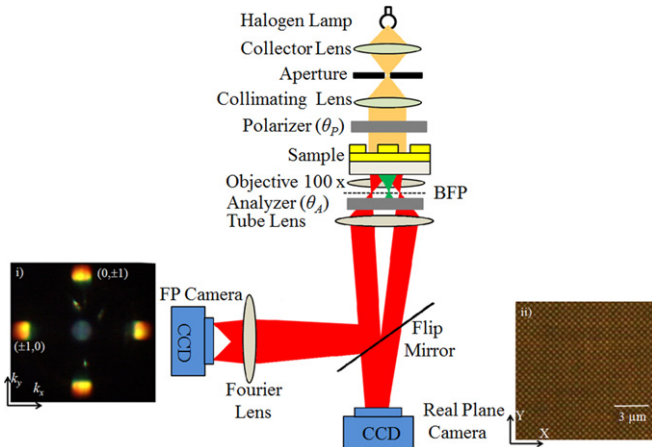


**Figure 4.** (a) Characterization setup. Inset (i) and (ii) shows the captured FP and real plane images for 2D plasmonic nanostructures of  $P_x = P_y = 500$  nm.

microscope using a conventional bright field microscope under two crossed axis polarizers [27]. Leakage of plasmon coupled transmitted radiation from the bottom of the substrate was collected by a  $100\times$  immersion oil objective lens. A flip mirror was used to divert the beam to a Fourier lens, and camera placed at its focus was used to obtain the FP images. Inset (i) and (ii) shows the FP and real plane images captured for 2D plasmonic nanostructures of period  $P_x = P_y = 500$  nm respectively. In real and FP images, the yellow brown color obtained due to the  $(0, \pm 1)$  and  $(\pm 1, 0)$  diffraction order coupled to SP mode at cross polarizer-analyzer position. The detailed mechanism for this phenomenon has been described in our recent work [27].

### Capturing refractive index induced surface modifications

The analytes were infused into the device using 2 ml, 1000 series gas tight syringes actuated by syringe pump to control the flow rate of the analytes passing through microfluidic channel. The experiments were carried out inside an air-conditioned lab at a steady temperature of  $25^\circ\text{C}$  to overcome the effect of temperature on the viscosity of different analytes [31]. The broadband white light source in an inverted microscope passing through a polarizer was incident on the device and the transmitted light was captured by real and FP CCD camera after passing through a cross axis analyzer.

The analytes of different refractive indices were introduced on the sensing sites through microfluidic channel having nanostructures with different periods. First the measurement was carried out with air and then the analyte with known refractive index was introduced. Finally the channel was washed with DI water and exposed to air to make sure that analyte was completely washed off the surface and the color returns to that air reference before introducing the next analyte.

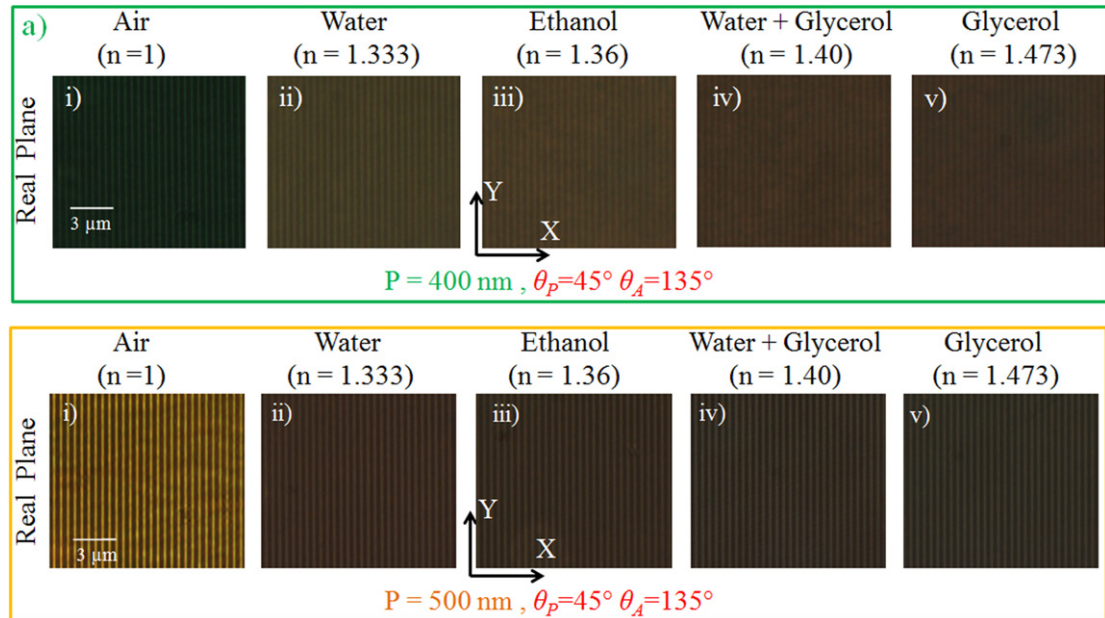


**Figure 5.** Real plane images of 1D plasmonic nanostructure with (a)  $P = 400 \text{ nm}$  (b)  $P = 500 \text{ nm}$  with analytes of different refractive indices.

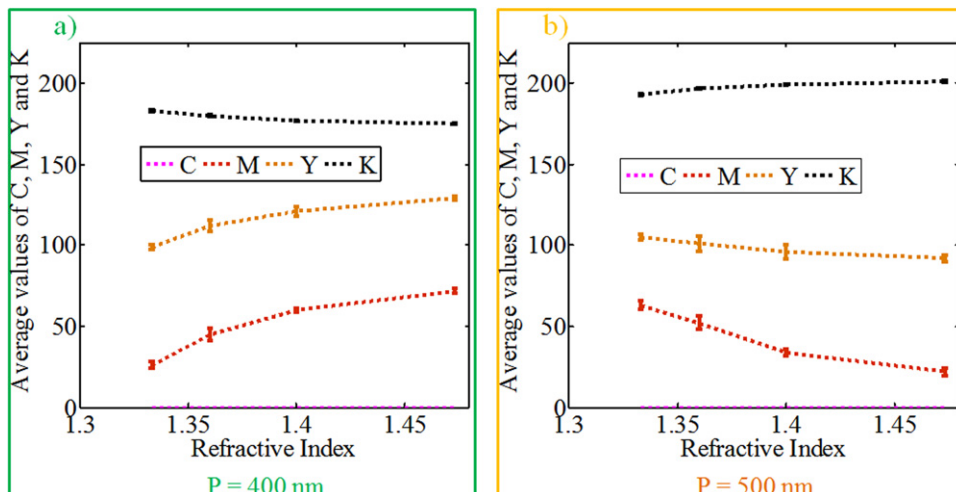
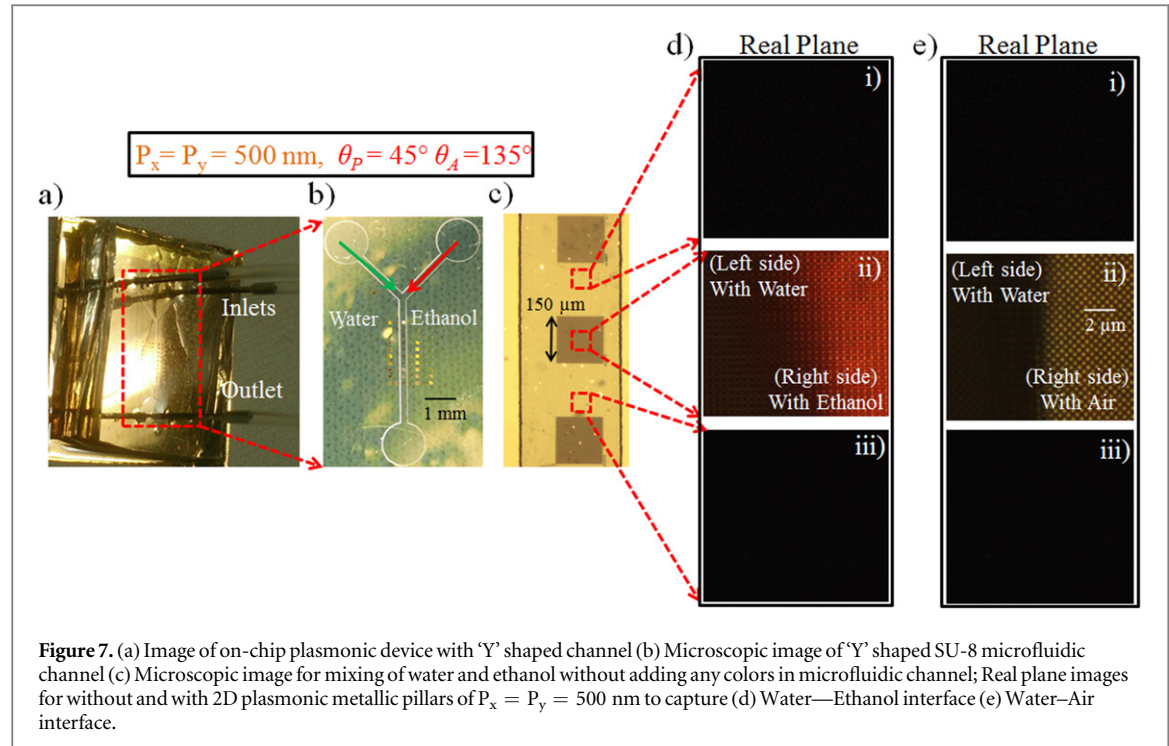


**Figure 6.** Average values of C, M, Y and K for captured images with varying refractive index of analytes for 1D plasmonic structure of (a)  $P = 400 \text{ nm}$  (b)  $P = 500 \text{ nm}$ .

Figure 5(a) shows the real plane images for 1D plasmonic nanostructure of  $P = 400 \text{ nm}$  with analytes of different refractive indices. The shift in color from green to orange-red was clearly observed with increase in refractive index in captured images. In the same channel, the images for different analytes (as introduced in figure 5(a)) for 1D plasmonic nanostructures of  $P = 500 \text{ nm}$  were also captured as shown in figure 5(b). The change in color with increase in refractive index can be clearly seen with analytes of different refractive indices with naked eyes. The change in color due to refractive index induced surface modification was quantified with CMYK components ( $\Delta C$ ,  $\Delta M$ ,  $\Delta Y$ ,  $\Delta K$ ) of captured images extracted using image processing as shown in figure 6. Using the standard deviation ( $\sigma_{CMYK} = 1.27$ ) value calculated from the repeatability measurements, the refractive index resolution can be defined as [21, 22, 32]

$$\text{Index Resolution} = \{\Delta n / (\Delta C^2 + \Delta M^2 + \Delta Y^2 + \Delta K^2)\} \times 2\sigma_{CMYK}$$

An index resolution of  $1.63 \times 10^{-4} \text{ RIU}$  was experimentally achieved from captured images. The reason behind choosing the CMYK (Cyan, Magenta, Yellow, Black) components instead of RGB (Red, Green, Blue) components to evaluate the sensing performance was to increase the range of measurement. Due to the presence



of 4 planes namely (C, M, Y, K) each ranging from 0 to 255, instead of R, G, B, the range of measurement can be improved considerably.

#### Label free imaging of miscible and immiscible analytes

The performance of on-chip plasmonic device with a 'Y' shaped microfluidic channel integrated with plasmonic substrates was investigated by mixing of two colorless liquids. First, the analysis was started with two miscible liquids and then for immiscible liquids. Figure 7(a) shows the image of on-chip plasmonic device with 'Y' shaped microfluidic channel and figure 7(b) shows the 'Y' shaped SU-8 microfluidic channel. The water and ethanol were taken as two miscible liquids to capture the interface of water and ethanol. The water was passed through the left inlet and the ethanol was passed through the right inlet. Figure 7(c) shows the mixing of water and ethanol without adding any colors where the interface of water and ethanol could not be distinguished.

So here, the color-selective filtering nature of plasmonic nanostructures was used for observing the interface of two colorless miscible liquids while flowing in 'Y' shaped channel. The real plane images were captured for the liquids flowing in the channel on the locations with and without plasmonic nanostructures. Figure 7(d-ii) shows the captured real plane image for 2D plasmonic nanostructure with metallic pillars of  $P_x = P_y = 500$  nm. The difference in color for water and ethanol was clearly seen due to different refractive indices in captured real plane image, whereas, the images captured on the locations without plasmonic nanostructures were found completely dark as expected. An another experiment was also performed to compare our results with reference by changing the right inlet analyte (ethanol) to air and captured the water-air interface on 2D metallic pillars of  $P_x = P_y = 500$  nm as shown in figure 7(e-ii). Thus, the color-selective filtering nature of plasmonic nanostructures can be used for capturing the interface of two colorless miscible liquids without any stain (label).

After capturing the interface of two colorless miscible liquids, the mixing of two immiscible liquids was studied. Here, the water and TCE (Tri Chloro Ethylene) were taken as two immiscible liquids. While mixing of Water and TCE, TCE droplets were formed, which were captured in real and FP images for 1D plasmonic nanostructures of  $P = 500$  nm. Figures 8(b) and (c) show the microscopic images for mixing of two colorless immiscible liquids, without TCE droplet and with TCE droplet respectively. Figures 8(d) and (e) show the FP and real plane images for capturing water and TCE. Whenever TCE droplet passed through the sensing sites, the change in color was clearly observed in FP and real plane images as shown in figures 8(c) and (d). In FP images, the change in color for  $\pm 1$  diffraction order coupled to SP mode was observed from dark red to orange due to change in the index of water and TCE. Since the FP images allow to image the directional emission in the reciprocal space, the images actually represent the momentum or effective index information directly. The change in the refractive index of the analyte modifies the dispersion relation of plasmonic nanostructure influencing the directional light emission [21, 33]. In other words, the variation in the direction emission of

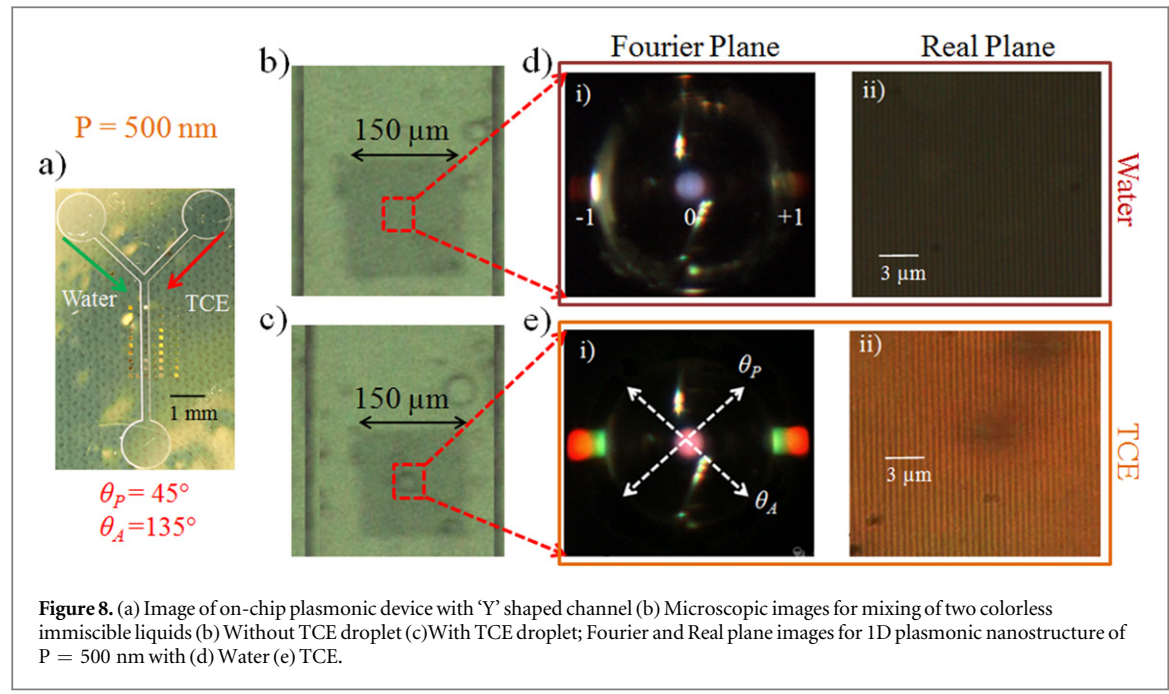


**Figure 8.** (a) Image of on-chip plasmonic device with 'Y' shaped channel (b) Microscopic images for mixing of two colorless immiscible liquids (b) Without TCE droplet (c) With TCE droplet; Fourier and Real plane images for 1D plasmonic nanostructure of  $P = 500 \text{ nm}$  with (d) Water (e) TCE.

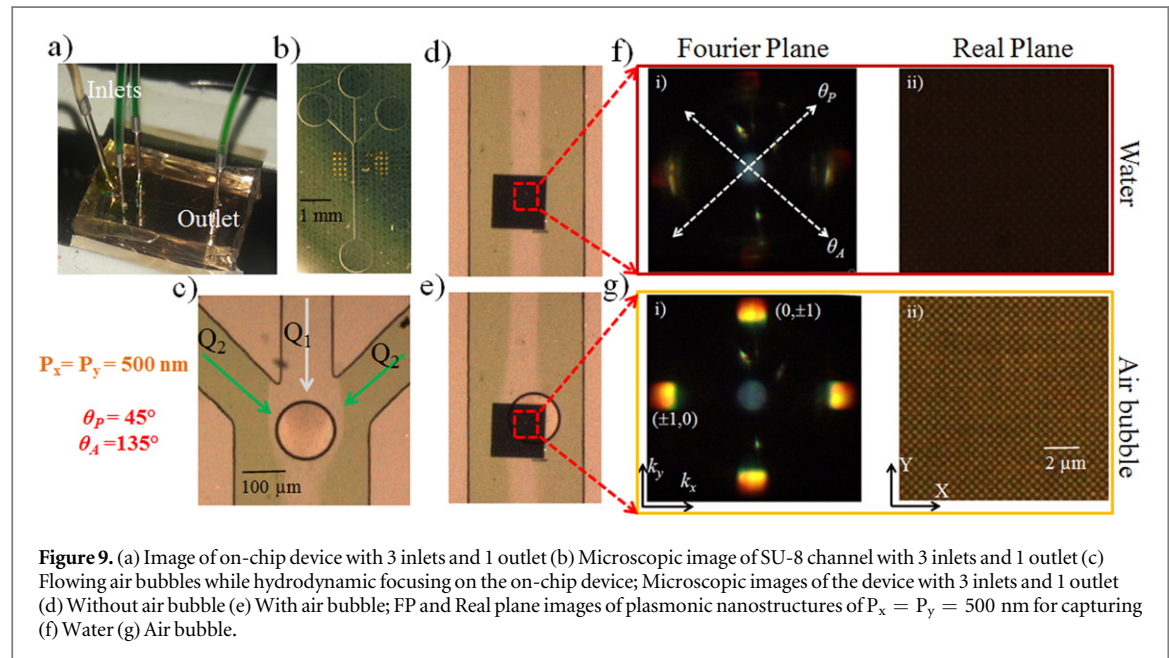


**Figure 9.** (a) Image of on-chip device with 3 inlets and 1 outlet (b) Microscopic image of SU-8 channel with 3 inlets and 1 outlet (c) Flowing air bubbles while hydrodynamic focusing on the on-chip device; Microscopic images of the device with 3 inlets and 1 outlet (d) Without air bubble (e) With air bubble; FP and Real plane images of plasmonic nanostructures of  $P_x = P_y = 500 \text{ nm}$  for capturing (f) Water (g) Air bubble.

captured surface plasmons by increasing/decreasing the refractive index of analytes leads to the change in the color of FP images.

#### Capturing air bubbles in real and FP images using hydrodynamic focusing

Hydrodynamic focusing was also demonstrated on presented on-chip device where the width of the hydrodynamically focused stream of one liquid was controlled by the relative flow rates of the three liquids. The most common configuration is a 3-inlets-1-outlet device which was fabricated and tested that allowed to capture the flow of air bubbles on plasmonic nanostructures with real and FP images through hydrodynamic focusing.

Figures 9(a)–(b) show the image for on-chip device and SU-8 channel with 3 inlets and 1 outlet respectively. The DI water, with green food color added manually (For visualization purposes), was passed through the outer inlets, whereas, the DI water without any color was passed through the middle inlet. The flow rate of the middle inlet was kept fixed to  $Q_1 = 4 \mu\text{l min}^{-1}$ , while, the flow rate in left and right inlets was changed from  $1.5 \mu\text{l min}^{-1}$  to  $4 \mu\text{l min}^{-1}$  in step of  $0.5 \mu\text{l min}^{-1}$  with help of syringe pumps. The idea to change the flow rate of outer inlets from  $1.5 \mu\text{l min}^{-1}$  to  $4 \mu\text{l min}^{-1}$  in steps was to demonstrate the hydrodynamic focusing, in other words by varying the flow rates, it is possible to get the focused stream for middle inlet. After achieving the

hydrodynamic focusing, the air bubbles were introduced through middle inlet with water as shown in figures 9(c)–(e) and the images of the air bubbles passing through fabricated 2D nanostructures of  $P_x = P_y = 500$  nm were captured in FP and real plane as shown in figures 9(f) and (g) respectively. The change in color from dark red to yellow brown was clearly observed in FP and real plane images as air bubble passed through sensing sites (In this case 2D plasmonic nanostructures with metallic pillars of  $P_x = P_y = 500$  nm). This imaging technique on proposed fabricated plasmonic structures can be used to count the number of air bubbles or cells for bio applications [34].

## Conclusions

The optofluidic integration using microfluidic channels on engineered fabricated plasmonic nanostructures was carried out to demonstrate the real-time index sensing. The analytes of different refractive indices were introduced on the sensing sites through SU-8 microfluidic channels and the change in the color corresponding to SP excitation wavelengths was captured in real and FP images. An index resolution of  $1.63 \times 10^{-4}$  RIU was achieved by quantifying CMYK components of images. Label-free imaging of the interface of colorless miscible and immiscible liquids flowing in laminar flow regime in the microfluidic channels was presented by using the color-selective filtering nature of plasmonic nanostructures. Hydrodynamic focusing was demonstrated on presented on-chip plasmonic device and the flow of air bubbles passing though channel on plasmonic nanostructures was captured in FP and real images due to change in refractive index from water to air. The purpose of the work is to establish the foundation of on-chip label-free imaging microscopy to avoid fluorescence tagging and to provide a simple platform where the optical image could be visually interpreted for surface modifications.

## Acknowledgments

The authors would like to thank Centre for NEMS and Nano Photonics (CNNP) for the use of fabrication facilities. The authors are thankful to Prof. Ashis Sen for allowing to use the facilities of Microfluidics lab and Dr P. Sajeesh for many fruitful discussions related to microfluidics.

## ORCID iDs

P Arora  <https://orcid.org/0000-0002-0451-9518>

## References

- [1] Sinton D 2004 Microscale flow visualization *Microfluidics and Nanofluidics* **1** 2–21
- [2] Ng A H C, Uddayasanakar U and Wheeler A R 2010 Immunoassays in microfluidic systems *Analytical and Bioanalytical Chemistry* **397** 991–1007
- [3] Fujii T 2002 PDMS-based microfluidic devices for biomedical applications *Microelectron. Eng.* **61–62** 907–14
- [4] Thrush E, Levi O, Cook L J, Deich J, Kurtz A, Smith S J, Moerner W E and Harris J S 2005 Monolithically integrated semiconductor fluorescence sensor for microfluidic applications *Sensors and Actuators, B: Chemical* **105** 393–9
- [5] Shi Y Z *et al* 2018 Sculpting nanoparticle dynamics for single-bacteria-level screening and direct binding-efficiency measurement *Nat. Commun.* **9** 1–11
- [6] Masters B R 2008 Principles of fluorescence spectroscopy *J. Biomed. Opt.* **13** 29901
- [7] Berezin M Y, Akers W J, Guo K, Fischer G M, Daltrozzo E, Zumbusch A and Achilefu S 2009 Long fluorescence lifetime molecular probes based on near infrared pyrrolopyrrole cyanine fluorophores for *in vivo* imaging *Biophys. J.* **97** L22–4
- [8] Klostranec J M, Xiang Q, Farcas G A, Lee J A, Rhee A, Lafferty E I, Perrault S D, Kain K C and Chan W C W 2007 Convergence of quantum dot barcodes with microfluidics and signal processing for multiplexed high-throughput infectious disease diagnostics *Nano Lett.* **7** 2812–8
- [9] Hsiao A, Gartia M R, Chang T W, Wang X, Khumwan P and Liu G L 2015 Colorimetric plasmon resonance microfluidics on nanohole array sensors *Sensing and Bio-Sensing Research* **5** 24–32
- [10] Ameen A, Gartia M R, Hsiao A, Chang T W, Xu Z and Liu G L 2015 Ultra-sensitive colorimetric plasmonic sensing and microfluidics for biofluid diagnostics using nanohole array *Journal of Nanomaterials* **16** 1–21
- [11] De Vos K, Bartolozzi I, Schacht E, Bienstman P and Baets R 2007 Silicon-on-insulator microring resonator for sensitive and label-free biosensing *Opt. Express* **15** 7610–5
- [12] Lin P T, Kwok S W, Lin H Y G, Singh V, Kimerling L C, Whitesides G M and Agarwal A 2014 Mid-infrared spectrometer using opto-nanofluidic slot-waveguide for label-free on-chip chemical sensing *Nano Lett.* **14** 231–8
- [13] Wang L, Wang L, Yin H, Xing W, Yu Z, Guo M and Cheng J 2010 Real-time, label-free monitoring of the cell cycle with a cellular impedance sensing chip *Biosensors and Bioelectronics* **25** 990–5
- [14] Arora P, Talker E, Mazurski N and Levy U 2018 Dispersion engineering with plasmonic nano structures for enhanced surface plasmon resonance sensing *Sci. Rep.* **8** 1–9
- [15] Gordon R, Sinton D, Kavanagh K L and Brolo A G 2008 A New Generation of Sensors Based on Extraordinary Optical Transmission *Acc. Chem. Res.* **41** 1049–57

- [16] De Leebeck A, Kumar L K S, De Lange V, Sinton D, Gordon R and Brolo A G 2007 On-chip surface-based detection with nanohole arrays *Anal. Chem.* **79** 4094–100
- [17] Eftekhari F, Escobedo C, Ferreira J, Duan X, Girotto E M, Brolo A G, Gordon R and Sinton D 2009 Nanoholes as nanochannels: flow-through plasmonic sensing *Anal. Chem.* **81** 4308–11
- [18] Chamanzar M, Xia Z, Yegnanarayanan S and Adibi A 2013 Hybrid integrated plasmonic-photonic waveguides for on-chip localized surface plasmon resonance (LSPR) sensing and spectroscopy *Opt. Express* **21** 32086–98
- [19] Liu P Y *et al* 2016 Cell refractive index for cell biology and disease diagnosis: past, present and future *Lab on a Chip* **16** 634–44
- [20] Wu P C, Zhu W, Shen Z X, Chong P H J, Ser W, Tsai D P and Liu A Q 2017 Broadband wide-angle multifunctional polarization converter via liquid-metal-based metasurface *Advanced Optical Materials* **5** 1–7
- [21] Arora P and Krishnan A 2015 Fourier plane colorimetric sensing using broadband imaging of surface plasmons and application to biosensing *J. Appl. Phys.* **118** 1–10
- [22] Khorasaninejad M, Abedzadeh N, Walia J, Patchett S and Saini S S 2012 Color matrix refractive index sensors using coupled vertical silicon nanowire arrays *Nano Lett.* **12** 4228–34
- [23] Arora P and Krishnan A 2016 Stain free colorimetric sensors using hybrid mode plasmonic microscopy *CLEO : 2016* (San Jose: OSA) pp 1–2
- [24] Zeng B, Gao Y and Bartoli F J 2013 Ultrathin nanostructured metals for highly transmissive plasmonic subtractive color filters *Sci. Rep.* **3** 1–9
- [25] Yokogawa S, Burgos S P and Atwater H A 2012 Plasmonic color filters for CMOS image sensor applications *Nano Lett.* **12** 4349–54
- [26] Wu P C, Sun G, Chen W T, Yang K Y, Huang Y W, Chen Y H, Huang H L, Hsu W L, Chiang H P and Tsai D P 2014 Vertical split-ring resonator based nanoplasmonic sensor *Appl. Phys. Lett.* **105** 1–4
- [27] Arora P and Krishnan A 2014 Imaging the engineered polarization states of surface plasmon polaritons at visible wavelengths *J. Lightwave Technol.* **32** 4816–22
- [28] Khorasaninejad M, Mohsen Raeis-Zadeh S, Amarloo H, Abedzadeh N, Safavi-Naeini S and Saini S S 2013 Colorimetric sensors using nano-patch surface plasmon resonators *Nanotechnology* **24** 1–10
- [29] Arora P and Krishnan A 2013 Analysis of transmission characteristics and multiple resonances in plasmonic gratings coated with homogeneous dielectrics *Progress In Electromagnetics Research Symp. Proc., 2013* vol 1 (Taipei) pp 927–31
- [30] Chamanzar M 2012 *Hybrid Nanoplasmonic-Nanophotonic Devices for on-Chip Devices for on-Chip Biochemical Sensing and Spectroscopy* Georgia Institute of Technology
- [31] Surya H P N, Parayil S, Banerjee U, Chander S and Sen A K 2015 Alternating and merged droplets in a double T-junction microchannel *Biochip Journal* **9** 16–26
- [32] Arora P 2016 *Colorimetric Sensors Using Hybrid Mode Plasmon Imaging for Refractive Index and Thickness Sensing* Indian Institute of Technology Madras
- [33] Fontana Y, Grzela G, Bakkers E P A M and Rivas J G 2012 Mapping the directional emission of quasi-two-dimensional photonic crystals of semiconductor nanowires using Fourier microscopy *Physical Review B—Condensed Matter and Materials Physics* **86** 1–7
- [34] Shi Y *et al* 2018 Nanometer-precision linear sorting with synchronized optofluidic dual barriers *Science Advances* **4** 1–9

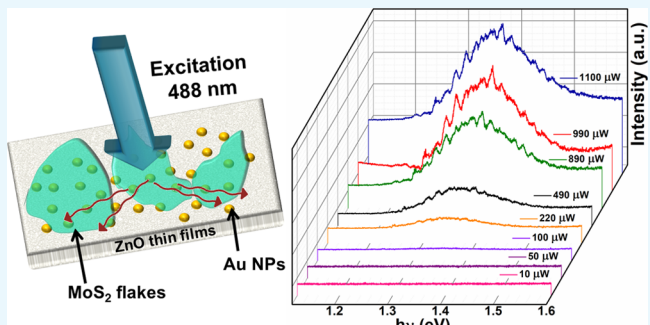
# Near Infrared Random Lasing in Multilayer MoS<sub>2</sub>

Tejendra Dixit,<sup>†,§</sup> Ankit Arora,<sup>†,‡,§</sup> Ananth Krishnan,<sup>‡</sup> K. Lakshmi Ganapathi,<sup>\*,†</sup> Pramoda K. Nayak,<sup>\*,†</sup> and M. S. Ramachandra Rao<sup>\*,†,§</sup>

<sup>†</sup>Department of Physics and Materials Science Research Centre, <sup>‡</sup>Centre for NEMS and Nano Photonics (CNNP), Department of Electrical Engineering, and <sup>§</sup>Nano Functional Materials Technology Centre, Indian Institute of Technology Madras, Chennai 600 036, India

## Supporting Information

**ABSTRACT:** We demonstrated room temperature near infrared (NIR) region random lasing (RL) (800–950 nm), with a threshold of nearly 500 μW, in ~200 nm thick MoS<sub>2</sub>/Au nanoparticles (NPs)/ZnO heterostructures using photoluminescence spectroscopy. The RL in the above system arises mainly due to the following three reasons: (1) enhanced multiple scattering because of Au/ZnO disordered structure, (2) exciton–plasmon coupling because of Au NPs, and (3) enhanced charge transfer from ZnO to thick MoS<sub>2</sub> flakes. RL has recently attracted tremendous interest because of its wide applications in the field of telecommunication, spectroscopy, and specifically in biomedical tissue imaging. This work provides new dimensions toward realization of low power on-chip NIR random lasers made up of biocompatible materials.



## 1. INTRODUCTION

Random lasing (RL) is one of the lasing phenomena that arises due to simultaneous action of optical gain and amplification by multiple scattering.<sup>1–3</sup> A random laser is different from a traditional laser in the sense that the feedback amplification is not provided by a cavity formed by reflection components, but by disorder-induced scattering. Because of ease of its fabrication, it is gaining popularity in a variety of applications like biomedical imaging and optical information processing.<sup>2</sup> Use of various plasmonic nanoparticles (NPs) as well as the new class of host materials including semiconductors, quantum dots, and so forth led to renewed interest in the area of random lasers and their applications over last decade.<sup>2,4–6</sup> RL in the spectral range from ultraviolet to visible region has been explored in variety of materials in literature.<sup>4,5,7,8</sup> However, there are few reports about near infrared (NIR) RL so far, which has the following advantages including telecommunication, spectroscopy, displays, and biomedical tissue imaging.<sup>9–11</sup> In addition, because the NIR window of tissue imaging falls in the range 650–1300 nm, NIR lasing using biocompatible materials is extremely needed.

Two-dimensional (2D) transition-metal dichalcogenides (TMDs) have recently attracted significant interest because of their intriguing physical/chemical properties and have huge potential applications in future optoelectronic, nanoelectronic, and spin-valleytronic devices.<sup>12–19</sup> Among the 2D TMDs, molybdenum disulfide (MoS<sub>2</sub>) is very promising candidate, which exhibits indirect optical band gap of 1.2 eV in bulk phase to direct band gap of 1.9 eV in monolayer limit.<sup>13,14,20,21</sup> However, the relatively small optical density of states and limited photon absorbing/emitting ability of monolayer MoS<sub>2</sub>

restrict its practical device applications.<sup>22–24</sup> The realization of lasing in the visible region has been already reported in monolayer MoS<sub>2</sub>.<sup>25,26</sup> As a counterpart of monolayer species, a few layer MoS<sub>2</sub> with thickness <100 nm (TnM) shows low luminescence quantum yield because of their indirect band gap nature. However, thick MoS<sub>2</sub> with thickness >100 nm (TkM) still holds some obvious superiorities compared with monolayer in terms of stronger photon absorption ability, higher optical density of states, and ability to withstand substantially higher injection currents, which are advantageous for light-emitting devices and solar energy conversion.<sup>23,27</sup> Moreover, as MoS<sub>2</sub> is biocompatible and the indirect band gap of TkM lies in the NIR region, it may be possible to build future optoelectronic devices using indirect band gap emission for NIR application.<sup>23,28</sup> However, RL is not possible from MoS<sub>2</sub> alone and needs an additional charge-transfer medium to invoke population inversion.

ZnO exhibits a direct wide band gap (~3.37 eV) in the UV region and defect-assisted deep level emission in the visible to NIR region and hence is a very suitable material for tunable light emission and photodetection.<sup>29–39</sup> It has been shown that ZnO can be used to tune the optical properties of 1L-TMDs by controlling the charge carrier density.<sup>40</sup> This is due to the fact that the electronic band structures of 1L-TMD/ZnO heterostructure (HS) form the type-II band alignment, where the effective charge transfer occurs at the interface between 1L-TMDs and ZnO that would enhance the photoluminescence

Received: June 8, 2018

Accepted: October 2, 2018

Published: October 25, 2018

(PL) of 1L-TMDs.<sup>40–42</sup> PL enhancement in the visible region has been observed in several such HSs including MoS<sub>2</sub>/ZnO and WSe<sub>2</sub>/ZnO by considering monolayer or few layer TMDs.<sup>40,43–45</sup> However, to the best of our knowledge, there is no report so far about the indirect band gap PL enhancement using TMD/ZnO HSs.

In this work, we have prepared TkM/ZnO thin film HSs and observed enhanced indirect PL emission of MoS<sub>2</sub>. To further enhance the indirect emission, we have incorporated Au NPs at the TkM/ZnO interface and interestingly observed RL in the NIR region. To understand the charge-transfer mechanism and to calculate lasing threshold, we have studied excitation power-dependent PL spectra of TkM/Au/ZnO HSs. On the basis of the above analysis, we have proposed a possible mechanism for lasing in the above system. The demonstration of NIR RL with the integration of MoS<sub>2</sub>, Au, and ZnO has potential to open new dimensions toward future optical technologies because of their biocompatibility, ease of fabrication, and on-chip fabrication suitability.

## 2. MATERIALS AND METHODS

**2.1. Synthesis of ZnO Thin Films.** A sol–gel process was employed for ZnO thin film deposition on glass substrate. In particular, an equi-molar solution (2 M) of anhydrous zinc acetate and ethanolamine in 2-methoxyethanol was spin coated on the glass substrate at 3000 rpm. Here, ethanolamine has a role of stabilizer. Spin-coated samples were annealed at 250 °C for throwing out organic impurities and improving the adhesion of ZnO thin film with the substrate. The deposition of 5 nm thick Au on these ZnO thin films was subsequently carried out by using dc sputtering system [Quorum (Q-150 RES)]. The thickness of Au coating was measured using inbuilt crystal detectors. UV–visible absorption spectra were recorded by a Cary 60 UV–vis spectrometer (Agilent Technologies) with a range of wavelengths from 200 to 800 nm.

**2.2. Preparation of MoS<sub>2</sub> Flakes and TkM/Au/ZnO HSs.** High-purity MoS<sub>2</sub> crystal was procured from Graphene Supermarket and mechanically exfoliated on 285 nm SiO<sub>2</sub>/Si, ZnO thin film and Au/ZnO to get desired HSs.

**2.3. AFM, SEM, PL, and Raman Measurements.** Atomic force microscope (AFM) measurement was carried out in tapping mode using Bruker edge dimension system. Scanning electron microscope (SEM) measurements were carried out with Quanta 400 FEG SEM. TnM, TkM, ZnO thin films, Au/ZnO, and TkM/Au/ZnO HSs were investigated using PL and Raman spectroscopy (HORIBA LabRAM). All of the measurements were carried out in a confocal microscopy setup using 488 nm continuous wave laser with spot size ~1 μm, in which we can readily locate and selectively excite HSs of different layer thicknesses.

## 3. RESULTS AND DISCUSSIONS

Figure 1a,b shows the room-temperature PL spectra of TnM and TkM flakes transferred on SiO<sub>2</sub>/Si substrates (corresponding AFM images are shown in Figure S1). MoS<sub>2</sub> multilayers usually show two distinguishable peaks with peak positions at 1.84 and 1.35 eV.<sup>20,23,46</sup> The peak observed at 1.84 eV with higher intensity corresponds to A direct exciton transition, while the other peak at 1.35 eV with lower intensity can be assigned to the indirect transition (i.e., transition of electrons from I-valley to K point).<sup>20,21</sup> In contrast, TkM (thickness of ~200 nm used in this work) has shown interesting features

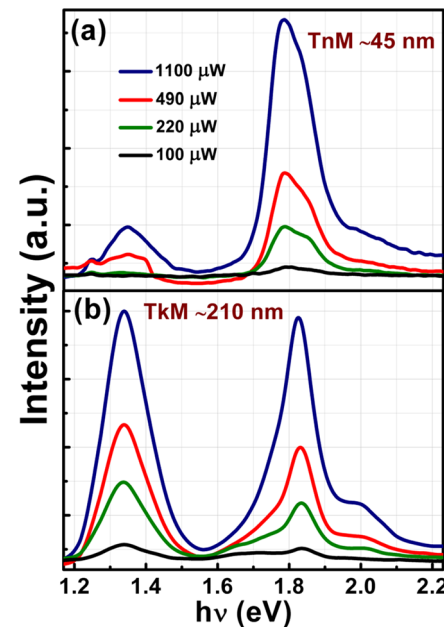


**Figure 1.** Room temperature PL spectra of MoS<sub>2</sub> flakes on 285 nm SiO<sub>2</sub>/Si substrate using 488 nm laser. Excitation power-dependent PL spectra of (a) TnM flakes with thickness ~45 nm and (b) TkM flakes with thickness ~210 nm. Black, green, red, and blue colors represent the laser excitation power of 100, 220, 490, and 1100 μW, respectively. Two distinguishable peaks are observed for all flakes, in which peak at 1.84 eV corresponds to direct exciton transition and at 1.35 eV corresponds to indirect transition.

with nearly equal probability for both direct and indirect transitions. Additionally, the B direct exciton transition was observed as a shoulder peak with peak position close to 2.0 eV for both thin and thick flakes. In case of TnM the main excitonic peak can be de-convoluted into two close peaks, that is, A trion and A exciton (see Figure S2). The origin of A<sup>-</sup> trion can be attributed to the charge transfer from SiO<sub>2</sub> substrate to MoS<sub>2</sub>, which can be clearly seen as a red shift in the A peak position by 15 meV (close to trion binding energy).<sup>47,48</sup> However, for TkM films with thicknesses ~210 nm, the substrate effect was found to be negligible. The ratio of the peak intensities corresponding to direct and indirect excitonic transitions were observed to be almost invariant with the variation of excitation power. Room-temperature Raman spectra measured on MoS<sub>2</sub> flakes are shown in Figure S3. The Raman spectra of MoS<sub>2</sub> consist of two characteristic peaks at 385 and 405 cm<sup>-1</sup> corresponding to E<sub>2g</sub> and A<sub>1g</sub> modes, respectively.<sup>49</sup> The difference in the Raman shift between these two peaks was found to be ~25 cm<sup>-1</sup>, which is in good agreement with the previously reported value for TkM flakes.<sup>49,50</sup> Similar to PL spectra, the peak positions were observed to be invariant for different excitation power. In addition to this, the full-width at half maximum for these peaks monotonically decreased with the decrease in the excitation power.

To investigate the effect of ZnO on MoS<sub>2</sub> flakes, both TnM and TkM were transferred onto sol–gel derived ZnO thin films. The excitation power-dependent PL spectra of TnM/ZnO HSs were observed to be dominated by ZnO emission in the range of 1.6–2.4 eV as shown in Figure S4 and did not show well-defined emission in the NIR region. Therefore, it was not considered for further analysis. On the other hand, the

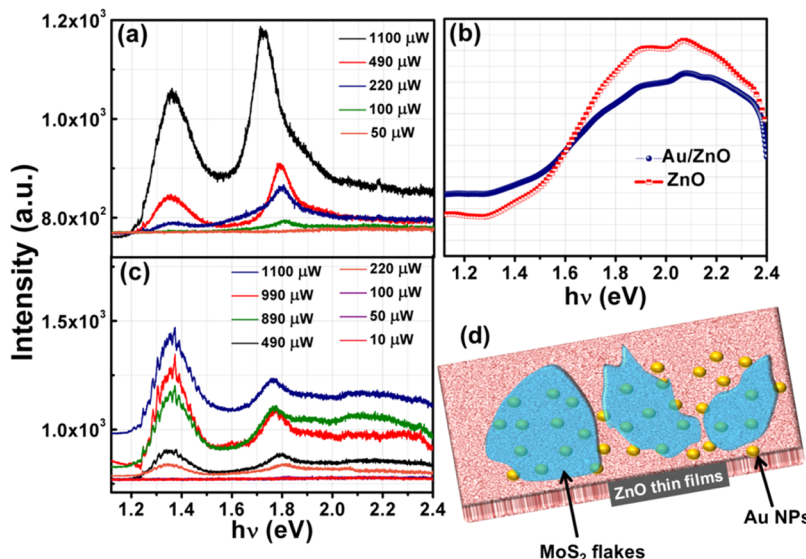


**Figure 2.** (a) Excitation power-dependent PL spectra of TkM/ZnO HSs showing significant NIR emission. (b) PL spectra of pristine (blue squares) and Au-coated ZnO thin films (red squares) in the range 1.2–2.4 eV. (c) Excitation power-dependent PL spectra of TkM/Au NPs/ZnO HSs. NIR emission is found to be significantly enhanced along with sharp and narrow peaks over the envelope, which increases with the increase in excitation power. Pink, magenta, purple, orange, black, green, red, and blue colors represent the laser excitation power of 10, 50, 100, 220, 490, 890, 990, and 1100  $\mu\text{W}$ , respectively. (d) Schematic of TkM/Au NPs/ZnO HSs, in which mosaic red represents ZnO thin film, blue flakes represent TkM and golden spheres represent Au NPs.

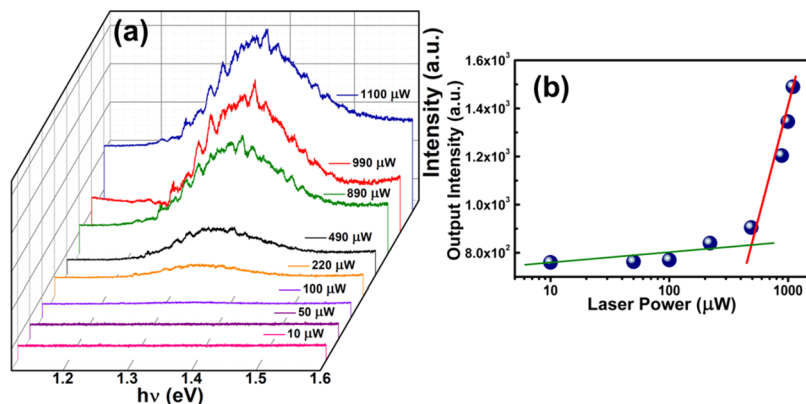


**Figure 3.** (a) Excitation power-dependent NIR emission of TkM/Au/ZnO HSs. The spectra are plotted in waterfall mode for clarity. Pink, magenta, purple, orange, black, green, red, and blue colors represent the laser excitation power of 10, 50, 100, 220, 490, 890, 990, and 1100  $\mu\text{W}$ , respectively. (b) PL intensity vs excitation power of above HSs. The lasing threshold has been estimated to be  $\sim 500 \mu\text{W}$ .

PL spectra of TkM/ZnO HSs showed significant NIR emission as shown in Figure 2a. To probe deeper, we recorded the excitation power-dependent PL spectra of TkM/ZnO HSs. The PL spectra of TkM/ZnO HSs showed red shift of direct A transitions in comparison to TkM/SiO<sub>2</sub> films (Figure 1b). MoS<sub>2</sub>/ZnO HSs exhibit type-II band alignment and therefore band bending is expected to align the Fermi levels.<sup>41</sup> The conduction band (CB) of MoS<sub>2</sub> followed downward band bending while making an interface with ZnO. Hence, the exciton population of both layers were affected by the charge accumulation at the interface and that made an impact on the ratio of indirect to direct peak values for MoS<sub>2</sub>/ZnO HSs. The excitation power-dependent red shift in the position of A exciton peak can be assigned to the photo-induced modulation of MoS<sub>2</sub> dielectric function, thus resulting into the decrease of exciton binding energy.<sup>51</sup> Tuning of A exciton transition of monolayer MoS<sub>2</sub> using ZnO thin film was demonstrated by Kim et al. in MoS<sub>2</sub>/ZnO HSs.<sup>40</sup> Figure S5 shows the PL

spectrum of TkM/ZnO HS in the region of indirect transition only for laser excitation power of 1100  $\mu\text{W}$ . In contrast to pristine MoS<sub>2</sub> films as mentioned earlier, this HS showed signature of amplified spontaneous emission (ASE) for the transitions related to I-valley as shown in Figure 2a for 1100  $\mu\text{W}$  power (the zoomed spectra corresponding to NIR region is shown in Figure S5). Additionally, the PL spectrum of ZnO thin film is shown in Figure 2b in the range 1.2–2.4 eV, and it was found to be luminescent in the visible and relatively nonluminescent in the region of I-valley of MoS<sub>2</sub>. It must be noted here that sol-gel processed ZnO is prone to defect states like oxygen vacancies and interstitials,<sup>52,53</sup> and hence, their interaction with excitonic transitions of MoS<sub>2</sub> cannot be ignored.

The observation of ASE in the indirect exciton transition has triggered its further exploration. It is well known that metal NPs are good candidates for enhancing light scattering mainly because of surface plasmon resonance.<sup>54–56</sup> In the present

work, we have strategically used Au NPs to get enhanced scattering to have lasing. With the insertion of Au between TkM and ZnO thin films, drastic change in the PL spectra was observed as shown in Figure 2c. The schematic of TkM/Au NPs/ZnO HS is shown in Figure 2d. The corresponding AFM image is shown in Figure S6. Figure S7 shows the typical SEM image of the TkM/Au/ZnO HS. Interestingly, significant enhancement in the emissions corresponding to the I-valley was observed (Figure 2c) along with sharp and narrow peaks over the envelope, which was found to be excitation power dependent. Such features were found to be absent both in pristine MoS<sub>2</sub> and TkM/ZnO HS. In addition, a red shift was observed in the peak corresponding to A direct transitions, which was also found to increase with increase in excitation power.

Figure 3a presents the excitation power-dependent emission in the NIR region of TkM/Au/ZnO HS by varying laser power in the range 10–1100 μW. It was found that the emission intensity increased abruptly beyond excitation power of 490 μW along with the emergence of sharp spike-like peaks over the entire envelope. At lower excitation power (<490 μW), no such sharp peaks were observed. The appearance of the sharp spike-like peaks indicates that RL occurs due to recurrent scattering in the disordered medium of TkM/Au/ZnO. It was observed that the position and intensities of these spike-like peaks were fluctuating for different readings, which is the characteristic of nonresonant feedback.<sup>2</sup> There could be three possible reasons for the origin of such peaks: (1) Fabry–Perot, (2) whispering gallery mode, and (3) RL. As the surface of Au/ZnO is not smooth enough, existence of Fabry–Perot between TkM and Au/ZnO can be neglected. Secondly, whispering gallery mode can also be discarded because of irregular geometry of TkM flakes. Hence, the possible mechanism can be RL only. We have carried out fast Fourier transform analysis for the PL spectra recorded with 1100 μW excitation power. Two side peaks along with the central peak can be clearly seen in the Figure S8, which confirms that the peaks are due to RL and not the noise. The increase in the lasing intensity was found to be nonlinear in nature, as shown in Figure 3b. The change in PL intensity versus excitation power showed an increase in slope indicating the onset of lasing and the lasing threshold was estimated to be approximately 500 μW.

On the basis of the feedback mechanism, RL can be categorized into two types: incoherent when it is phase insensitive and coherent when it is phase sensitive. In a strongly scattering system, multiple scattering facilitates light of wavelength  $\lambda$  to return to the same coherence volume  $\lambda^3$  it has visited before, thereby providing field feedback for lasing.<sup>6,57,58</sup> The lasing frequencies can be determined by the interference of scattered light returning via different paths.<sup>2</sup> On the basis of the above analysis, we propose the possible mechanism as shown in Figure 4.

As mentioned earlier, band bending at the TkM/ZnO junction results in the charge accumulation in the CB of TkM at the interface. However, the charge accumulation was not sufficient enough for the system to lase. Incorporation of Au NPs between TkM and ZnO resulted in lasing possibly because of three following effects: (1) enhanced multiple scattering, (2) exciton–plasmon coupling, and (3) enhanced charge transfer from ZnO to TkM. It is well reported that plasmon resonance of Au NPs can couple with ZnO excitons (the absorption spectra of ZnO and Au/ZnO is shown in

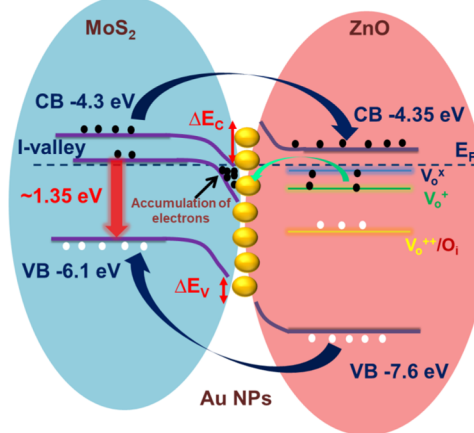


**Figure 4.** Schematic showing the possible mechanism of RL in TkM/Au/ZnO HSs. Band bending at TkM/ZnO junction results in the charge accumulation in the CB of TkM at the interface, however not sufficient enough for the system to lase. Incorporation of Au NPs (golden spheres) between TkM and ZnO results in lasing possibly due to three following effects, that is, enhanced multiple scattering because of Au/ZnO disordered structure, exciton–plasmon coupling because of Au NPs, and enhanced charge transfer from ZnO to thick MoS<sub>2</sub>.

Figure S9; it can be clearly seen that the plasmon resonance peak is present nearly at 528 nm), thereby improving radiative recombination.<sup>59</sup> Because of the difference in work function and electron affinity between ZnO and MoS<sub>2</sub>, electrons present in the ZnO may diffuse into TkM at the interface to match the Fermi levels, which can yield depletion region in the ZnO side and a negatively charged carrier accumulation region in the MoS<sub>2</sub> side. Additionally, the presence of Au will promote the band bending and therefore enforce charge accumulation at MoS<sub>2</sub> CB. Electrons present at defect states of ZnO can be transferred to the Au Fermi level and then to MoS<sub>2</sub> CBs, specifically I-valley, as the later is well matched with the Fermi level of Au. For better understanding, we have recorded the PL spectra using 632 nm laser and found no RL which indicates clear involvement of Au NPs for achieving lasing (shown in Figure S10).

Raman spectra for TkM/Au/ZnO HSs are shown in Figure S11. In contrast to Raman spectra of pristine MoS<sub>2</sub> flakes, here a systematic red shift in the peak positions corresponding to E<sub>2g</sub> and A<sub>1g</sub> modes was observed. The shift in E<sub>2g</sub> mode can be assigned to strain induced due to rough ZnO thin films. Moreover, the shift in A<sub>1g</sub> peak toward lower energy suggests electron transfer from Au/ZnO to TkM.<sup>41,51</sup>

#### 4. CONCLUSIONS

In conclusion, we demonstrated RL action from MoS<sub>2</sub>/Au/ZnO HS in the NIR region. Thick-layer MoS<sub>2</sub> flakes were found to be a potential candidate for NIR emission. The thick-layer MoS<sub>2</sub> flakes while transferred onto ZnO thin films resulted in enhanced indirect emission. To enhance the PL emission further, Au NPs were incorporated at the interface between TkM and ZnO. The resulting TkM/Au/ZnO HS was found to lase in the NIR region (800–950 nm) with lasing threshold of nearly 500 μW. Enhanced multiple scattering because of Au/ZnO disordered structure, exciton–plasmon coupling because of Au NPs, and enhanced charge transfer from ZnO to thick MoS<sub>2</sub> could be the possible reasons for RL in the above HS. The present work opens up new dimensions

toward realization of low power on-chip NIR random lasers made up of biocompatible materials.

## ■ ASSOCIATED CONTENT

### Supporting Information

The Supporting Information is available free of charge on the ACS Publications website at DOI: [10.1021/acsomega.8b01287](https://doi.org/10.1021/acsomega.8b01287).

Detailed description about the experimental methods and additional characterizations ([PDF](#))

## ■ AUTHOR INFORMATION

### Corresponding Authors

\*E-mail: [klganapathi@iitm.ac.in](mailto:klganapathi@iitm.ac.in) (K.L.G.).

\*E-mail: [pnayak@iitm.ac.in](mailto:pnayak@iitm.ac.in) (P.K.N.).

\*E-mail: [msrrao@iitm.ac.in](mailto:msrrao@iitm.ac.in) (M.S.R.R.).

### ORCID

Pramoda K. Nayak: [0000-0002-2569-0517](https://orcid.org/0000-0002-2569-0517)

### Notes

The authors declare no competing financial interest.

## ■ ACKNOWLEDGMENTS

This work was partially supported by Department of Science and Technology (DST) that led to the establishment of Nano Functional Materials Technology Centre (NFMTC) (SR/NM/NAT/02-2005). P.K.N. acknowledge the financial support from Department of Science and Technology, India, with sanction order no. SERB/F/5379/2017–2018 under Ramanujan Fellowship. K.L.G. acknowledge the financial support from Department of Science and Technology, India, with sanction order no. DST/INSPIRE/04/2016/001865 under DST INSPIRE Faculty program. T.D. would like to thank IIT Madras for proving institute postdoctoral fellowship.

## ■ REFERENCES

- (1) Wiersma, D. S. Disordered Photonics. *Nat. Photonics* **2013**, *7*, 188–196.
- (2) Luan, F.; Gu, B.; Gomes, A. S. L.; Yong, K.-T.; Wen, S.; Prasad, P. N. Lasing in Nanocomposite Random Media. *Nano Today* **2015**, *10*, 168–192.
- (3) Cao, H.; Jiang, X.; Ling, Y.; Xu, J. Y.; Soukoulis, C. M. Mode Repulsion and Mode Coupling in Random Lasers. *Phys. Rev. B: Condens. Matter Mater. Phys.* **2003**, *67*, 161101.
- (4) Abiyasa, A. P.; Yu, S. F.; Lau, S. P.; Leong, E. S. P.; Yang, H. Y. Enhancement of Ultraviolet Lasing from Ag-Coated Highly Disordered ZnO Films by Surface-Plasmon Resonance. *Appl. Phys. Lett.* **2007**, *90*, 231106.
- (5) Fallert, J.; Dietz, R. J. B.; Sartor, J.; Schneider, D.; Klingshirn, C.; Kalt, H. Co-Existence of Strongly and Weakly Localized Random Laser Modes. *Nat. Photonics* **2009**, *3*, 279–282.
- (6) Wiersma, D. S. The Physics and Applications of Random Lasers. *Nat. Phys.* **2008**, *4*, 359–367.
- (7) Zhu, H.; Shan, C.-X.; Zhang, J.-Y.; Zhang, Z.-Z.; Li, B.-H.; Zhao, D.-X.; Yao, B.; Shen, D.-Z.; Fan, X.-W.; Tang, Z.-K.; et al. Low-Threshold Electrically Pumped Random Lasers. *Adv. Mater.* **2010**, *22*, 1877–1881.
- (8) Krämer, S.; Vannahme, C.; Smith, C. L. C.; Grossmann, T.; Jenne, M.; Schierle, S.; Jørgensen, L.; Chronakis, I. S.; Kristensen, A.; Kalt, H. Random-Cavity Lasing from Electrospun Polymer Fiber Networks. *Adv. Mater.* **2014**, *26*, 8096–8100.
- (9) Wang, X.; Liao, Q.; Li, H.; Bai, S.; Wu, Y.; Lu, X.; Hu, H.; Shi, Q.; Fu, H. Near-Infrared Lasing from Small-Molecule Organic Hemispheres. *J. Am. Chem. Soc.* **2015**, *137*, 9289–9295.
- (10) Wirths, S.; Mayer, B. F.; Schmid, H.; Sousa, M.; Gooth, J.; Riel, H.; Moselund, K. E. Room-Temperature Lasing from Monolithically Integrated GaAs Microdisks on Silicon. *ACS Nano* **2018**, *12*, 2169–2175.
- (11) Wang, X.; Li, Z.-Z.; Zhuo, M.-P.; Wu, Y.; Chen, S.; Yao, J.; Fu, H. Tunable Near-Infrared Organic Nanowire Nanolasers. *Adv. Funct. Mater.* **2017**, *27*, 1703470.
- (12) Cheng, R.; Li, D.; Zhou, H.; Wang, C.; Yin, A.; Jiang, S.; Liu, Y.; Chen, Y.; Huang, Y.; Duan, X. Electroluminescence and Photocurrent Generation from Atomically Sharp WSe<sub>2</sub>/MoS<sub>2</sub> Heterojunction P – N Diodes. *Nano Lett.* **2014**, *14*, 5590–5597.
- (13) Glazov, M. M.; Ivchenko, E. L.; Wang, G.; Amand, T.; Marie, X.; Urbaszek, B.; Liu, B. L. Spin and Valley Dynamics of Excitons in Transition Metal Dichalcogenide Monolayers. *Phys. Status Solidi B* **2015**, *252*, 2349–2362.
- (14) Lagarde, D.; Bouet, L.; Marie, X.; Zhu, C. R.; Liu, B. L.; Amand, T.; Tan, P. H.; Urbaszek, B. Carrier and Polarization Dynamics in Monolayer MoS<sub>2</sub>. *Phys. Rev. Lett.* **2014**, *112*, 047401.
- (15) Mak, K. F.; He, K.; Shan, J.; Heinz, T. F. Control of valley polarization in monolayer MoS<sub>2</sub> by optical helicity. *Nat. Nanotechnol.* **2012**, *7*, 494–498.
- (16) Mai, C.; Barrette, A.; Yu, Y. Many-Body E FF Ects in Valleytronics: Direct Measurement of Valley Lifetimes in Single-Layer MoS<sub>2</sub>. *Nano Lett.* **2013**, *14*, 202–206.
- (17) Radisavljevic, B.; Radenovic, A.; Brivio, J.; Giacometti, V.; Kis, A. Single-layer MoS<sub>2</sub> transistors. *Nat. Nanotechnol.* **2011**, *6*, 147–150.
- (18) Nayak, P. K.; Horbatenko, Y.; Ahn, S.; Kim, G.; Lee, J.-U.; Ma, K. Y.; Jang, A.-R.; Lim, H.; Kim, D.; Ryu, S.; et al. Probing Evolution of Twist-Angle-Dependent Interlayer Excitons in MoSe<sub>2</sub>/WSe<sub>2</sub> van der Waals Heterostructures. *ACS Nano* **2017**, *11*, 4041–4050.
- (19) Nayak, P. K.; Lin, F.-C.; Yeh, C.-H.; Huang, J.-S.; Chiu, P.-W. Robust room temperature valley polarization in monolayer and bilayer WS<sub>2</sub>. *Nanoscale* **2016**, *8*, 6035–6042.
- (20) Splendiani, A.; Sun, L.; Zhang, Y.; Li, T.; Kim, J.; Chim, C.-Y.; Galli, G.; Wang, F. Emerging Photoluminescence in Monolayer MoS<sub>2</sub>. *Nano Lett.* **2010**, *10*, 1271–1275.
- (21) Mak, K. F.; Lee, C.; Hone, J.; Shan, J.; Heinz, T. F. Atomically Thin MoS<sub>2</sub>: A New Direct-Gap Semiconductor. *Phys. Rev. Lett.* **2010**, *105*, 136805.
- (22) Dhall, R.; Neupane, M. R.; Wickramaratne, D.; Mecklenburg, M.; Li, Z.; Moore, C.; Lake, R. K.; Cronin, S. Direct Bandgap Transition in Many-Layer MoS<sub>2</sub>by Plasma-Induced Layer Decoupling. *Adv. Mater.* **2015**, *27*, 1573–1578.
- (23) Li, Z.; Ezhilarasu, G.; Chatzakis, I.; Dhall, R.; Chen, C.-C.; Cronin, S. B. Indirect Band Gap Emission by Hot Electron Injection in Metal/MoS<sub>2</sub> and Metal/WSe<sub>2</sub> Heterojunctions. *Nano Lett.* **2015**, *15*, 3977–3982.
- (24) Ganatra, R.; Zhang, Q. Few-Layer MoS<sub>2</sub>: A Promising Layered Semiconductor. *ACS Nano* **2014**, *8*, 4074–4099.
- (25) Ye, Y.; Wong, Z. J.; Lu, X.; Ni, X.; Zhu, H.; Chen, X.; Wang, Y.; Zhang, X. Monolayer Excitonic Laser. *Nat. Photonics* **2015**, *9*, 733–737.
- (26) Salehzadeh, O.; Djavid, M.; Tran, N. H.; Shih, I.; Mi, Z. Optically Pumped Two-Dimensional MoS<sub>2</sub> Lasers Operating at Room-Temperature. *Nano Lett.* **2015**, *15*, 5302–5306.
- (27) Li, Y.; Xu, H.; Liu, W.; Yang, G.; Shi, J.; Liu, Z.; Liu, X.; Wang, Z.; Tang, Q.; Liu, Y. Enhancement of Exciton Emission from Multilayer MoS<sub>2</sub> at High Temperatures: Intervalley Transfer versus Interlayer Decoupling. *Small* **2017**, *13*, 1700157.
- (28) Chou, S. S.; Kaehr, B.; Kim, J.; Foley, B. M.; De, M.; Hopkins, P. E.; Huang, J.; Brinker, C. J.; Dravid, V. P. Chemically Exfoliated MoS<sub>2</sub>as Near-Infrared Photothermal Agents. *Angew. Chem., Int. Ed.* **2013**, *52*, 4160–4164.
- (29) Tsukazaki, A.; Ohtomo, A.; Onuma, T.; Ohtani, M.; Makino, T.; Sumiya, M.; Ohtani, K.; Chichibu, S. F.; Fuke, S.; Segawa, Y.; et al. Repeated Temperature Modulation Epitaxy for P-Type Doping and Light-Emitting Diode Based on ZnO. *Nat. Mater.* **2005**, *4*, 42–46.
- (30) Xu, S.; Xu, C.; Liu, Y.; Hu, Y.; Yang, R.; Yang, Q.; Ryou, J.-H.; Kim, H. J.; Lochner, Z.; Choi, S.; et al. Ordered Nanowire Array

- Blue/near-UV Light Emitting Diodes. *Adv. Mater.* **2010**, *22*, 4749–4753.
- (31) Yang, Q.; Wang, W.; Xu, S.; Wang, Z. L. Enhancing Light Emission of ZnO Microwire-Based Diodes by Piezo-Phototronic Effect. *Nano Lett.* **2011**, *11*, 4012–4017.
- (32) Dai, J.; Xu, C. X.; Sun, X. W. ZnO-Microrod/p-GaN Heterostructured Whispering-Gallery-Mode Microlaser Diodes. *Adv. Mater.* **2011**, *23*, 4115–4119.
- (33) Chu, S.; Wang, G.; Zhou, W.; Lin, Y.; Chernyak, L.; Zhao, J.; Kong, J.; Li, L.; Ren, J.; Liu, J. Electrically Pumped Waveguide Lasing from ZnO Nanowires. *Nat. Nanotechnol.* **2011**, *6*, 506–510.
- (34) Soci, C.; Zhang, A.; Xiang, B.; Dayeh, S. A.; Aplin, D. P. R.; Park, J.; Bao, X. Y.; Lo, Y. H.; Wang, D. ZnO Nanowire UV Photodetectors with High Internal Gain. *Nano Lett.* **2007**, *7*, 1003–1009.
- (35) Bie, Y.-Q.; Liao, Z.-M.; Zhang, H.-Z.; Li, G.-R.; Ye, Y.; Zhou, Y.-B.; Xu, J.; Qin, Z.-X.; Dai, L.; Yu, D.-P. Self-Powered, Ultrafast, Visible-Blind UV Detection and Optical Logical Operation Based on ZnO/GaN Nanoscale P-N Junctions. *Adv. Mater.* **2011**, *23*, 649–653.
- (36) Retamal, J. R. D.; Chen, C.-Y.; Lien, D.-H.; Huang, M. R. S.; Lin, C.-A.; Liu, C.-P.; He, J.-H. Concurrent Improvement in Photogain and Speed of a Metal Oxide Nanowire Photodetector through Enhancing Surface Band Bending via Incorporating a Nanoscale Heterojunction. *ACS Photonics* **2014**, *1*, 354–359.
- (37) Dixit, T.; Palani, I. A.; Singh, V. Insights into Non-Noble Metal Based Nanophotonics: Exploration of Cr-Coated ZnO Nanorods for Optoelectronic Applications. *RSC Adv.* **2018**, *8*, 6820–6833.
- (38) Dixit, T.; Kumar, A.; Palani, I. A.; Singh, V. Surface-plasmon-mediated red and near infrared emission from Au-coated ZnO/ZnCr<sub>2</sub>O<sub>4</sub> nanocomposites. *Scr. Mater.* **2016**, *114*, 84–87.
- (39) Liu, W. Z.; Xu, H. Y.; Wang, C. L.; Zhang, L. X.; Zhang, C.; Sun, S. Y.; Ma, J. G.; Zhang, X. T.; Wang, J. N.; Liu, Y. C. Enhanced Ultraviolet Emission and Improved Spatial Distribution Uniformity of ZnO Nanorod Array Light-Emitting Diodes via Ag Nanoparticles Decoration. *Nanoscale* **2013**, *5*, 8634–8639.
- (40) Kim, M. S.; Roy, S.; Lee, J.; Kim, B. G.; Kim, H.; Park, J.-H.; Yun, S. J.; Han, G. H.; Leem, J.-Y.; Kim, J. Enhanced Light Emission from Monolayer Semiconductors by Forming Heterostructures with ZnO Thin Films. *ACS Appl. Mater. Interfaces* **2016**, *8*, 28809–28815.
- (41) Chen, L.; Xue, F.; Li, X.; Huang, X.; Wang, L.; Kou, J.; Wang, Z. L. Strain-Gated Field Effect Transistor of a MoS<sub>2</sub>-ZnO 2D-1D Hybrid Structure. *ACS Nano* **2016**, *10*, 1546–1551.
- (42) Zhang, K.; Zhang, Y.; Zhang, T.; Dong, W.; Wei, T.; Sun, Y.; Chen, X.; Shen, G.; Dai, N. Vertically coupled ZnO nanorods on MoS<sub>2</sub> monolayers with enhanced Raman and photoluminescence emission. *Nano Res.* **2015**, *8*, 743–750.
- (43) Nazir, G.; Khan, M. F.; Akhtar, I.; Akbar, K.; Gautam, P.; Noh, H.; Seo, Y.; Chun, S.-H.; Eom, J. Enhanced photoresponse of ZnO quantum dot-decorated MoS<sub>2</sub> thin films. *RSC Adv.* **2017**, *7*, 16890–16900.
- (44) Hsiao, Y.-J.; Fang, T.-H.; Ji, L.-W.; Yang, B.-Y. Red-Shift Effect and Sensitive Responsivity of MoS<sub>2</sub>/ZnO Flexible Photodetectors. *Nanoscale Res. Lett.* **2015**, *10*, 443.
- (45) Jeong, H.; Oh, H. M.; Gokarna, A.; Kim, H.; Yun, S. J.; Han, G. H.; Jeong, M. S.; Lee, Y. H.; Lerondel, G. Integrated Freestanding Two-Dimensional Transition Metal Dichalcogenides. *Adv. Mater.* **2017**, *29*, 1700308.
- (46) Zhao, W.; Ribeiro, R. M.; Toh, M.; Carvalho, A.; Kloc, C.; Castro Neto, A. H.; Eda, G. Origin of Indirect Optical Transitions in Few-Layer MoS<sub>2</sub>, WS<sub>2</sub>, and WSe<sub>2</sub>. *Nano Lett.* **2013**, *13*, 5627–5634.
- (47) Buscema, M.; Steele, G. A.; van der Zant, H. S. J.; Castellanos-Gomez, A. The Effect of the Substrate on the Raman and Photoluminescence Emission of Single-Layer MoS<sub>2</sub>. *Nano Res.* **2014**, *7*, 561–571.
- (48) Drüppel, M.; Deilmann, T.; Krüger, P.; Rohlfing, M. Diversity of Trion States and Substrate Effects in the Optical Properties of an MoS<sub>2</sub> Monolayer. *Nat. Commun.* **2017**, *8*, 2117.
- (49) Li, H.; Zhang, Q.; Yap, C. C. R.; Tay, B. K.; Edwin, T. H. T.; Olivier, A.; Baillargeat, D. From Bulk to Monolayer MoS<sub>2</sub>: Evolution of Raman Scattering. *Adv. Funct. Mater.* **2012**, *22*, 1385–1390.
- (50) Golasa, K.; Grzeszczyk, M.; Bożek, R.; Leszczyński, P.; Wysmołek, A.; Potemski, M.; Babiński, A. Resonant Raman Scattering in MoS<sub>2</sub>: From Bulk to Monolayer. *Solid State Commun.* **2014**, *197*, 53–56.
- (51) Li, Z.; Xiao, Y.; Gong, Y.; Wang, Z.; Kang, Y.; Zu, S.; Ajayan, P. M.; Nordlander, P.; Fang, Z. Active Light Control of the MoS<sub>2</sub> Monolayer Exciton Binding Energy. *ACS Nano* **2015**, *9*, 10158–10164.
- (52) Djurišić, A. B.; Leung, Y. H. Optical Properties of ZnO Nanostructures. *Small* **2006**, *2*, 944–961.
- (53) Dixit, T.; Bilgaiyan, A.; Palani, I. A.; Nakamura, D.; Okada, T.; Singh, V. Influence of Potassium Permanganate on the Anisotropic Growth and Enhanced UV Emission of ZnO Nanostructures Using Hydrothermal Process for Optoelectronic Applications. *J. Sol-Gel Sci. Technol.* **2015**, *75*, 693–702.
- (54) Maier, S. A.; Kik, P. G.; Atwater, H. A.; Meltzer, S.; Harel, E.; Koel, B. E.; Requicha, A. A. G. Local Detection of Electromagnetic Energy Transport below the Diffraction Limit in Metal Nanoparticle Plasmon Waveguides. *Nat. Mater.* **2003**, *2*, 229–232.
- (55) Brown, A. M.; Sundararaman, R.; Narang, P.; Goddard, W. A.; Atwater, H. A. Nonradiative Plasmon Decay and Hot Carrier Dynamics: Effects of Phonons, Surfaces, and Geometry. *ACS Nano* **2016**, *10*, 957–966.
- (56) Museum, B.; Dame, N.; Atwater, H. A Small World Full of Opportunities. *Nat. Mater.* **2010**, *9*, 181.
- (57) Andreasen, J.; Asatryan, A. A.; Botten, L. C.; Byrne, M. A.; Cao, H.; Ge, L.; Labonté, L.; Sebbah, P.; Stone, A. D.; Türeci, H. E.; et al. Modes of Random Lasers. *Adv. Opt. Photon.* **2010**, *3*, 88–127.
- (58) Van Der Molen, K. L.; Tjerkstra, R. W.; Mosk, A. P.; Lagendijk, A. Spatial Extent of Random Laser Modes. *Phys. Rev. Lett.* **2007**, *98*, 143901.
- (59) Haglund, R. F.; Lawrie, B. J.; Mu, R. Coupling of Photoluminescent Centers in ZnO to Localized and Propagating Surface Plasmons. *Thin Solid Films* **2010**, *518*, 4637–4643.